Aus der Abteilung Kardiologie
Zentrum für Innere Medizin der
Universitätsmedizin Rostock
(Direktor: Univ.- Prof. Dr. med. Hüseyin Ince)

Multimodale Bildgebung der myokardialen Heilung nach einem Herzinfarkt im Mausmodell im Kontext kardialer Stammzelltherapien

Habilitationsschrift
(kumulativ)
Zur Erlangung des akademischen Grades
Doctor medicinae habilitatus (Dr. med. habil.)
der Universitätsmedizin Rostock

Vorgelegt von:
Dr. med. Cajetan Immanuel Lang
geb. am: 27.9.1984 in Filderstadt
Wohnhaft in: Rostock

https://doi.org/10.18453/rosdok_id00004054

Gutachter:

Prof. Dr. Hüseyin Ince, Universitätsmedizin Rostock, Zentrum für Innere Medizin, Abteilung Kardiologie

Prof. Dr. med. Christoph Rischpler, Universitätsklinikum Essen, Klinik für Nuklearmedizin

Prof. Dr. med. Stephan Baldus, Uniklinik Köln, Klinik III für Innere Medizin - Allgemeine und interventionelle Kardiologie, Elektrophysiologie, Angiologie, Pneumologie und internistische Intensivmedizin

Jahr der Einreichung: 2021

Jahr der Verteidigung: 2022

Inhaltsverzeichnis

1. Einleitung und Zielsetzung

Die chronische ischämische Herzkrankheit als Folge eines chronischen Koronarsyndroms ist weltweit die häufigste Todesursache [1] und stellt zudem eine enorme ökonomische Belastung der Gesundheitssysteme dar [2]. Um den Untergang funktionellen Myokards im Falle eines Herzinfarktes zu minimieren, muss die Blutversorgung durch revaskularisierende Verfahren wie perkutane Koronarinterventionen oder Bypass-Operationen wiederhergestellt werden. Trotz dieser Maßnahmen kommt es in vielen Fällen zu einer relevanten Myokardnekrose mit einer resultierenden ischämischen Kardiomyopathie. Oft entwickelt sich daraus eine klinisch manifeste Herzinsuffizienz, welche - auch unter Einsatz moderner interventioneller und pharmakologischer Therapien - ähnlich maligne wie viele onkologische Erkrankungen verläuft [3].

Anfang der 2000er Jahre wurde vor diesem Hintergrund das Konzept des funktionellen Herzgewebsersatzes durch intramyokardial transplantierte Knochenmarkstammzellen innerhalb kürzester Zeit vom Mausmodell in die Klinik [4, 5] translatiert. Entgegen anfänglicher Hoffnungen wurde die Hypothese, dass hämatopoetische Stammzellen nach Transplantation milieuabhängig zu Kardiomyozyten differenzieren, jedoch schon bald entkräftet [6-8]. Trotzdem konnten in Tiermodellen reproduzierbar positive Effekte durch die Injektion adulter Stammzellen in das geschädigte Myokard erreicht werden, sodass die These sogenannter „parakriner Effekte“ als Wirkmechanismus formuliert wurde [9]. Unter dem Begriff der parakrinen Effekte wurden alle positiven Effekte auf das Zielgewebe durch von transplantierten Zellen sezernierte Wachstumsfaktoren und Chemokine zusammengefasst. Enttäuschenderweise zeigten klinische Studien bis auf eine sichere Durchführbarkeit keine überzeugenden Daten hinsichtlich ihrer Wirksamkeit [10]. In einem Perspektiven-Papier kommt die US-amerikanische „Food and Drug Administration“ (FDA) in 2016 folglich zum Schluss, dass keine belastbare wissenschaftliche Evidenz für den klinischen Einsatz von Knochenmarkstammzellen und mesenchymaler Stammzellen für kardiale Stammzelltherapien vorliegt [11].

Während sich klinische Studien hauptsächlich auf die Anwendung adulter Stammzellen konzentrierten, wurde in Mäusen ein wesentliches breiteres Spektrum therapeutischer Zellpopulationen untersucht. Von besonderem Interesse waren dabei aus pluripotenten Stammzellen gewonnene kardiovaskuläre Zellen und kardiale Stammzellen [12]. Allerdings wurde auch hier, insbesondere hinsichtlich sogenannter kardialer Stammzellen (CSC), das Konzept des funktionellen Ersatzes untergegangenen Myokards heftig kritisiert [13]. Kürzlich stellte die Arbeitsgruppe um Jeffrey Molkentin in einer bahnbrechenden Arbeit die Hypothese auf, dass der positive Effekt intramyokardial transplantierter Stammzellen durch eine unspezifische akute Immunantwort zustande kommt, die ebenso gut durch die Injektion des Pyrogens „Zymosan“ erreicht werden kann [14], sodass sich das ganze Forschungsfeld aktuell auf einer Kurskorrektur befindet [15]. Dennoch führt die Stammzelltherapie im Tiermodell nach einem chirurgisch induzierten Myokardinfarkt reproduzierbar zu einer Verbesserung der kardialen Funktion, wenn auch höchstwahrscheinlich nicht durch die vor mehr als 15 Jahren vorgeschlagenen Mechanismen [16].

Um die Wirkung besser verstehen und potentielle Therapien entwickeln zu können, muss aus meiner Sicht der Fokus auf eine therapeutische Modulation des Heilungsprozesses nach einem Herzinfarkt gelegt werden. Durch das bessere Verständnis der komplexen Vorgänge im Heilungsprozess nach einem Herzinfarkt im letzten Jahrzehnt [17, 18] kommen wir einer gezielteren und spezifischeren Modulation der involvierten „Heilungskomponenten“ mit dem Ziel einer „besseren“ Infarktheilung immer näher. Eine besondere Rolle spielt dabei das Mausmodell, in welchem der hochdynamische und komplexe Prozess der myokardialen Heilung in den ersten Wochen nach einem akuten Herzinfarkt sehr detailliert untersucht worden ist:

Im hypoxisch geschädigten murinen Myokard spielen sich die biologischen Prozesse in drei charakteristischen Phasen ab. In den ersten 72 Stunden findet eine starke Inflammation statt, die von infiltrierenden Leukozyten, welche abgestorbene Zellen und Interzellulärmatrix abräumen, dominiert ist. In der sich anschließenden proliferativen Phase (bis ca. 7 Tage nach der akuten Ischämie) wird infarziertes Myokard durch Granulationsgewebe ersetzt. Fibroblasten differenzieren sich zu Myofibroblasten und sezernieren eine extrazelluläre Matrix, welche von einem einsprossenden Gefäßnetzwerk durchzogen wird. In der Reifungsphase kommt es zur Apoptose von Fibroblasten, das angiogenetisch eingesprosste Gefäßnetzwerk bildet sich zurück und es entsteht eine kollagenreiche Narbe [19]. Diese Phasen werden maßgeblich durch verschiedene Entitäten von Makrophagen- und Monozyten-Populationen koordiniert [18, 20].

Einer der Gründe für die fehlende Translatierbarkeit dieser experimentellen Therapien ist, dass deren Wirkmechanismen im Menschen bisher kaum untersucht werden können. Biologische

Prozesse, wie die zelluläre Inflammation oder die Gefäßeinsprossung nach einem Herzinfarkt, werden in konventionellen präklinischen Versuchsaufbauten meist durchflusszytometrisch oder immunhistochemisch post mortem untersucht und sind damit nicht für eine direkte Anwendung in lebenden Patienten geeignet. Allerdings birgt die nuklearmedizinische molekulare Bildgebung das Potential, diese Lücke zu schließen.

Insbesondere die Positronen-Emissions-Tomographie (PET) ermöglicht eine Korrelation bildgeberischer Datensätze mit den Ergebnissen histologischer, zell- und molekularbiologischer Experimente. Somit lassen sich biologische Mechanismen im Mausmodell etablieren, die dann aber über die gemeinsame Methode der PET das Potential für eine potentielle Translation in die Klinik haben.

Konkrete Ziele

Das übergeordnete Ziel der im Folgenden zusammengefassten Arbeiten war, Methoden im Mausmodell zu entwickeln und zu evaluieren, mit denen das Verhalten intramyokardial transplantierter Zellen, deren Wirkmechanismus und deren Effekt auf das linksventrikuläre Remodeling *in-vivo* gemessen werden kann. Das Schicksal der transplantierten Zellen und die Wirkmechanismen – zelluläre Inflammation und Angiogenese – wurden dabei vor allem mittels PET untersucht. Für die Etablierung der Bildgebung des LV Remodeling spielte die kardiale Magnetresonanztomographie die tragende Rolle.

2. Methoden

Auf methodische Details wird in den jeweiligen Manuskripten ausführlich eingegangen.

3. Ergebnisse im Kontext der einzelnen Studien

3.1. ^{18}F-FDG-PET basierte *in-vivo* Bildgebung des Schicksals von intramyokardial transplantierten Zellen im Mausmodell: Vergleich von Stammzellen und Fibroblasten

In den meisten experimentellen Studien zu kardialen Stammzelltherapien wird das therapeutische Zellpräparat nach einem Herzinfarkt in die Grenzzone zwischen Infarkt und gesundem Myokard injiziert. Nur ein kleiner Teil der transplantierten Zellen überlebt langfristig im Zielgewebe, sodass verschiedene Strategien, das „Engraftment“ der Zellen zu verbessern, untersucht worden sind [21-23]. Allerdings sind die pathophysiologischen Mechanismen, welche zu diesem Zellverlust führen, noch unzureichend verstanden.

Trotzdem wurden bereits verschiedene Strategien, das Langzeit-„Engraftment“ zu verbessern, untersucht [23]. So führte die Ko-Transplantation von Fibroblasten zu einer signifikanten Verbesserung des Langzeitüberlebens von „ESC-derived cardiomyocytes“ [24]. Um solche Therapieansätze gezielt weiter zu optimieren, muss das Zeitfenster, in welchem Fibroblasten vermeintlich unterstützende Effekte ausüben, identifiziert werden.

Wir konnten zeigen, dass schon nach 25 Minuten nur noch etwa 5 % der applizierten Zellen im Myokard nachweisbar sind [25]. Vor diesem Hintergrund wollten wir untersuchen, ob Fibroblasten (FB) im Vergleich zu embryonalen Stammzellen (ESC) ein besseres Retentionsverhalten in den ersten zwei Stunden nach der Injektion ins infarzierte Myokard aufweisen.

Dazu wurden nach Induktion eines Herzinfarktes in Mäusen mit ^{18}F-FDG markierte ESC bzw. FB in die Grenzzone des Herzinfarktes injiziert. Direkt im Anschluss erfolgte eine dynamische Positronen-Emissions-Tomographie (PET) um die Biodistribution und Retention der jeweiligen Zellen zu messen. Für eine größtmögliche Genauigkeit wurden die PET-Daten um den zellulären FDG-Efflux korrigiert.

Unabhängig vom Zelltyp trat eine massiver Zellverlust in den ersten 25 Minuten auf, wobei FB in den ersten 60 Minuten noch eine signifikant bessere Retentionsrate als ESC zeigten (7,5±1,7 vs. 5,2± 0,7 % ID bei 25 min und 7,0±1,5 vs. 4,8±0,8 % ID bei 60 min). Nach 120 Minuten konnten unabhängig vom Zelltyp noch etwa 5 % am Injektionsort nachgewiesen werden (120 min, ESC vs. FB; p=0,64). Ein Großteil der verlorenen Zellen fand sich in der Lunge wieder (~30 %).

In dieser Studie gelang es uns somit zum ersten Mal, mittels PET-Bildgebung im Mausmodell die Retention und Biodistribution verschiedener Zelltypen *in-vivo* quantitativ zu bestimmen.

Dabei beobachteten wir sowohl für FB als auch ESC einen massiven initialen Zellverlust von ~95 %. Entsprechend scheinen FB im Vergleich zu ESC keine privilegierte akute Retentionskinetik aufzuweisen. Folglich gehen wir davon aus, dass FB ihren mutmaßlich positiven Effekt erst später ausüben und unabhängig vom Zelltyp Strategien benötigt werden, die akute Retention zu erhöhen.

3.2. ^{18}F-FDG-PET-basierte Bildgebung der myokardialen Inflammation nach einem akuten Herzinfarkt im Mausmodell

Die zelluläre Inflammation ist ein integraler Bestandteil des Heilungsprozesses nach einem akuten Myokardinfarkt (MI) [17]. Als biologischer Schlüsselmechanismus stellt sie ein attraktives Ziel für neue Therapien und prognostische Verfahren dar [26]. Auf zellulärer Ebene wird der Heilungsprozess ab dem 3. Tage nach MI vor allem durch Monozyten und Makrophagen bestimmt. Als metabolische hochaktive Zellen sind sie durch eine hohe Aufnahme von Glukose und entsprechend dessen Analogon ^{18}F-FDG (FDG) gekennzeichnet [26]. Um mittels FDG Positronen-Emissions-Tomographie (PET) die gemessene Radioaktivität den Monozyten und Makrophagen zuordnen zu können, ist eine Unterdrückung des Glukosestoffwechsels im vitalen Myokard zwingend erforderlich. Im Mausmodell, dem wichtigsten Modellorganismus in der Grundlagenforschung, kann dies durch eine Narkose mit Ketamin/Xylazin (KX) erreicht werden [26-28]. Allerdings gibt es bisher keine einheitliche Strategie zur reproduzierbaren Bildanalyse. Entsprechend uneinheitlich fällt die Interpretation der jeweiligen Daten aus. Sollen Therapien evaluiert werden, welche die myokardiale Inflammation modulieren, ist das jedoch eine unabdingbare Voraussetzung. Ziel der Studie war deshalb, eine einfache Strategie zur systematischen Bildanalyse der FDG-PET-Daten im Mausmodell zu etablieren.

Dazu wurde in Mäusen durch Okklusion des Ramus interventrikularis anterior (RIVA) ein akuter Myokardinfarkt induziert. Nach 5 Tagen wurde ein statischer FDG-PET/CT-Scan unter Ketamin/Xylazin-Anästhesie durchgeführt. Für die Bildrekonstruktion wurden aufeinanderfolgend die Algorithmen „3D ordered subset expectation maximization (3D-OSEM)“ und „3D ordinary poisson maximum a priori (MAP)“ verwendet. Die Auswertung der Daten erfolgte mit der Software *Inveon Research Workplace*.

Die höchste fokale Traceranreicherung fand sich typischerweise in der Randzone des Infarkts. Da sich diese Randzone schwer reproduzierbar in einem „Volume of Interest (VOI)“ erfassen lässt, basiert unser Protokoll auf der Positionierung von VOIs um jeweils den gesamten linken Ventrikel, die inferobasale und die anterolaterale Wand. Mit diesem Protokoll stellen wir eine Strategie zur systematischen Analyse der FDG-PET-Daten in der Inflammationsbildgebung nach einem Herzinfarkt zur Verfügung. Damit konnten wir die Grundlage schaffen, um die myokardiale Inflammation als prognostischen Marker in experimentellen Therapieansätzen zu vergleichen.

3.3. Detektion der myokardialen Inflammation nach einem Herzinfarkt im Mausmodell mittels ^{18}F-FDG-PET als Prädiktor der kardialen Funktion nach Transplantation von „cardiac induced cells“

In diesem Projekt wurde untersucht, welchen Einfluss die syngene Transplantation von „cardiac induced cells“ (CiC) auf die zelluläre Inflammation im Heilungsprozess und das resultierende Remodeling des linken Ventrikels nach einem akuten Herzinfarkt hat.

Nach der Induktion eines akuten Herzinfarktes (MI) im Mausmodell wurde entweder Matrigel (MI-Gruppe) oder Matrigel + 10^6 CiC (MIC-Gruppe) in die Randzone des Infarktes injiziert. 5 nach dem Herzinfarkt wurde eine FGD-PET durchgeführt. Dabei wurden die Tiere mit Ketamin und Xylazin (KX) narkotisiert, um den myokardialen Glukosestoffwechsel zu unterdrücken und somit die zelluläre Inflammation erfassen zu können [26, 29]. Eine detaillierte Analyse der am Heilungsprozess beteiligten Monozyten- Makrophagenpopulationen wurde in separaten Gruppen durchflusszytometrisch untersucht. Der Einfluss der Zelltherapie auf das linksventrikuläre Remodeling wurde mittels kardialer Magnetresonanz (CMR)-Bildgebung 3 Wochen nach der Herzinfarktinduktion erfasst.

Mit der FDG-PET ließ sich in der MI-Gruppe eine hohe Akkumulation des Tracers in der „Borderzone“ des infarzierten Myokards nachweisen, während das Infarktareal und das „remote“ Myokard eine gleichermaßen niedrige Traceraufnahme aufwiesen. Das FDG-Aufnahmemuster veränderte sich durch die CiC-Transplantation deutlich. Sie führte im Vergleich zur MI-Gruppe zu einer signifikant erhöhten FDG-Akkumulation sowohl im gesamten Herzen als auch im „remote“ Myokard. Passend zu dieser Beobachtung konnten wir im „remote“ Myokard durchflusszytometrisch mehr CD11b$^+$-Zellen nachweisen. Auf funktioneller Ebene ließ sich durch die CiC-Transplantation eine signifikante Verbesserung der linksventrikulären Ejektionsfraktion erreichen.

Aus diesen Beobachtungen folgern wir, dass der therapeutische Effekt der CiC-Transplantation durch eine Modulation der zellulären Entzündungsreaktion im Heilungsprozess nach dem AMI zustande kommt. Somit konnten wir zeigen, dass die FDG-basierte PET-Bildgebung zur Messung der zellulären Inflammation nach AMI einen Prädiktor für die Wirksamkeit kardialer Stammzelltherapien darstellt.

3.4. ^{68}Ga-NODAGA-RGD Positronen-Emissions-Tomographie (PET) zur Beurteilung der Angiogenese nach Myokardinfarkt als Prädiktor für das linksventrikuläre Remodeling einer kardialen Stammzelltherapie im Mausmodell

Die Angiogenese spielt eine zentrale Rolle im Heilungsprozess nach einem akuten Myokardinfarkt [30, 31]. Entsprechend ist sie sowohl als therapeutischer Zielmechanismus, als auch aus diagnostischer Sicht höchst interessant und wird entsprechend intensiv beforscht [32, 33]. Eine wichtige Rolle spielt dabei das $\alpha_v\beta_3$-Integrin, welches als Vitronektin-Rezeptor auf sprossenden Endothelzellen exprimiert wird [34]. Die Bindung des Integrins an Proteine der extrazellulären Matrix erfolgt dabei über die Aminosäuresequenz RGD [35]. Entsprechend wurden verschiedene RGD-basierte Tracer für die Bildgebung der $\alpha_v\beta_3$-Integrin-Expression mittels Singlephotonen-Emissionscomputertomographie (SPECT) und PET in tierexperimentellen und klinischen Studien zur Darstellung der Angiogenese im Heilungsprozess nach einem akuten Herzinfarkt untersucht [33]. Allerdings fehlt bisher belastbare Evidenz, ob das Ausmaß der Tracer-Anreicherung im heilenden Myokard mit dem funktionellen Ergebnis korreliert.

Ziel dieser Arbeit war es daher, erstens den Tracer ^{68}Ga-NODAGA-RGD für die Bildgebung der $\alpha_v\beta_3$-Integrin-Expression im Heilungsprozess nach einem Herzinfarkt im Mausmodell zu etablieren und zweitens den Tracer als Prädiktor für das Ausmaß kardialen Remodeling im Rahmen einer kardialen Stammzelltherapie zu evaluieren.

Nach der Induktion eines akuten Herzinfarktes (MI) im Mausmodell wurde entweder Matrigel oder Matrigel + 10^6 „Cardiac induced Cells“ (CiC) in die Randzone des Infarktes injiziert. Eine SHAM-Gruppe, die als Negativkontrolle diente, wurde lediglich thorakotomiert und das Myokard im Bereich der LAD-Ligationstelle mit Nadel und Faden durchstochen.

In separaten Gruppen wurde nach 7 Tagen eine ^{68}Ga-NODAGA-RGD-PET und nach 3 Wochen eine kardiale MRT (CMR) durchgeführt. Die Spezifität der Bindung von ^{68}Ga-NODAGA-RGD an das $\alpha_v\beta_3$-Integrin wurde durch die Applikation des kompetitiven Inhibitors Cilengitide gezeigt.

Durch die Injektion von Cilengitide 10 Minuten vor der Applikation des Tracers ließ sich die ^{68}Ga-NODAGA-RGD-Anreicherung auf SHAM-Niveau supprimieren.

Die Herzinfarktgruppe (MI) wies 7 Tage nach MI eine intensive Akkumulation des Tracers in der Infarktregion auf. Nach 3 Wochen zeigte sich in der CMR ein ausgeprägtes Remodeling des linken Ventrikels, welches in einer hochgradig reduzierten linksventrikulären Ejektionsfraktion (LVEF) resultierte. Die CiC-Transplantation führte zu einer signifikanten Verbesserung der LVEF. Entgegen unserer Erwartung im Kontext der existierenden wissenschaftlichen Literatur [36-39] führte die CiC-Transplantation zu einer signifikant geringeren Tracer-Akkumulation.

Uns ist es somit gelungen, den PET-Tracer ^{68}Ga-NODAGA-RGD erfolgreich für die Visualisierung und Quantifizierung der $\alpha_v\beta_3$-Integrin-Expression im Heilungsprozess nach einem Herzinfarkt im Mausmodell zu etablieren. Ob das Ausmaß der $\alpha_v\beta_3$-Integrin-Expression ein geeigneter Prädiktor für das Ausmaß des linksventrikulären Remodeling nach einem Herzinfarkt ist, muss in zukünftigen Studien noch weiter untersucht werden, da nun inkonklusive Ergebnisse zur Korrelation der beiden Parameter vorliegen.

3.5. Native kardiale Magnetresonanztomographie zur Darstellung des ventrikulären Remodeling nach Herzinfarkt im Mausmodell – Evaluation verschiedener Parameter im Vergleich der beiden Infarktmodelle permanente versus transiente Okklusion der LAD

Der Heilungsprozess nach einem akuten Herzinfarkt, als Zielmechanismus neuer therapeutischer Ansätze, wird derzeit intensiv beforscht. Für die Entschlüsselung zugrunde liegender biologischer Mechanismen auf molekularer und zellulärer Ebene ist die Maus der Modellorganismus der Wahl [40]. Potentielle Therapien sollten über eine positive Modulation der myokardialen Heilung zu einem geringeren myokardialen Schaden und entsprechend weniger ausgeprägtem linksventrikulären Remodeling führen. Während der myokardiale Schaden oft histologisch erfasst wird [41], stellt die „linksventrikuläre Ejektionsfraktion" (LVEF) den am häufigsten verwendeten Surrogatparameter für die kardiale Funktion dar [42]. Oft sind auch Studien, welche die kardiale Funktion mittels CMR erfassen, auf diesen Parameter begrenzt.

Da selbst native Aufnahmen viel mehr Potential haben, war das Ziel unserer Studie, das Post-Infarkt-Remodeling mittels nativer CMR so umfassend wie möglich zu beschreiben. Anhand verschiedener Parameter haben wir die beiden prominentesten Infarktmodelle, die permanente Ligatur (PL) der linken anterioren absteigenden Arterie (LAD) versus Ischämie-Reperfusion (I/R), untersucht.

Dazu wurden Mäuse entweder einem permanenten oder einem transienten (45 min) Verschluss der LAD unterzogen. Nach 3 Wochen erfolgte eine native CMR mit einem 7-Tesla-Kleintier-MRT. Die Datenanalyse wurde mit der frei erhältlichen Software Segment durchgeführt.

Eine PL der LAD führte zu einer massiven Dilatation des linken Ventrikels, die mit einer Hypertrophie des nicht-infarzierten Myokards und einer Abnahme der kontraktilen Funktion einherging. Diese Effekte waren in der I/R-Gruppe weniger stark ausgeprägt.

Messungen in einzelnen repräsentativen Ebenen, analog zu parasternalen Anlotungen in der Echokardiographie, eigneten sich nicht, um die morphologischen Unterschiede des linken Ventrikels zwischen den beiden Infarktmodellen zu erfassen.

Allerdings erwiesen sich Bulls-Eye-Plots als ideales Werkzeug für eine Beurteilung des linksventrikulären Myokards auf qualitativer Ebene. Durch die Verwendung einer strukturierten sektorbasierten Mehrschicht-Analyse aller 5 axialen Schnitte ist es uns gelungen, Unterschiede bezüglich morphologischer und funktioneller Eigenschaften des linksventrikulären Myokards auch auf einer quantitativen Ebene zu beschreiben.

Die Kombination der Polar-Map-Analyse mit den volumetrischen Messungen einer nativen CINE CMR stellt ein vielseitiges und leicht verfügbares Werkzeug zur seriellen Beurteilung des LV während des Remodeling-Prozesses dar. Damit soll auch weniger CMR-versierten Forschenden eine Möglichkeit gegeben sein, das LV Remodeling so umfassend wie möglich zu beschreiben.

4. Diskussion

Ziel der zusammengefassten Arbeiten war, Methoden zu entwickeln, um den Heilungsprozess nach einem Herzinfarkt im Mausmodell und die resultierenden Veränderungen des linken Ventrikels *in-vivo* darzustellen. Die Evaluierung dieser Methoden erfolgte dabei im Kontext kardialer Zelltherapien.

Die wesentliche Aussage der ersten Arbeit ist, dass unabhängig vom Zelltyp die meisten intramyokardial injizierten Zellen im Infarktmodell der Maus schon nach 25 Minuten nicht mehr am Applikationsort, sondern in der Lunge zu finden sind. Die verwendete Methode, eine Markierung der transplantierten Zelle mit ^{18}F-FDG, welche eine Darstellung und

Quantifizierung der transplantierten Zellen mittels PET *in-vivo* ermöglicht, hatten wir kürzlich für das Mausmodell etabliert [43]. Mit einer ähnlichen Methode hatten Wissenschaftler an der John Hopkins Universität in Baltimore auch in Ratten nach Herzinfarkt einen hohen Zellverlust innerhalb der ersten Stunde nach der Injektion festgestellt [21-23]. Dieser massive initiale Zellverlust scheint dabei unabhängig von der Spezies zu sein – ähnliche Daten liegen auch für das Schweinemodell vor [44] - und scheint vor allem durch eine mechanische Extrusion der Zellen durch die Kontraktion des Herzens zustande zu kommen. Entsprechend höher sind die Retentionsraten in größeren Tiermodellen mit entsprechend niedrigeren Herzfrequenzen [21, 44]. Interessanterweise wurde das Phänomen, dass die meisten intramyokardial transplantierten Zellen nach kurzer Zeit in der Lungenstrombahn nachweisbar sind, auch von anderen Forschungsgruppen beobachtet [21]. Dieses Entrapment der transplantierten Zellen in den Lungen wurde in klinischen Studien nicht beschrieben und könnte ein Phänomen sein, das anatomisch bedingt ist und durch die Größe der applizierten Zellen nur im Kleintiermodell auftritt [45, 46]. Daher werten wir das Phänomen nicht als relevante Nebenwirkung, sondern als indirekten Indikator für das Ausmaß des frühen „Washouts“ der Zellen. Wenn also die Zahl der transplantierten Zellen erhöht werden soll, muss der frühe mechanisch bedingte Zellverlust gezielt reduziert werden. Die von uns entwickelte Methode wäre - durch die Integration des zell- und organspezifischen FDG-Effluxes - empfindlich genug, um im Mausmodell diesbezüglich neue Strategien zu entwickeln.

In den nächsten Studien lag der Fokus dann vor allem auf der Entwicklung von Strategien, die biologischen Mechanismen, die der Wirksamkeit kardialer Zelltherapien zugrunde liegen, *in-vivo* zu visualisieren und zu quantifizieren. Um eine Translation solcher neuartigen Therapien in die Klinik zu schaffen, muss sich der postulierte Wirkmechanismus auch in Patienten darstellen lassen.

Die Wahl des therapeutischen Zellpräparates – die wir „Cardiac induced Cells“ (CiC) genannt haben - beruht im Wesentlichen auf der Beobachtung, dass in einer von uns durchgeführten Meta-Analyse kardiovaskulär differenzierte Zellen (ausgenommen pluripotente Stammzellen, die jedoch ein hohes tumorigenes Potential haben) den tendenziell besten Effekt auf die LVEF im Mausmodell hatten [47]. Zudem zeigten unpublizierte Daten aus unserem Labor, dass eine Vereinzelung der Zellen im Stadium der „embryoid bodies“ (EB), wie sie für eine antikörperbasierte Aufreinigung über spezifische Oberflächenmarker (wie z.B. Flk-1 [48]) notwendig ist, die Differenzierungsfähigkeit *in-vitro* beeinträchtigt. Entsprechend haben wir ein kardiales Differenzierungsprotokoll [49, 50] verwendet und die Zellen als EBs an Tag 6 der Differenzierung transplantiert.

Für die Bildgebung der zellulären Inflammation hat sich im klinischen Alltag die ^{18}F-FDG-PET etabliert. Grundlage ist der hohe Glukosestoffwechel aktivierter Leukozyten, die sich vor allem in Gewebe mit niedrigem Glukoseumsatz gut abgrenzen lassen [51]. Entsprechend muss für eine ^{18}F-FDG-PET der inflammatorischen Zellen im metabolisch aktiven Herzen, der myokardiale Glukosestoffwechsel supprimiert werden. In Patienten kann dies über eine kohlenhydratarme Diät am Tag vor der Untersuchung gefolgt von einer Fastenperiode von 12 Stunden und der intravenösen Applikation von Heparin direkt vor der Untersuchung erreicht werden [52].

Im Mausmodell hingegen konnte gezeigt werden, dass allein durch die Verwendung einer Narkose mit Ketamin und Xylazin (KX) statt Isofluoran der myokardiale FDG-Uptake um etwa 90% supprimiert werden kann [26-29]. Allerdings lag bis vor kurzem kein standardisiertes Auswertungsprotokoll der FDG-basierten Bildgebung myokardialer Inflammation nach Herzinfarkt vor. Zudem wurde die Methode noch nicht im Kontext einer Therapie, die den Inflammationsprozess moduliert, evaluiert.

Deshalb haben wir im ersten Schritt ein Protokoll zur standardisierten Auswertung der Inflammations-PET mit FDG und KX-Narkose entwickelt [29] und dieses in einem zweiten Schritt angewendet [53], um den Effekt einer kardialen Zelltherapie mit „Cardiac induced Cells“ (CiC) auf die zelluläre Inflammation zu messen. Durch die innovative Kombination aus einer qualitativen Beurteilung der Bilder mit einer reproduzierbaren Positionierung standardisierter „Volumes of Interest“ (VOI) liefert unsere Publikation hier einen deutlichen Mehrwert.

Ähnlich wie Lee und Kollegen [26] konnten wir zeigen, dass es an Tag 5 nach einem Herzinfarkt vor allem in der Grenzzone zwischen Herzinfarkt und vitalem Myokard („Borderzone“) zu einer fokalen Mehranreicherung kommt. Diese PET/CT-morphologische Beobachtung korreliert mit histologischen Untersuchungen, die eine hohe Zahl infiltrierender CD11b^{+} Zellen in der entsprechenden Region zeigten [26]. Lee und Kollegen konnten zeigen, dass der größte Anteil an FDG genau von dieser Zellpopulation gespeichert wird [26]. Durch die Narkose mit KX kam es sowohl im gesunden Myokard als auch dem Infarktareal zu einer deutlichen Suppression der FDG-Anreicherung auf vergleichbar niedrige Level; ähnliche Beobachtungen hatte auch die

Arbeitsgruppe um Frank Bengel gemacht [27, 28]. Die Zell-Transplantation führte - 5 Tage nach dem Herzinfarkt - interessanterweise nur zu einem signifikanten Anstieg der FDG-Anreicherung im gesamten Herzen und dem gesunden Myokard, während der FDG-Uptake im Infarktareal unverändert blieb. Passend zu dieser Beobachtung konnten wir auf durchflusszytometrischer Ebene eine prozentuale Erhöhung der CD11b$^+$ Zellen im gesunden Myokard nachweisen.

Um die in diesem Prozess involvierten Zellpopulationen genauer zu beschreiben, haben wir durchflusszytometrische Analysen der jeweiligen Infarktregion und des gesunden Myokards vorgenommen, in denen die myeloischen Zellen (CD45$^+$/**CD11b$^+$/**CD11c$^-$) weiter subdifferenziert wurden. Im gesunden Myokard führte die Zelltherapie 5 Tage nach dem Herzinfarkt zu einer prozentualen Erhöhung der CD11b$^+$ Zellen und der „monocyte-derived“ Makrophagen. Im Infarktareal führte die Zelltherapie zu einer signifikanten Reduktion der „yolk-sac derived“ Makrophagen. Während die Änderung des FDG-Verteilungsmusters mit dem funktionellen Effekt der Zell-Therapie korreliert, ist die Bedeutung des Einflusses der Therapie auf die Modulation der CD11b$^+$ Zell-Subpopulationen weniger klar.

Nahrendorf und Kollegen hatten um 2007 die Hypothese aufgestellt, dass der Heilungsprozess nach einem Herzinfarkt maßgeblich durch eine biphasische Infiltration zweier Monozytenpopulationen organisiert wird. Immunphänotypisch werden sie durch eine hohe bzw. eine niedrige Expression von „Ly-6C“ unterschieden. Ly-6C^{high} bzw. Ly-6C^{low} Monozyten werden chemotaktisch jeweils über die Zytokingradienten von CCL2 bzw. CX3CL1 über die entsprechenden Rezeptoren (CCR2 und CX3CR1) ins Myokard geleitet. Die Ly-6C^{high} Monozyten sind phagozytotisch und proteolytisch aktive Zellen, welche die inflammatorische Phase dominieren, während Ly-6C^{low} Monozyten in der proliferativen Phase über Stimulation von Fibroblasten, Angiogenese und Kollagenbildung eine zentrale Rolle spielen [20]. Dieses Konzept basiert auf der lange vorherrschenden Hypothese, dass Gewebsmakrophagen aus im Blut zirkulierenden Monozyten entstehen, welche wiederum aus hämatopoetischen Stammzellen im Knochenmark hervorgehen [54].

In den letzten 10 Jahren wurde klar, dass die Organisation des myokardialen Heilungsprozesses noch wesentlich komplexer ist. Besonders interessant waren diesbezüglich vergleichende Studien zwischen adulten und neonatalen Mäusen hinsichtlich der Heilung nach einem experimental induzierten myokardialen Schaden [55-57]. Das Herz neonataler Mäuse kann sich nach einem Herzinfarkt komplett regenerieren. Diese Fähigkeit geht schon 7 Tage nach der Geburt verloren. Eine wesentliche Rolle spielen dabei gewebsständige Makrophagen, die ihren

Ursprung nicht nur in zirkulierenden Monozyten, sondern vor allem in embryonalen Vorläuferzellen haben [18]. Über die jeweilige Expression der Oberflächenantigene MHC-II und CCR2 lassen sich die gewebsständigen Makrophagen in drei Subtypen einteilen: die numerisch größte Population stellen MHC-II^{low} / CCR2$^-$ und MHC-II^{hi} / CCR2$^-$ Makrophagen, welche embryonalen Vorläufern entstammen. Ein dritter CCR$^+$ Subtyp stammt von zirkulierenden Monozyten ab.

Während der Heilung nach myokardialer Schädigung in neonatalen Mäusen expandieren vor allem MHC-II^{low} / CCR2$^-$ Makrophagen, die ein Mileu schaffen, welches in einer kompletten Regeneration resultiert. Im Gegensatz dazu wird geschädigtes Myokard in adulten Tieren von Monozyten und MHC-II^{hi} / CCR2$^+$ Makrophagen infiltriert, was zu Narbenbildung und konsekutivem funktionellem Schaden führt [57]. Obwohl CCR2$^-$ gewebsständige Makrophagen in adulten Herzen vorhanden sind, gehen sie während einer myokardialen Schädigung unter und werden durch inflammatorische CCR2$^+$ "monocyte-derived“ Makrophagen ersetzt [57].

Daraus ergibt sich nun die Frage, ob eine Modulation der entsprechenden Makrophagen und Monozytenpopulationen die Heilung nach einem Myokardinfarkt ebenfalls in positiver Weise beeinflussen könnte.

In unserer Studie führte die Zelltherapie zu einer Reduktion von CCR2$^-$ Makrophagen an Tag 5 nach dem Infarkt, eine Verschiebung der dominierenden „monocyte-derived“ Makrophagen von M1 zu M2, wie von anderen Gruppen beobachtet wurde [58], konnten wir nicht beobachten. Vielmehr führte die Zelltherapie zu einer höheren Infiltration beider Makrophagenpopulationen. Trotzdem führte die Transplantation der CiC zu einer verbesserten kardialen Pumpfunktion. Für eine gezielte therapeutische Modulation auf Ebene der einzelnen Makrophagensubtypen muss folglich noch ein weitaus besseres Verständnis der biologischen Prozesse in der Heilung nach einem Herzinfarkt erarbeitet werden.

Monozyten und Makrophagen sind die zentralen Mediatoren im Heilungsprozess nach einem Herzinfarkt. Sie koordinieren während der inflammatorischen Phase die Beseitigung des nekrotischen Gewebes und in der darauffolgenden proliferativen Phase den Aufbau der Narbe. Die beteiligten Zellen sind metabolisch hoch aktiv und haben einen entsprechend hohen Energiebedarf. Auf histologischer Ebene stellt sich diese Phase als sogenanntes „Granulationsgewebe“ dar, in dessen Matrix ein dichtes Netzwerk aus Kapillaren aus der Umgebung einsprosst [19]. An den Spitzen dieser wachsenden Gefäße befinden sich sogenannte „tip cells“, welche über durch hohe Expression des $\alpha_v\beta_3$-Integrins über die Aminosäure-Sequenz RDG (Arginin, Glycin und Asparaginsäure) an Moleküle der extrazellulären Matrix binden [34] . Ruhende Endothelzellen exprimieren das $\alpha_v\beta_3$-Integrin nur minimal, wodurch es sich hervorragend als Ziel für molekulare Bildgebung und Therapien eignet [59].

Das Konzept der $\alpha_v\beta_3$-Integrin-basierten molekularen Bildgebung als Surrogatmarker für die Angiogenese im Heilungsprozess ischämisch geschädigten Myokards [36, 60, 61] oder Skelettmuskel [62, 63], wurde bereits in verschiedenen und unabhängigen Forschungsgruppen evaluiert. Als integraler Bestandteil des Heilungsprozesses nach einem Herzinfarkt stellt die Angiogenese einen interessanten Zielmechanismus dar, um den myokardialen Schaden nach einer Ischämie zu limitieren und das Ausmaß des post-ischämischen Remodeling zu minimieren [60]. Entsprechend naheliegend war die Idee, das Ausmaß der $\alpha_v\beta_3$-Integrin-Expression mit dem Ausmaß des linksventrikulären Remodeling nach einem Herzinfarkt zu korrelieren.

Die wesentlichen Beiträge unserer Forschung in diesem Kontext sind nun zum einen die erfolgreiche Etablierung des PET-Tracers „^{68}Ga-NODAGA-RGD“ zur Darstellung und Quantifizierung der $\alpha_v\beta_3$-Integrin-Expression im Herzinfarktmodell der Maus, und zum anderen die Beobachtung, dass unsere Zelltherapie zwar zu einer Verbesserung der LVEF führt, aber 7 Tage nach dem Herzinfarkt – wider Erwarten – mit einer signifikant niedrigeren $\alpha_v\beta_3$-Integrin-Expression einhergeht. Insgesamt liegt bisher nur wenig Evidenz zur Korrelation des Ausmaßes der $\alpha_v\beta_3$-Integrin-Expression mit dem Ausmaß des linksventrikulären Remodeling vor:

Sherif *et al.* beschrieben im Rattenmodell - 7 Tage nach einem Herzinfarkt - eine positive Korrelation für das Ausmaß des linksventrikulären Remodeling mit der Höhe der $\alpha_v\beta_3$-Integrin-Expression im Infarktareal [38]. In einer kleinen klinischen Studie korrelierte die Tracer-Akkumulation nicht mit der Infarktgröße, sondern mit der funktionellen Erholung, was darauf hindeuten könnte, dass die $\alpha_v\beta_3$-Integrin-Expression weniger ein Surrogat für die Infarktgröße ist, sondern vielmehr mit der Heilungsreaktion des Gewebes auf die Verletzung zusammenhängt [39]. Allerdings kamen verschiedene Tracer (^{8}F-Galacto-RGD und ^{18}F-Fluciclatid) in unterschiedlichen Spezies zum Einsatz, sodass zum Zusammenhang zwischen $\alpha_v\beta_3$-Integrin-Expression und Ausmaß des linksventrikulären (LV) Remodeling noch kein kongruentes Bild vorliegt.

Der Effekt von Therapien, welche auf eine Modulation der Heilung nach einem Herzinfarkt abzielen, wurde ebenfalls von einigen anderen Gruppen mittels molekularer *in-vivo* $\alpha_v\beta_3$-Integrin-Bildgebung untersucht:
In unserem Mausmodell führte die CiC-Therapie zu einer Verbesserung der LVEF und einer signifikant niedrigeren $\alpha_v\beta_3$-Integrin-Expression an Tag 7. Lindsey *et al.* beschrieben, ebenfalls im Mausmodell, eine Erhöhung der $\alpha_v\beta_3$-Integrin-Expression an Tag 7 nach MI. Allerdings untersuchten sie in ihrer Studie den Effekt der Deletion der Matrix-Metalloprotease MMP-9 auf die extrazelluläre Matrixbildung mit dem Ziel, das LV-Remodeling positiv zu modulieren. Die LVEF verbesserte sich durch die MMP-9-Deletion signifikant [37]. Eine andere Gruppe konnte im Rattenmodell durch die Transplantation von humanen Nabelvenen-Endothelzellen (HUVECs) das Ausmaß des LV-Remodeling reduzieren und damit einhergehend eine Erhöhung der $\alpha_v\beta_3$-Integrin-Expression an Tag 5 nach MI detektieren [36]. Auch diese Studien werfen mehr Fragen auf, als sie beantworten können. Eine Erklärung für diese vermeintlich widersprüchlichen Ergebnisse könnte sein, dass die RDG-basierten Tracer zwar eine sehr hohe Spezifität für das $\alpha_v\beta_3$-Integrin aufweisen, dieses jedoch weniger spezifisch für den Prozess der Angiogenese ist, da es auch von weiteren Zelltypen wie Myofibroblasten [64] und Makrophagen [65] exprimiert wird. Für eine sinnvolle Verwendung von RGD-basierten Tracern muss die spezifische Rolle der $\alpha_v\beta_3$-Integrin-Expression in der myokardialen Heilung besser verstanden werden. Dabei könnten die Geschwindigkeit und der qualitative Verlauf der Heilung eine relevante Rolle spielen [66-68], sodass die involvierten biologischen Vorgänge hinsichtlich der zeitlichen Auflösung viel detaillierter verstanden werden müssen. Erst dann wird es möglich sein, den optimalen Zeitpunkt für quantitative Messungen einzelner Komponenten in diesem Prozess zu definieren. Wir halten es für sehr wahrscheinlich, dass Therapien, die auf den Heilungsprozess nach akutem Myokardinfarkt abzielen, eine Verschiebung der Geschwindigkeit der myokardialen Heilung bewirken, die spezifisch für das jeweils eingesetzte Therapeutikum ist. Bevor eine therapeutische Modulation der Heilung nach einem Herzinfarkt mittels RDG-Bildgebung evaluiert werden kann, ist eine Vertiefung des Verständnisses der $\alpha_v\beta_3$-Integrin-Expression in der proliferativen Phase der myokardialen Heilung unabdingbar und muss in zukünftigen Studien weiter untersucht werden.

Das Ausmaß des linksventrikulären Remodeling wird maßgeblich von der Größe des myokardialen Schadens nach einem akuten Herzinfarkt bestimmt [69, 70]. Die globalen volumetrischen Parameter endsystolisches Volumen (ESV), enddiastolisches Volumen (EDV) und linksventrikuläre Ejektionsfraktion (LVEF) sind entsprechend etablierte Surrogatmarker, um den Effekt relativ unspezifischer Therapien, wie einer pharmakologischen RAAS-Inhibition, zu erfassen [71]. Therapien - wie z.B. die lokale Applikation von Stammzellen – modulieren am Zielort einen spezifischen biologischen Mechanismus. Um solche Effekte besser erfassen zu können, reicht eine bloße Volumetrie nicht aus. Interessanterweise wurden verschiedene elaborierte Methoden entwickelt, mit denen eine CMR-basierte regionale Erfassung der linksventrikulären Eigenschaften möglich ist [72]. Trotzdem beschränken sich anwendungsorientierte Studien im Mausmodell meistens auf CMR-basierte volumetrische Messungen. Die Ursache dafür liegt unserer Meinung nach am fehlenden Zugang vieler biologisch orientierter Forschungsgruppen zur CMR Radiologie und den hohen Kosten der dafür benötigten Software. Vor diesem Hintergrund war das Ziel unserer Arbeit die Entwicklung eines einfachen Protokolls, mit dem auf Basis einer nativen CINE CMR möglichst viele Informationen über regionale und funktionelle Eigenschaften der linksventrikulären Wand erfasst werden können.

Anhand der beiden Infarktmodelle - permanente Ligatur (PL) und transiente Ligatur der LAD (I/R) - wurden verschiedene Parameter 3 Wochen nach dem Herzinfarkt mittels nativer CINE CMR gemessen und evaluiert.

Beide Infarkte führten zu einer Dilatation des linken Ventrikels und einer konsekutiv erniedrigten LVEF. Wie zu erwarten, fiel das Ausmaß der LV-Dilatation in der PL-Gruppe signifikant extremer aus [73-75] . Interessanterweise war – passend zu einer kompensierten Herzinsuffizienz - das Schlagvolumen (SV) in den Infarktgruppen im Vergleich zu gesunden Tieren nicht wesentlich reduziert. Die LV-Dilatation führt also bei reduzierter LVEF - zumindest in einem gewissen Rahmen - zu einer Kompensation des Herzzeitvolumens (HZV) und wurde sowohl in Patienten [76] als auch in einer Mausstudie [73] beschrieben.

Die globalen volumetrischen Parameter ESV und EDV und die davon abgeleiteten Parameter LVEF und SV liefern allerdings keine Information über regionale Eigenschaften des linken Ventrikels, der im gesunden Myokard hypertrophiert und im Bereich der Narbe progressiv dilatiert. Während bei der PL eine transmurale Narbe entsteht, bildet sich bei einer I/R eine komplexere Narbe in der mittleren Schicht des linken Ventrikels, die von einer jeweils endokardialen und epikardialen Schicht gesunden Myokards umgeben ist [67, 77] .

Wir haben nun im nächsten Schritt versucht, ein anwenderfreundliches Protokoll zu etablieren, mit dem auf Basis einer nativen CINE CMR – auch ohne spezifische radiologische Vorkenntnisse zu besitzen - regionale Analysen der linksventrikulären Wand möglich sind.

Die Grundlage unseres Ansatzes war die Darstellung der linksventrikulären endsystolischen Wanddicke in der sogenannten „bulls-eye“ Ansicht, um ein qualitatives Bild der regionalen Veränderungen im Prozess des LV-Remodeling zu schaffen. In Anlehnung an das 17-Segment-Modell der „American Heart Association“ (AHA) haben wir dann eine segmentale Analyse aller fünf axialen Schichten vorgenommen.

Hinsichtlich der regionalen Wandeigenschaften ergab sich nun ein differenzierteres Bild mit charakteristischen LV-Eigenschaften des jeweiligen Infarktmodells. In beiden Modellen führte eine kompensatorische Hypertrophie zu einer signifikanten Zunahme der septalen Wanddicke, während nur die PL zu einer Ausdünnung der LV-Wand im LAD-Versorgungsgebiet führte. Neben der regionalen Wanddicke, habe wir versucht, auch das radiale „Wall Thickening“ quantitativ zu erfassen. Der Messwert ergibt sich aus der Differenz der jeweils endsystolisch und enddiastolisch gemessenen regionalen Wanddicke. Wie zu erwarten, ließ sich im aneurysmatisch erweiterten Narbenareal der PL Gruppe kein „Wall Thickening“ messen. Interessanterweise blieb in der I/R die Wanddicke im Narbenareal zwar erhalten, allerdings war die radiale Kontraktilität im Vergleich zu gesunden Tieren signifikant reduziert. Ähnliche Beobachtungen konnten andere Gruppen unter Verwendung von „Regional Strain Analysis“ mittels Echokardiographie und T1 „Maps“ in der CMR machen [73, 75]. Damit stellen wir nun eine Methode zur Verfügung, die trotz des Verzichts auf spezielle Techniken in der CMR ein benutzerfreundliches und zuverlässiges Werkzeug für die „Regional Wall Analysis“ im Mausmodell darstellt. Wir sind überzeugt, dass dies vielen Wissenschaftlern helfen wird, den Effekt gezielter Therapien experimentell besser zu erfassen und somit eine Translation in die Klinik zu erleichtern.

5. Zusammenfassung und Schlussfolgerung

Moderne Bildgebungsverfahren, wie die dedizierte Kleintier-PET und -MRT, bieten die Möglichkeit, biologische Prozesse vom Mausmodell bis zum Patienten zu erfassen und haben ein enormes Potential, das Forschungsgebiet der translationalen kardiovaskulären Forschung zu revolutionieren. Die Arbeiten, welcher dieser Habilitation zugrunde liegen, erweitern die Möglichkeiten der Bildgebung von Heilungsprozessen nach einem Herzinfarkt und dem damit verbundenen linksvertrikulären Remodeling im Mausmodell um einen relevanten Schritt. Die von uns etablierten Techniken ermöglichen ein intraindividuelles und longitudinales Monitoring der Heilung nach einem Herzinfarkt im Mausmodell mit dem Potential einer direkten Translation in die Anwendung an Patienten.

6. Literaturverzeichnis

1. Nowbar AN, Gitto M, Howard JP, Francis DP, Al-Lamee R: **Mortality From Ischemic Heart Disease**. *Circ Cardiovasc Qual Outcomes* 2019, **12**(6):e005375.
2. Dai H, Zhang Q, Much AA, Maor E, Segev A, Beinart R, Adawi S, Lu Y, Bragazzi NL, Wu J: **Global, regional, and national prevalence, incidence, mortality, and risk factors for atrial fibrillation, 1990-2017: results from the Global Burden of Disease Study 2017**. *Eur Heart J Qual Care Clin Outcomes* 2020.
3. Mamas MA, Sperrin M, Watson MC, Coutts A, Wilde K, Burton C, Kadam UT, Kwok CS, Clark AB, Murchie P *et al*: **Do patients have worse outcomes in heart failure than in cancer? A primary care-based cohort study with 10-year follow-up in Scotland**. *Eur J Heart Fail* 2017, **19**(9):1095-1104.
4. Orlic D, Kajstura J, Chimenti S, Jakoniuk I, Anderson SM, Li B, Pickel J, McKay R, Nadal-Ginard B, Bodine DM *et al*: **Bone marrow cells regenerate infarcted myocardium**. *Nature* 2001, **410**(6829):701-705.
5. Strauer BE, Brehm M, Zeus T, Gattermann N, Hernandez A, Sorg RV, Kogler G, Wernet P: **[Intracoronary, human autologous stem cell transplantation for myocardial regeneration following myocardial infarction]**. *Dtsch Med Wochenschr* 2001, **126**(34-35):932-938.
6. Murry CE, Soonpaa MH, Reinecke H, Nakajima H, Nakajima HO, Rubart M, Pasumarthi KB, Virag JI, Bartelmez SH, Poppa V *et al*: **Haematopoietic stem cells do not transdifferentiate into cardiac myocytes in myocardial infarcts**. *Nature* 2004, **428**(6983):664-668.
7. Balsam LB, Wagers AJ, Christensen JL, Kofidis T, Weissman IL, Robbins RC: **Haematopoietic stem cells adopt mature haematopoietic fates in ischaemic myocardium**. *Nature* 2004, **428**(6983):668-673.
8. Nygren JM, Jovinge S, Breitbach M, Sawen P, Roll W, Hescheler J, Taneera J, Fleischmann BK, Jacobsen SE: **Bone marrow-derived hematopoietic cells generate cardiomyocytes at a low frequency through cell fusion, but not transdifferentiation**. *Nature medicine* 2004, **10**(5):494-501.
9. Hodgkinson CP, Bareja A, Gomez JA, Dzau VJ: **Emerging Concepts in Paracrine Mechanisms in Regenerative Cardiovascular Medicine and Biology**. *Circ Res* 2016, **118**(1):95-107.
10. Steinhoff G, Nesteruk J, Wolfien M, Kundt G, Group PTI, Borgermann J, David R, Garbade J, Grosse J, Haverich A *et al*: **Cardiac Function Improvement and Bone Marrow Response -: Outcome Analysis of the Randomized PERFECT Phase III Clinical Trial of Intramyocardial CD133(+) Application After Myocardial Infarction**. *EBioMedicine* 2017, **22**:208-224.
11. Marks PW, Witten CM, Califf RM: **Clarifying Stem-Cell Therapy's Benefits and Risks**. *N Engl J Med* 2017, **376**(11):1007-1009.
12. Zwetsloot PP, Vegh AM, Jansen of Lorkeers SJ, van Hout GP, Currie GL, Sena ES, Gremmels H, Buikema JW, Goumans MJ, Macleod MR *et al*: **Cardiac Stem Cell Treatment in Myocardial Infarction: A Systematic Review and Meta-Analysis of Preclinical Studies**. *Circ Res* 2016, **118**(8):1223-1232.
13. van Berlo JH, Kanisicak O, Maillet M, Vagnozzi RJ, Karch J, Lin SC, Middleton RC, Marban E, Molkentin JD: **c-kit+ cells minimally contribute cardiomyocytes to the heart**. *Nature* 2014, **509**(7500):337-341.
14. Vagnozzi RJ, Maillet M, Sargent MA, Khalil H, Johansen AKZ, Schwanekamp JA, York AJ, Huang V, Nahrendorf M, Sadayappan S *et al*: **An acute immune response underlies the benefit of cardiac stem cell therapy**. *Nature* 2020, **577**(7790):405-409.
15. Sadek H, Olson EN: **Toward the Goal of Human Heart Regeneration**. *Cell Stem Cell* 2020, **26**(1):7-16.
16. Huynh K: **Stem cell therapy improves heart function by triggering an acute immune response**. *Nat Rev Cardiol* 2020, **17**(2):69.
17. Frangogiannis NG: **The inflammatory response in myocardial injury, repair, and remodelling**. *Nat Rev Cardiol* 2014, **11**(5):255-265.
18. Epelman S, Liu PP, Mann DL: **Role of innate and adaptive immune mechanisms in cardiac injury and repair**. *Nat Rev Immunol* 2015, **15**(2):117-129.

19. Frangogiannis NG: **The mechanistic basis of infarct healing**. *Antioxid Redox Signal* 2006, **8**(11-12):1907-1939.

20. Nahrendorf M, Swirski FK, Aikawa E, Stangenberg L, Wurdinger T, Figueiredo JL, Libby P, Weissleder R, Pittet MJ: **The healing myocardium sequentially mobilizes two monocyte subsets with divergent and complementary functions**. *J Exp Med* 2007, **204**(12):3037-3047.

21. Bonios M, Terrovitis J, Chang CY, Engles JM, Higuchi T, Lautamaki R, Yu J, Fox J, Pomper M, Wahl RL *et al*: **Myocardial substrate and route of administration determine acute cardiac retention and lung bio-distribution of cardiosphere-derived cells**. *J Nucl Cardiol* 2011, **18**(3):443-450.

22. Lautamaki R, Terrovitis J, Bonios M, Yu J, Tsui BM, Abraham MR, Bengel FM: **Perfusion defect size predicts engraftment but not early retention of intra-myocardially injected cardiosphere-derived cells after acute myocardial infarction**. *Basic Res Cardiol* 2011, **106**(6):1379-1386.

23. Terrovitis J, Lautamaki R, Bonios M, Fox J, Engles JM, Yu J, Leppo MK, Pomper MG, Wahl RL, Seidel J *et al*: **Noninvasive quantification and optimization of acute cell retention by in vivo positron emission tomography after intramyocardial cardiac-derived stem cell delivery**. *J Am Coll Cardiol* 2009, **54**(17):1619-1626.

24. Kolossov E, Bostani T, Roell W, Breitbach M, Pillekamp F, Nygren JM, Sasse P, Rubenchik O, Fries JW, Wenzel D *et al*: **Engraftment of engineered ES cell-derived cardiomyocytes but not BM cells restores contractile function to the infarcted myocardium**. *J Exp Med* 2006, **203**(10):2315-2327.

25. Lang C, Lehner S, Todica A, Boening G, Franz WM, Bartenstein P, Hacker M, David R: **Positron emission tomography based in-vivo imaging of early phase stem cell retention after intramyocardial delivery in the mouse model**. *Eur J Nucl Med Mol Imaging* 2013, **40**(11):1730-1738.

26. Lee WW, Marinelli B, van der Laan AM, Sena BF, Gorbatov R, Leuschner F, Dutta P, Iwamoto Y, Ueno T, Begieneman MP *et al*: **PET/MRI of inflammation in myocardial infarction**. *J Am Coll Cardiol* 2012, **59**(2):153-163.

27. Thackeray JT, Bankstahl JP, Wang Y, Korf-Klingebiel M, Walte A, Wittneben A, Wollert KC, Bengel FM: **Targeting post-infarct inflammation by PET imaging: comparison of (68)Ga-citrate and (68)Ga-DOTATATE with (18)F-FDG in a mouse model**. *Eur J Nucl Med Mol Imaging* 2015, **42**(2):317-327.

28. Thackeray JT, Bankstahl JP, Wang Y, Wollert KC, Bengel FM: **Clinically relevant strategies for lowering cardiomyocyte glucose uptake for 18F-FDG imaging of myocardial inflammation in mice**. *Eur J Nucl Med Mol Imaging* 2015, **42**(5):771-780.

29. Vasudevan P, Gabel R, Stenzel J, Forster J, Kurth J, Vollmar B, Krause BJ, Ince H, David R, Lang CI: **(18)F-FDG PET-Based Imaging of Myocardial Inflammation Following Acute Myocardial Infarction in a Mouse Model**. *Int J Mol Sci* 2020, **21**(9).

30. Cochain C, Channon KM, Silvestre JS: **Angiogenesis in the infarcted myocardium**. *Antioxid Redox Signal* 2013, **18**(9):1100-1113.

31. Tonnesen MG, Feng X, Clark RA: **Angiogenesis in wound healing**. *J Investig Dermatol Symp Proc* 2000, **5**(1):40-46.

32. van der Laan AM, Piek JJ, van Royen N: **Targeting angiogenesis to restore the microcirculation after reperfused MI**. *Nat Rev Cardiol* 2009, **6**(8):515-523.

33. Mandic L, Traxler D, Gugerell A, Zlabinger K, Lukovic D, Pavo N, Goliasch G, Spannbauer A, Winkler J, Gyongyosi M: **Molecular Imaging of Angiogenesis in Cardiac Regeneration**. *Curr Cardiovasc Imaging Rep* 2016, **9**(10):27.

34. Hodivala-Dilke K: **alphavbeta3 integrin and angiogenesis: a moody integrin in a changing environment**. *Curr Opin Cell Biol* 2008, **20**(5):514-519.

35. Horton MA: **The alpha v beta 3 integrin "vitronectin receptor"**. *Int J Biochem Cell Biol* 1997, **29**(5):721-725.

36. Huang CC, Wei HJ, Lin KJ, Lin WW, Wang CW, Pan WY, Hwang SM, Chang Y, Sung HW: **Multimodality noninvasive imaging for assessing therapeutic effects of exogenously transplanted cell aggregates capable of angiogenesis on acute myocardial infarction**. *Biomaterials* 2015, **73**:12-22.

37. Lindsey ML, Escobar GP, Dobrucki LW, Goshorn DK, Bouges S, Mingoia JT, McClister DM, Jr., Su H, Gannon J, MacGillivray C *et al*: **Matrix metalloproteinase-9 gene deletion facilitates angiogenesis after myocardial infarction**. *Am J Physiol Heart Circ Physiol* 2006, **290**(1):H232-239.

38. Sherif HM, Saraste A, Nekolla SG, Weidl E, Reder S, Tapfer A, Rudelius M, Higuchi T, Botnar RM, Wester HJ *et al*: **Molecular imaging of early alphavbeta3 integrin expression predicts long-term left-ventricle remodeling after myocardial infarction in rats**. *J Nucl Med* 2012, **53**(2):318-323.

39. Jenkins WS, Vesey AT, Stirrat C, Connell M, Lucatelli C, Neale A, Moles C, Vickers A, Fletcher A, Pawade T *et al*: **Cardiac alphaVbeta3 integrin expression following acute myocardial infarction in humans**. *Heart* 2017, **103**(8):607-615.

40. Patten RD, Hall-Porter MR: **Small animal models of heart failure: development of novel therapies, past and present**. *Circ Heart Fail* 2009, **2**(2):138-144.
41. Takagawa J, Zhang Y, Wong ML, Sievers RE, Kapasi NK, Wang Y, Yeghiazarians Y, Lee RJ, Grossman W, Springer ML: **Myocardial infarct size measurement in the mouse chronic infarction model: comparison of area- and length-based approaches**. *J Appl Physiol (1985)* 2007, **102**(6):2104-2111.
42. Lindsey ML, Kassiri Z, Virag JAI, de Castro Bras LE, Scherrer-Crosbie M: **Guidelines for measuring cardiac physiology in mice**. *Am J Physiol Heart Circ Physiol* 2018, **314**(4):H733-H752.
43. Lang C, Lehner S, Todica A, Boening G, Zacherl M, Franz WM, Krause BJ, Bartenstein P, Hacker M, David R: **In-vivo comparison of the acute retention of stem cell derivatives and fibroblasts after intramyocardial transplantation in the mouse model**. *Eur J Nucl Med Mol Imaging* 2014, **41**(12):2325-2336.
44. Teng CJ, Luo J, Chiu RC, Shum-Tim D: **Massive mechanical loss of microspheres with direct intramyocardial injection in the beating heart: implications for cellular cardiomyoplasty**. *J Thorac Cardiovasc Surg* 2006, **132**(3):628-632.
45. Hofmann M, Wollert KC, Meyer GP, Menke A, Arseniev L, Hertenstein B, Ganser A, Knapp WH, Drexler H: **Monitoring of bone marrow cell homing into the infarcted human myocardium**. *Circulation* 2005, **111**(17):2198-2202.
46. Kang WJ, Kang HJ, Kim HS, Chung JK, Lee MC, Lee DS: **Tissue distribution of 18F-FDG-labeled peripheral hematopoietic stem cells after intracoronary administration in patients with myocardial infarction**. *J Nucl Med* 2006, **47**(8):1295-1301.
47. Lang CI, Wolfien M, Langenbach A, Muller P, Wolkenhauer O, Yavari A, Ince H, Steinhoff G, Krause BJ, David R *et al*: **Cardiac Cell Therapies for the Treatment of Acute Myocardial Infarction: A Meta-Analysis from Mouse Studies**. *Cell Physiol Biochem* 2017, **42**(1):254-268.
48. Mauritz C, Martens A, Rojas SV, Schnick T, Rathert C, Schecker N, Menke S, Glage S, Zweigerdt R, Haverich A *et al*: **Induced pluripotent stem cell (iPSC)-derived Flk-1 progenitor cells engraft, differentiate, and improve heart function in a mouse model of acute myocardial infarction**. *Eur Heart J* 2011, **32**(21):2634-2641.
49. Cao N, Liu Z, Chen Z, Wang J, Chen T, Zhao X, Ma Y, Qin L, Kang J, Wei B *et al*: **Ascorbic acid enhances the cardiac differentiation of induced pluripotent stem cells through promoting the proliferation of cardiac progenitor cells**. *Cell Res* 2012, **22**(1):219-236.
50. Rimmbach C, Jung JJ, David R: **Generation of murine cardiac pacemaker cell aggregates based on ES-cell-programming in combination with Myh6-promoter-selection**. *J Vis Exp* 2015(96):e52465.
51. Love C, Tomas MB, Tronco GG, Palestro CJ: **FDG PET of infection and inflammation**. *Radiographics* 2005, **25**(5):1357-1368.
52. Rischpler C, Dirschinger RJ, Nekolla SG, Kossmann H, Nicolosi S, Hanus F, van Marwick S, Kunze KP, Meinicke A, Gotze K *et al*: **Prospective Evaluation of 18F-Fluorodeoxyglucose Uptake in Postischemic Myocardium by Simultaneous Positron Emission Tomography/Magnetic Resonance Imaging as a Prognostic Marker of Functional Outcome**. *Circ Cardiovasc Imaging* 2016, **9**(4):e004316.
53. Vasudevan P, Gaebel R, Doering P, Mueller P, Lemcke H, Stenzel J, Lindner T, Kurth J, Steinhoff G, Vollmar B *et al*: **18F-FDG PET-Based Imaging of Myocardial Inflammation Predicts a Functional Outcome Following Transplantation of mESC-Derived Cardiac Induced Cells in a Mouse Model of Myocardial Infarction**. *Cells* 2019, **8**(12).
54. van Furth R, Cohn ZA: **The origin and kinetics of mononuclear phagocytes**. *J Exp Med* 1968, **128**(3):415-435.
55. Aurora AB, Porrello ER, Tan W, Mahmoud AI, Hill JA, Bassel-Duby R, Sadek HA, Olson EN: **Macrophages are required for neonatal heart regeneration**. *J Clin Invest* 2014, **124**(3):1382-1392.
56. Aurora AB, Olson EN: **Immune modulation of stem cells and regeneration**. *Cell Stem Cell* 2014, **15**(1):14-25.
57. Lavine KJ, Epelman S, Uchida K, Weber KJ, Nichols CG, Schilling JD, Ornitz DM, Randolph GJ, Mann DL: **Distinct macrophage lineages contribute to disparate patterns of cardiac recovery and remodeling in the neonatal and adult heart**. *Proc Natl Acad Sci U S A* 2014, **111**(45):16029-16034.
58. Ben-Mordechai T, Holbova R, Landa-Rouben N, Harel-Adar T, Feinberg MS, Abd Elrahman I, Blum G, Epstein FH, Silman Z, Cohen S *et al*: **Macrophage subpopulations are essential for infarct repair with and without stem cell therapy**. *J Am Coll Cardiol* 2013, **62**(20):1890-1901.
59. Hendrikx G, Voo S, Bauwens M, Post MJ, Mottaghy FM: **SPECT and PET imaging of angiogenesis and arteriogenesis in pre-clinical models of myocardial ischemia and peripheral vascular disease**. *Eur J Nucl Med Mol Imaging* 2016, **43**(13):2433-2447.

60. Higuchi T, Bengel FM, Seidl S, Watzlowik P, Kessler H, Hegenloh R, Reder S, Nekolla SG, Wester HJ, Schwaiger M: Assessment of alphavbeta3 integrin expression after myocardial infarction by positron emission tomography. *Cardiovasc Res* 2008, **78**(2):395-403.
61. Gao H, Lang L, Guo N, Cao F, Quan Q, Hu S, Kiesewetter DO, Niu G, Chen X: PET imaging of angiogenesis after myocardial infarction/reperfusion using a one-step labeled integrin-targeted tracer 18F-AlF-NOTA-PRGD2. *Eur J Nucl Med Mol Imaging* 2012, **39**(4):683-692.
62. Hedhli J, Slania SLL, Ploska A, Czerwinski A, Konopka CJ, Wozniak M, Banach M, Dobrucki IT, Kalinowski L, Dobrucki LW: Evaluation of a dimeric-cRGD peptide for targeted PET-CT imaging of peripheral angiogenesis in diabetic mice. *Sci Rep* 2018, **8**(1):5401.
63. Hua J, Dobrucki LW, Sadeghi MM, Zhang J, Bourke BN, Cavaliere P, Song J, Chow C, Jahanshad N, van Royen N *et al*: Noninvasive imaging of angiogenesis with a 99mTc-labeled peptide targeted at alphavbeta3 integrin after murine hindlimb ischemia. *Circulation* 2005, **111**(24):3255-3260.
64. van den Borne SW, Isobe S, Verjans JW, Petrov A, Lovhaug D, Li P, Zandbergen HR, Ni Y, Frederik P, Zhou J *et al*: Molecular imaging of interstitial alterations in remodeling myocardium after myocardial infarction. *J Am Coll Cardiol* 2008, **52**(24):2017-2028.
65. Savill J, Dransfield I, Hogg N, Haslett C: Vitronectin receptor-mediated phagocytosis of cells undergoing apoptosis. *Nature* 1990, **343**(6254):170-173.
66. Virag JI, Murry CE: Myofibroblast and endothelial cell proliferation during murine myocardial infarct repair. *Am J Pathol* 2003, **163**(6):2433-2440.
67. Vandervelde S, van Amerongen MJ, Tio RA, Petersen AH, van Luyn MJ, Harmsen MC: Increased inflammatory response and neovascularization in reperfused vs. non-reperfused murine myocardial infarction. *Cardiovasc Pathol* 2006, **15**(2):83-90.
68. Minatoguchi S, Takemura G, Chen XH, Wang N, Uno Y, Koda M, Arai M, Misao Y, Lu C, Suzuki K *et al*: Acceleration of the healing process and myocardial regeneration may be important as a mechanism of improvement of cardiac function and remodeling by postinfarction granulocyte colony-stimulating factor treatment. *Circulation* 2004, **109**(21):2572-2580.
69. Pfeffer MA, Pfeffer JM, Fishbein MC, Fletcher PJ, Spadaro J, Kloner RA, Braunwald E: Myocardial infarct size and ventricular function in rats. *Circ Res* 1979, **44**(4):503-512.
70. Chareonthaitawee P, Christian TF, Hirose K, Gibbons RJ, Rumberger JA: Relation of initial infarct size to extent of left ventricular remodeling in the year after acute myocardial infarction. *J Am Coll Cardiol* 1995, **25**(3):567-573.
71. Konstam MA, Kramer DG, Patel AR, Maron MS, Udelson JE: Left ventricular remodeling in heart failure: current concepts in clinical significance and assessment. *JACC Cardiovasc Imaging* 2011, **4**(1):98-108.
72. Vanhoutte L, Gerber BL, Gallez B, Po C, Magat J, Balligand JL, Feron O, Moniotte S: High field magnetic resonance imaging of rodents in cardiovascular research. *Basic Res Cardiol* 2016, **111**(4):46.
73. Soepriatna AH, Yeh AK, Clifford AD, Bezci SE, O'Connell GD, Goergen CJ: Three-dimensional myocardial strain correlates with murine left ventricular remodelling severity post-infarction. *J R Soc Interface* 2019, **16**(160):20190570.
74. Pluijmert NJ, Bart CI, Bax WH, Quax PHA, Atsma DE: Effects on cardiac function, remodeling and inflammation following myocardial ischemia-reperfusion injury or unreperfused myocardial infarction in hypercholesterolemic APOE*3-Leiden mice. *Sci Rep* 2020, **10**(1):16601.
75. Haberkorn SM, Jacoby C, Ding Z, Keul P, Bonner F, Polzin A, Levkau B, Schrader J, Kelm M, Flogel U: Cardiovascular Magnetic Resonance Relaxometry Predicts Regional Functional Outcome After Experimental Myocardial Infarction. *Circ Cardiovasc Imaging* 2017, **10**(8).
76. MacIver DH, Dayer MJ: An alternative approach to understanding the pathophysiological mechanisms of chronic heart failure. *Int J Cardiol* 2012, **154**(2):102-110.
77. De Celle T, Cleutjens JP, Blankesteijn WM, Debets JJ, Smits JF, Janssen BJ: Long-term structural and functional consequences of cardiac ischaemia-reperfusion injury in vivo in mice. *Exp Physiol* 2004, **89**(5):605-615.

7. Liste der eigenen Publikationen

Der angegebene Impact-Faktor (IF) bezieht sich auf das Erscheinungsjahr der jeweiligen Arbeit.

7.1. Originalarbeiten die der kumulativen Habilitation zugrunde liegen

Lang C, Lehner S, Todica A, Boening G, Zacherl M, Franz WM, Krause BJ, Bartenstein P, Hacker M, David R: ***In-vivo* comparison of the acute retention of stem cell derivatives and fibroblasts after intramyocardial transplantation in the mouse model**. *Eur J Nucl Med Mol Imaging* 2014, **41**(12):2325-2336 (IF: 6,065)

Vasudevan P, Gaebel R, Doering P, Mueller P, Lemcke H, Stenzel J, Lindner T, Kurth J, Steinhoff G, Vollmar B, Krause BJ, Ince H, David R, Lang C: **^{18}F-FDG PET-Based Imaging of Myocardial Inflammation Predicts a Functional Outcome Following Transplantation of mESC-Derived Cardiac Induced Cells in a Mouse Model of Myocardial Infarction.** Cells 2019, 8(12). (IF: 4,366)

Vasudevan P, Gabel R, Stenzel J, Forster J, Kurth J, Vollmar B, Krause BJ, Ince H, David R, Lang C: **^{18}F-FDG PET-Based Imaging of Myocardial Inflammation Following Acute Myocardial Infarction in a Mouse Model**. *Int J Mol Sci* 2020, **21**(9). (IF: 4,556)

Lang C, Doring P, Gabel R, Vasudevan P, Lemcke H, Muller P, Stenzel J, Lindner T, Joksch M, Kurth J, Bergner C, Wester H, Ince H, Steinhoff G, Vollmar B, David R, Krause B: **^{68}Ga-NODAGA-RGD Positron Emission Tomography (PET) for Assessment of Post Myocardial Infarction Angiogenesis as a Predictor for Left Ventricular Remodeling in Mice after Cardiac Stem Cell Therapy**. *Cells* 2020, **9**(6). (IF: 4,366)

Lang CI, Vasudevan P, Doring P, Gabel R, Lemcke H, Lindner T, Steinhoff G, Krause BJ, Vollmar B, Meinel FG *et al*: **Expedient assessment of post-infarct remodeling by native cardiac magnetic resonance imaging in mice**. *Sci Rep* 2021, **11**(1):11625. (IF 3,998).

7.2. Weitere ausgewählte Originalarbeiten zur Thematik

Lang C*, Lehner S*, Todica A, Boening G, Franz W, Bartenstein P, Hacker M, David R: **Positron emission tomography based in-vivo imaging of early phase stem cell retention after intramyocardial delivery in the mouse model**. *Eur J Nucl Med Mol Imaging* 2013, **40**(11):1730-1738. (IF 5,514)

*contributed equally.

Lehner S*, Lang C*, Kaissis G, Todica A, Zacherl M, Boening G, Spitzweg C, Herbach N, Franz WM, Krause B, Steinhoff G, Bartenstein P, Hacker M, David R: **(124)I-PET Assessment of Human Sodium Iodide Symporter Reporter Gene Activity for Highly Sensitive In Vivo Monitoring of Teratoma Formation in Mice**. *Mol Imaging Biol* 2015, **17**(6):874-883. (IF 2,82)

*contributed equally.
Lang C*, Wolfien M*, Langenbach A, Muller P, Wolkenhauer O, Yavari A, Ince H, Steinhoff G, Krause BJ, David R, Glass A: **Cardiac Cell Therapies for the Treatment of Acute Myocardial Infarction: A Meta-Analysis from Mouse Studies**. *Cell Physiol Biochem* 2017, **42**(1):254-268. (IF 5,5)

*contributed equally.

Muller P, Gaebel R, Lemcke H, Wiekhorst F, Hausburg F, Lang C, Zarniko N, Westphal B, Steinhoff G, David R: **Intramyocardial fate and effect of iron nanoparticles co-injected with MACS® purified stem cell products.** Biomaterials 2017, 135:74-84. (IF 9,394)

Lemcke H, Skorska A, Lang C, Johann L, David R: **Quantitative Evaluation of the Sarcomere Network of Human hiPSC-Derived Cardiomyocytes Using Single-Molecule Localization Microscopy.** Int J Mol Sci 2020, 21(8). (IF: 4,556)

Vasudevan P, Wolfien M, Lemcke H, Lang C, Skorska A, Gaebel R, Koczan D, Lindner T, Engelmann R, Vollmar B *et al*: **Cardiomyocyte Transplantation after Myocardial Infarction Alters the Immune Response in the Heart**. *Cells* 2020, **9**(8). (IF: 4,366)

Johann L, Chabanovska O, Lang C, David R, Lemcke H: **Analyzing the alpha-Actinin Network in Human iPSC-Derived Cardiomyocytes Using Single Molecule Localization Microscopy**. *J Vis Exp* 2020(165). (IF 1,2)

Mueller P, Wolfien M, Ekat K, Lang C, Koczan D, Wolkenhauer O, Hahn O, Peters K, Lang H, David R, Lemcke H: **RNA-Based Strategies for Cardiac Reprogramming of Human Mesenchymal Stromal Cells**. *Cells* 2020, **9**(2). (IF: 4,366)

Bottcher B, Lorbeer R, Stocklein S, Beller E, Lang CI, Weber MA, Meinel FG: **Global and Regional Test-Retest Reproducibility of Native T1 and T2 Mapping in Cardiac Magnetic Resonance Imaging**. *J Magn Reson Imaging* 2021. (IF: 4,813)

7.3. Editorial

Lang C, Krause B, David R: **Cardiac FDG-PET: a straight forward tool with high potential**. *Eur Heart J Cardiovasc Imaging* 2016, **17**(2):130-131 (IF: 5,404)

7.4. Buchartikel

Chapter 9: Imaging Technology in Regenerative Medicine – from Protocol to Patient (Editor: Gustav Steinhoff; Springer International Publishing Switzerland 2016). DOI 10.1007/978-3-319-28274-9_9

8. Originalarbeiten der Habilitationsschrift

Eur J Nucl Med Mol Imaging (2014) 41:2325–2336
DOI 10.1007/s00259-014-2858-8

ORIGINAL ARTICLE

In-vivo comparison of the acute retention of stem cell derivatives and fibroblasts after intramyocardial transplantation in the mouse model

Cajetan Lang · Sebastian Lehner · Andrei Todica · Guido Boening · Mathias Zacherl · Wolfgang-Michael Franz · Bernd Joachim Krause · Peter Bartenstein · Marcus Hacker · Robert David

Received: 8 January 2014 / Accepted: 4 July 2014 / Published online: 26 July 2014

Abstract

Purpose Various strategies have been applied to increase the engraftment of an intramyocardial cell transplant (Tx) to treat ischemic myocardium. Thereby, co-transplanted fibroblasts (FB) improve the long-term survival of stem cell derivatives (SCD) in a murine model of myocardial infarction. For therapeutic use, the time frame in which FB exert putative supportive effects needs to be identified. Therefore, we tracked the biodistribution and retention of SCD and FB in vivo using highly sensitive positron emission tomography (PET) imaging.

Methods Murine [^{18}F]-fluorodeoxyglucose (FDG) labeled SCD and FB were transplanted after left anterior descending artery (LAD) ligation into the border zone of the ischemic area in female C57BL/6 mice. Cardiac retention and biodistribution during the initial 2 h after injection were measured via PET imaging.

Results Massive initial cell loss occurred independently of the cell type. Thereby, FB were retained slightly, yet significantly better than SCD until 60 min post-injection (7.5±1.7 vs. 5.2±0.7 % ID at 25 min and 7.0±1.5 vs. 4.8±0.8 % ID at 60 min). Thereafter, a fraction of ~5 % that withstood the massive initial washout remained at the site of injection independently of the applied cell type (120 min, SCD vs. FB $P=0.64$). Most of the lost cells were detected in the lungs (~30 % ID).

Conclusions We were able to quantitatively define the retention and biodistribution of different cell types via PET imaging in a mouse model after intramyocardial Tx. The utmost accuracy was achieved through this cell- and organ-specific approach by correcting PET data for cellular FDG efflux. Thereby, we observed a massive initial cell loss of ~95 %, causing low rates of long-term engraftment for both SCD and FB. We conclude that FB are not privileged compared to SCD regarding their acute retention kinetics, and therefore exert their beneficial effects at a later time point.

Keywords MicroPET · Cell tracking · Mouse · Myocardial infarction

Abbreviations and acronyms

SCD	Stem cell derivatives
FB	Fibroblasts
PET	Positron emission tomography
FDG	[18 F]-fluorodeoxyglucose
LAD	Left anterior descending artery
BMSC	Bone marrow stem cells
iPS	Induced pluripotent stem cells

Marcus Hacker and Robert David share senior authorship.

C. Lang · R. David (✉)
Reference and Translation Center for Cardiac Stem Cell Therapy (RTC), University of Rostock, Rostock, Germany
e-mail: robert.david@med.uni-rostock.de

S. Lehner · A. Todica · G. Boening · M. Zacherl · P. Bartenstein
Department of Nuclear Medicine, Ludwig-Maximilians, University of Munich, Munich, Germany

W.-M. Franz
Department of Cardiology, University of Innsbruck, Innbruck, Austria

M. Hacker (✉)
Division of Nuclear Medicine, Department of Biomedical Imaging and Image-guided Therapy, Medical University of Vienna, Währinger Gürtel 18-20, 1090 Wien, Austria
e-mail: marcus.hacker@meduniwien.ac.at

B. J. Krause
Department of Nuclear Medicine, University of Rostock, Rostock, Germany

ESC	Embryonic stem cells
DMEM	Dulbecco's modified Eagle's medium
PBS	Phosphate buffered saline
MI	Myocardial infarction
VOI	Volume of interest
%ID	Percentage of the injected dose
OSEM 3D	Ordered subset expectation maximization
MAP	Ordinary-poisson maximum a-priori

Introduction

Cardiac transplantation is currently the only causal therapy for end-stage congestive heart failure following myocardial infarction. Taking into account the growing gap between urgently needed donor organs and their limited numbers available for transplantation [1], cellular cardiomyoplasty is a promising alternative approach [2]. The efficacy and feasibility of both the intramyocardial and intracoronary delivery of autologous bone marrow stem cells (BMSC) have already been confirmed in meta-analyses of randomized clinical trials [3, 4]. Mechanisms underlying the respective therapeutic benefit are ascribed to the alleged paracrine effects resulting in enhanced angiogenesis and neovascularization [5].

Yet, in order to ultimately restore the systolic function of damaged myocardium, lost tissue needs to be replaced by contractile cells. Due to their pro-arrhythmogenic potential, the safety of autologous skeletal myoblast transplantation was recently challenged [6]. In contrast, the delivery of fetal or embryonic stem cell (ESC)-derived cardiomyocytes led to a significantly improved contractile function of the heart in small-animal models [7, 8]. Thereby, both long-term retention and therapeutic response could be enhanced by the co-transplantation of fibroblasts (FB), even though no positive effects were observed after the sole application of the latter [7, 9]. Cardiac fibroblasts play an important role in cardiac vessel homeostasis [10] and the propagation of force from cardiomyocytes to the surrounding extracellular matrix [11]. Both mechanisms suggest supportive rather than direct effects of fibroblasts.

Novel methods are needed to elucidate cell-specific mechanisms underlying the respective effect leading to an improved cardiac function. Molecular imaging was introduced as a versatile technology for quantitative in-vivo cell tracking following intramyocardial delivery in the mouse model [12]. However, frequently applied bioluminescence imaging is not applicable for the assessment of acute retention following myocardial delivery. Yet, various studies using the rat model suggested that massive cell loss occurs within the first hour following injection [13–15]. Our group recently equipped the mouse with an appropriate positron emission tomography (PET)-based method for quantitative cell-tracking of the initial cell fate, coming up with similar findings for this small-rodent model [16]. Based on this result, we compared the acute retention kinetics of SCD and FB to define the time frame during which initial supportive effects through co-transplantation might be exerted. To our knowledge, this is the first study using PET imaging to compare the acute retention and biodistribution of different cell types in the mouse model after intramyocardial Tx.

Material and methods

Cell culture

Murine embryonic stem cells (ESC) (GSES) [17] were cultured according to standard protocols as described previously [18]. Briefly, ESC were grown in high-glucose Dulbecco's modified Eagle's medium (DMEM) supplemented with 10 % heat-inactivated ESC-qualified fetal calf serum, 2 mM L-glutamine, 50 U/ml penicillin, 50 μg/ml streptomycin, 1× nonessential amino acids, 0.4 mg/ml Geneticin (G418), and 0.1 mM β-mercaptoethanol. To maintain undifferentiated ESC under feeder-free conditions, we applied 1,000 U/ml of purified recombinant mouse leukaemia inhibitory factor.

Fibroblasts were prepared from Imprinting Control Region (ICR) mouse embryos (ED 13.5) using standard protocols [19] and grown in high-glucose Dulbecco's modified Eagle's medium (DMEM) supplemented with 10 % fetal calf serum, 2 mM L-glutamine, 50 U/ml penicillin, 50 μg/ml streptomycin, and 1×nonessential amino acids. Cells were kept at 37 °C in a humidified atmosphere of 5 % CO_2/95 % air. When a confluence of 70–80 % was reached, monolayers were passaged by trypsinization.

Cell-labeling with FDG

3×10^6 ESC and FB were labeled with 0.1 MBq FDG, respectively, as previously described in detail [16]. Trypan blue staining was used to ensure the viability of applied cells. Cells were washed in phosphate buffered saline (PBS) and dissolved in 20 μl saline for transplantation.

Stability of radiolabeling

SCD and FB were labeled as described above and washed three times with PBS. Subsequently, DMEM containing 5 mM glucose was added to mimic in-vivo glucose concentrations. Then, 0, 60, and 120 min after radiolabeling, intracellular FDG retention and FDG in the supernatant were measured using a gamma counter. Intracellular retention was expressed as the percentage of the initially measured cellular FDG uptake after completing the labeling procedure.

Animal surgery and intramyocardial injection

Permanent occlusion of the left anterior descending artery (LAD) was performed in 15 female C57BL6/N wild-type mice (Charles River Laboratories, Sulzbach, Germany) weighing 18–25 g to induce myocardial (MI) infarction as described previously [20]. Five minutes after LAD occlusion, 3×10^6 cells (SCD: n=5, FB: n=5) suspended in 20 µl PBS (containing 0.1 MBq FDG) and 0.8 MBq of free FDG (n=5) were injected into three sites within the border zone of the MI, respectively, using a Hamilton syringe as described by van Laake et al [21]. Experimental protocols were approved by the regional governmental commission of animal protection (Regierung von Oberbayern, Germany) and were performed according to the Guide for the Care and Use of Laboratory Animals published by the US National Institutes of Health (NIH Publication No. 85–23, revised 1996).

PET imaging

PET images were acquired on a dedicated small-animal PET scanner (Inveon Dedicated PET; Preclinical Solutions, Siemens Healthcare Molecular Imaging, Knoxville, TN). Following the surgical intervention and cell injection, the anesthetized animals were transferred to the PET scanner. Images from transplanted cells were obtained as three-dimensional, dynamic list-mode acquisitions lasting 120 min. For the allocation of anatomical structures and the delineation of the area of the MI and the lungs, free FDG (20 MBq) was injected into a tail vein and a list-mode PET image lasting 30 min was acquired. The animals were then killed. All data were processed with an Inveon Acquisition Workplace (Siemens Medical Solutions, Knoxville, TN). For reconstruction details refer to [16].

Image analysis

An Inveon Research Workplace (Siemens Medical Solutions, Knoxville, TN) was used to analyze the obtained images. Dynamic images of transplanted cells were fused with static scans following application of free FDG. Thus, the injected cells could be allocated to the respective anatomical structure. After visual verification of an appropriate alignment by an experienced reader, standardized volumes of interest (VOI) were drawn over the respective region of cell delivery, the lungs, brain, and bladder. For quantitative analysis, a total-body VOI was drawn to measure the net injected activity, corresponding to the 3×10^6 cells applied in each animal. The percentage of the injected dose (%ID) in the organ of interest could then be calculated as the ratio of radioactivity in the respective organ VOI and radioactivity in the total-body VOI. Obtained values were corrected for FDG efflux. For further qualitative analysis of organ activities, representative VOIs were drawn on the dynamic images around the lungs, brain, and bladder to generate time–activity curves.

Statistics

Comparisons between two groups were performed using the unpaired t test when appropriate. Values are shown as mean± SEM or SD, as indicated in the respective figure legends. Values of $p<0.05$ were considered statistically significant.

Results

Stability of radiolabeling

The amount of intracellular FDG retention was measured at 25 min, 60 min, and 120 min after the labeling procedure for both SCD and FB. In SCD the intracellular FDG retention was 91±1.4 % at 25 min, 74±1.2 % at 60 min, and 55±0.5 % at 120 min. In FB the intracellular FDG retention rate was 35± 5.3 % at 25 min, 31±5.2 % at 60 min, and 27±5.9 % at 120 min (Fig. 1). The kinetics of intracellular FDG retention differed significantly between PSC and FB (25 min: P=0.005, 60 min: P=0.001, 120 min: P=0.009). For the experiments described below, cellular retention rates at the site of the injection measured via PET were corrected for the released amount of radiotracer at the respective time point, as described previously [16].

Biodistribution of free FDG

The experiments described above revealed a significant and cell-type-specific efflux of initially cell-bound FDG. To analyze the influence of this released free FDG on quantitative PET data from cell transplantation groups, we visualized and measured the biodistribution of free FDG following intramyocardial injection of the radiotracer. Whereas FDG uptake was low at the site of injection, as well as in the brain, we observed remarkable activities in the area of the lungs and the bladder, respectively (Fig. 2a).

Heart Retention rates of free FDG at the site of injection were 1.5±0.6 % ID at 25 min, 1.3±0.5 % ID at 60 min, and 0.9± 0.5 % ID at 120 min. These values are significantly lower than the retention rates of both SCD and FB ($p<0.0005$) (Fig. 2b).

Brain and bladder Activity in the brain was low (2.3±1.0 %ID at 25 min, 2.0±0.9 %ID at 60 min, 1.6±0.6 %ID at 120 min), whereas an accumulation of activity was observed in the bladder (8.4±5.1 %ID at 25 min, 11.4±6.3 %ID at 60 min, 13.0±6.6 at 120 min) (Fig. 2a).

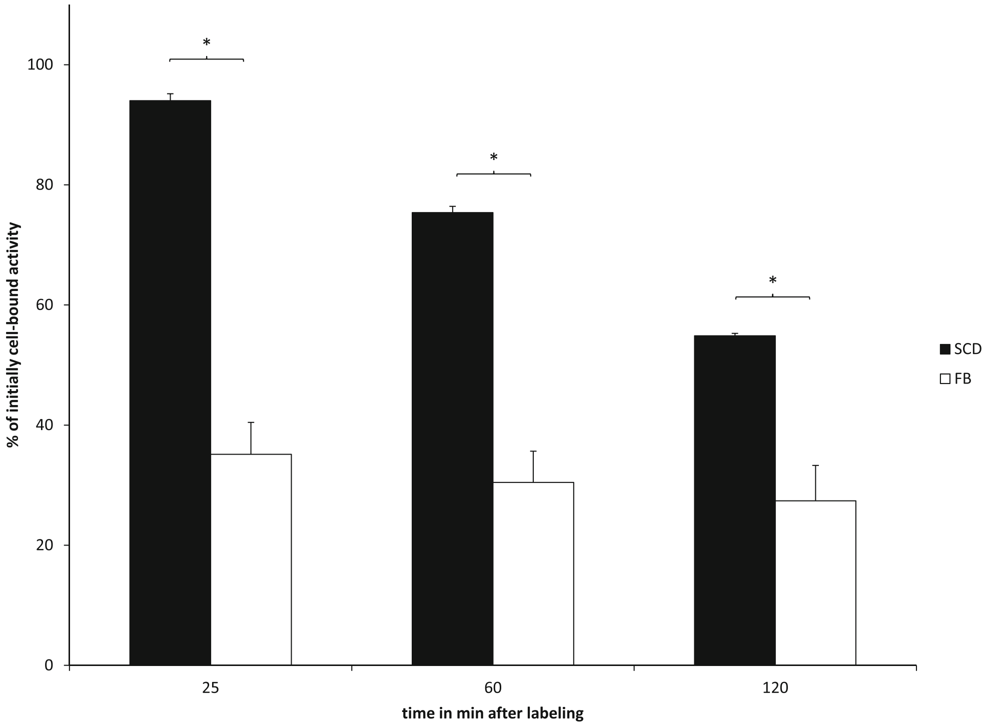

Fig. 1 Cell-specific efflux of FDG within the first 2 h after the labeling procedure. Intracellular-retained FDG is shown at 25 min, 60 min, and 120 min (*n*=3 for each cell type) after the labeling procedure in SCD and FB. The kinetics of intracellular FDG retention differed significantly between SCD and FB (25 min: *P*=0,005, 60 min: *P*=0.001, 120 min: *P*=0.009). Data are presented as mean±SEM. (*=statistically significant)

Lungs Activity in the area of the lungs was~7 %ID (7.7±2,1 %ID at 25 min, 7.2±1.9 %ID at 60 min, 7.4±2.0 %ID at 120 min) during the measured time period without significant changes (25 vs. 60 min: *P*=0.65, 60 vs. 120 min: *P*=0.85) (Fig. 2a). Consecutive cell tracking experiments were corrected for this background signal in the area of the lungs, thus ensuring the clear allocation of activity to transplanted cells.

Biodistribution of FDG following cellular transplantation

Time–activity curves generated from dynamic PET acquisitions confirmed the in-vitro observed, cell-specific FDG retention, thus suggesting that cellular FDG retention rates assessed in vitro can be transferred to our in-vivo model.

The activity concentration (AC) was low and stable in the brain for both SCD and FB, whereas in the lungs it decreased over the measured time period. In contrast, AC increased constantly in the bladder. Activity accumulation in the bladder was considerably more pronounced in animals who received FB, reflecting the higher release of free FDG (Fig. 3).

Cellular retention in the heart and lungs

The acquisition of anatomical landmarking scans enabled us to attribute activity measured in the dynamic scans to the respective organ of interest (Figs. 4 and 5). Thereby, the injected activity was clearly located in the border zone of the myocardial infarction (Fig. 6).

Injection site Retention rates for SCD were 5.2±0.7 %ID at 25 min, 4.8±0.8 %ID at 60 min, and 5.6±1.5 %ID at 120 min. For FB, the measured values were 7.5±1.7 %ID at 25 min, 7.0 ±1.5 %ID at 60 min, and 6.2±1.1 %ID at 120 min. Hence, until 60 min after cell transplantation, FBs were significantly better retained at the injection site than SCD, whereas retention rates did not differ any more at 120 min post-injection (Fig. 7). This indicates a cell-specific behavior during the first hour comprising the initial phase of massive cell loss. Intriguingly, a fraction of~5 % that withstood this massive initial washout [16] remained at the site of injection independently of the applied cell type (120 min, SCD vs. FB *P*=0.64).

Lungs The majority of both cell types was located in the lungs (Figs. 4 and 5). Measured values for SCD were 36±5.5 %ID at 25 min, 28±5.1 %ID at 60 min, and 24±4.3 %ID at 120 min. For FB, the measured values were 35±9.1 %ID at 25 min, 30±7.9 % ID at 60 min, and 23±5.7 %ID at 120 min. We did not observe any significant difference in lung retention rates between SCD and FB at the respective time points (Fig. 8).

Discussion

Strategies to improve the engraftment and effectiveness of intramyocardial cell transplant

Cellular survival is an indispensable prerequisite for efficient cardiac stem cell therapies. According to Teng et al., effective

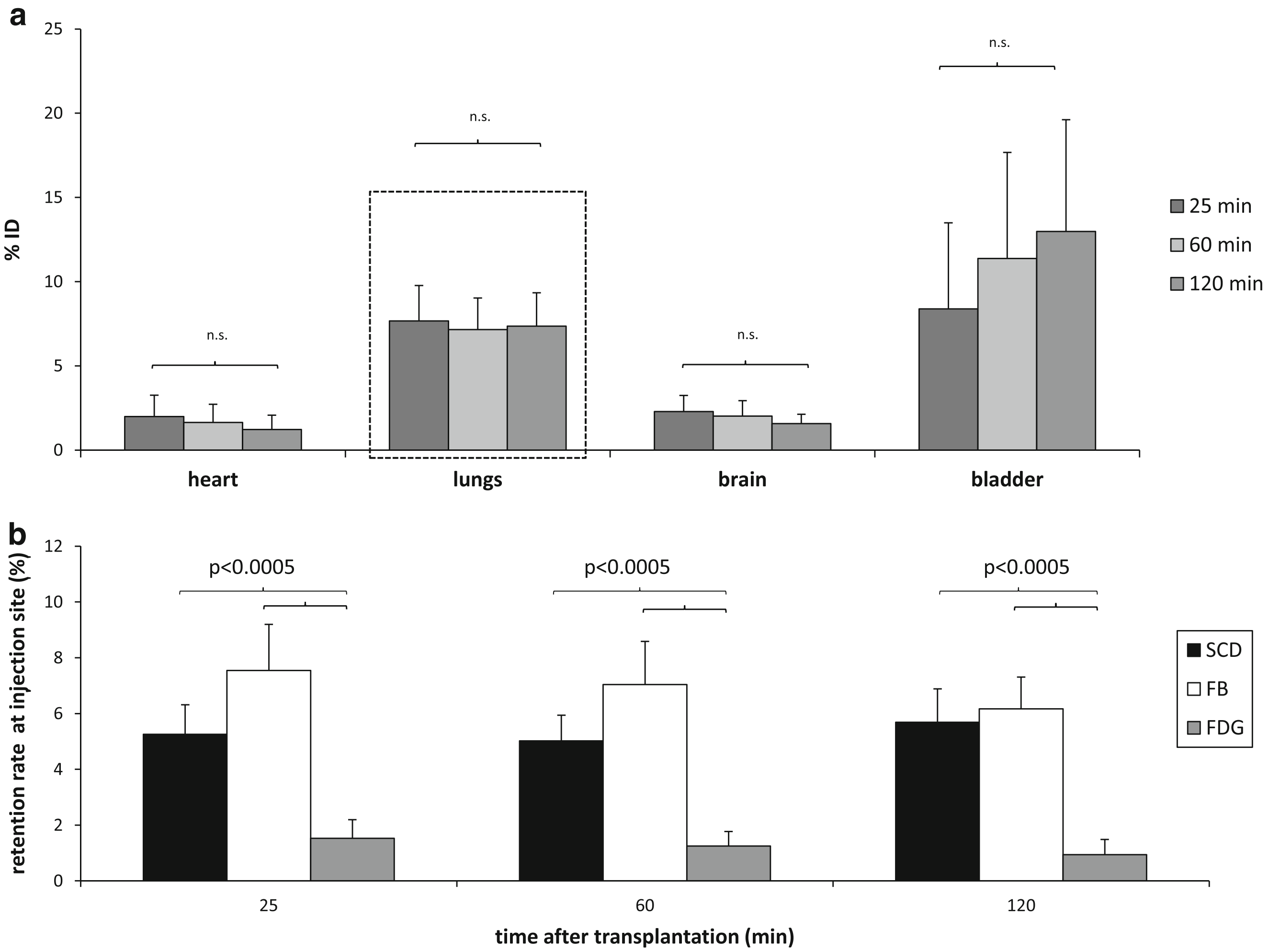

Fig. 2 Biodistribution of free FDG following intramyocardial injection and retention rates at the site of injection; SCD, FB, and free FDG. **a** Free FDG (0.8 MBq) was injected intramyocardially into the border zone after surgical MI induction. Biodistribution of the radiotracer was measured and visualized until 120 min after injection. Obtained data were used to analyze the influence of this released free FDG on quantitative PET data from cell transplantation groups. Whereas FDG uptake was low at the site of injection and in the brain, we observed remarkable activity in the area of the lungs (~7 %) and the bladder, respectively. The data are presented as the mean±SD (n.s. = not significant). **b** Retention rates of free FDG at the site of injection were 1.5±0.6 % ID at 25 min, 1.3±0.5 % ID at 60 min, and 0.9±0.5 % ID at 120 min. These values are significantly lower than the retention rates of both SCD and FB (*p* 0.0005). The data are presented as the mean±SD

engraftment is hampered by specific and time-dependent factors [22]. According to this model, cellular fate can be divided into three phases (Fig. 9). **Phase I** is dominated by an acute cell loss of ~90 % due to mechanical washout [14, 13, 16]. The respective pathological mechanisms underlying further cell loss in **Phase II** are of a biological nature. The retained cells are exposed to a milieu dominated by inflammation, anoikis, and ischemia, ultimately leading to cell death [23]. The surviving cell fraction unfolds its specific therapeutic effect during **Phase III**.

While the above-mentioned model applies to small- and large-animal models, similar low engraftment rates were observed in clinical applications [24]. Yet, meta-analyses of current studies revealed an left ventricular ejection fraction (LVEF) improvement of 3–5 % [4, 3], which is in a similar range as can be achieved by the well-established standard treatment of acute myocardial infarction [25]. Therefore, it seems appropriate to reason that a moderately elevated cardiac function may lead to a considerably improved clinical outcome [26]. Against this background, the respective key trials that established these treatment regimens have led to profound changes in medical practice [26].

Intriguingly, a meta-analysis performed by Martin-Rendon et al. identified the number of transplanted cells to be of utmost importance for an improvement of LVEF [27]. These findings were further corroborated by recent animal studies revealing the importance of the long-term physical presence of therapeutic cells in the host tissue [28, 29]. Against the background that very low cellular engraftment is a commonly assumed phenomenon, we conclude that increased cellular retention could considerably enhance the efficacy of cardiac stem cell therapies.

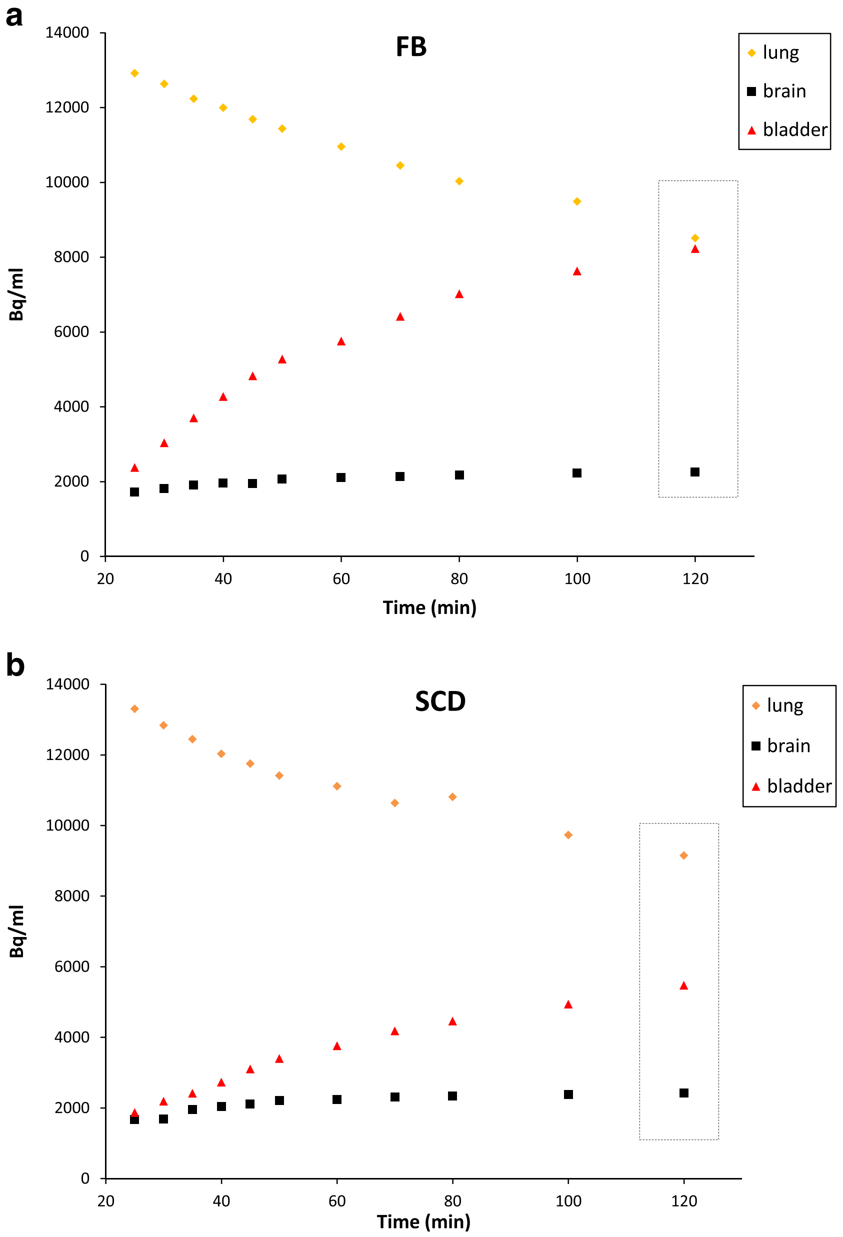

Fig. 3 Time–activity curves (TAC) for the lungs, brain, and bladder after the injection of SCD and FB. Cell-bound FDG in the lungs decreases over the measured time period, whereas free FDG accumulates in the bladder. Higher release of free FDG from a FB compared to b SCD is indicated by a more pronounced increase of activity in the bladder. The uptake of free FDG in the brain was low and stable for both SCD and FB

Effective approaches target specific burdens in the respective phases of the transplanted cells' fate (Fig. 9). Mechanical washout in **Phase I** has been reduced by the application of fibrin glue or cardiac arrest [13]. Biological burdens in **Phase II** might be overcome by modifying the apoptose-inducing milieu [23].

Kolossov et al. reported enhanced long-term engraftment of ESC-derivatives by co-transplanting fibroblasts. This positive effect was ascribed to cell–cell interactions of therapeutic cells with the co-transplanted FB, and would therefore be attributed to **Phase III** (Fig. 9).

Addressing the issue of cellular retention in the mouse model using PET-based in-vivo monitoring, we show here that FB and SCD suffer from comparable low retention rates of ~5 % within the first 2 h after injection. While we most certainly agree with Kolossov's hypothesis that FB exert their supportive effect in **Phase II** and **Phase III**, our data suggest that it is highly unlikely that cell loss due to mechanical washout will be attenuated by co-transplantation. The fact that FB do not show clearly privileged retention rates as compared to SCD further emphasizes this point. Rather, we propose that additional strategies addressing the initial mechanical washout in **Phase I** could considerably improve the engraftment of co-transplanted FB and SCD, paving the way for improved synergistic effects of either cell type in later phases. This approach should be integrated into future studies to optimize the efficacy of cardiac stem cell therapies.

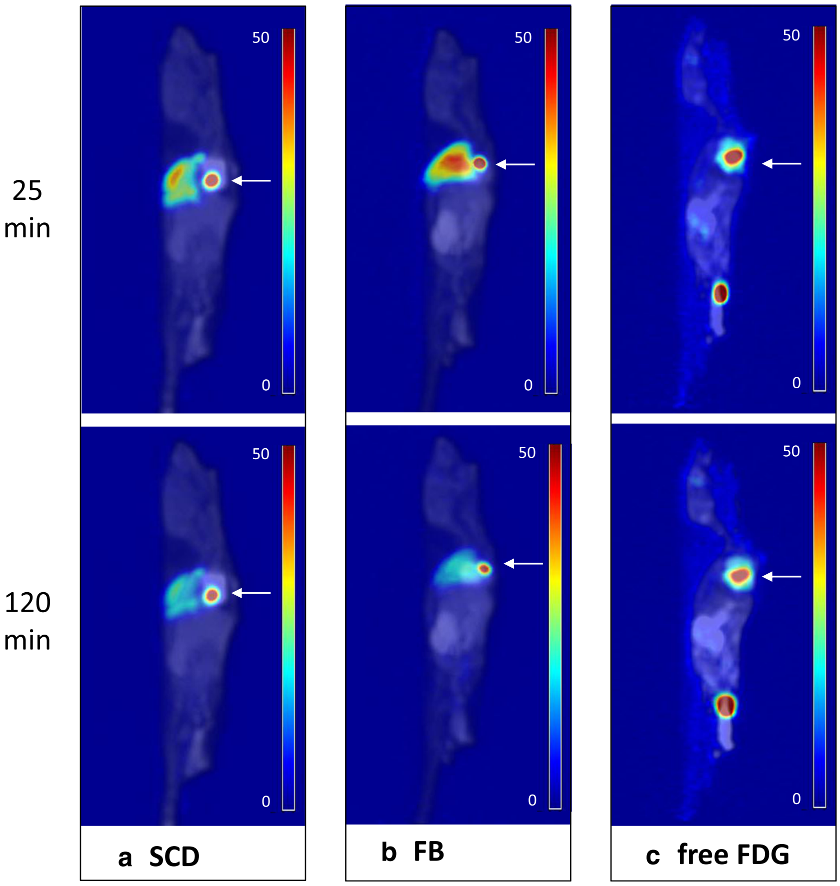

Fig. 4 Whole-body fusion images of the landmarking scans (*grey*) and dynamic scans (colored) of the delivered cells and free FDG at 25 min and 120 min after myocardial injection. Transplanted cells can easily be identified as bright spots, as indicated by arrows. **a** SCD and **b** FB were mainly located in the lungs as early as 25 min after application (*upper panels*). **c** Transplanted free FDG can be identified in the heart. Yet, the highest accumulation is located in the bladder due to excretion into the urinary tract. While loss of activity can be observed at 120 min post injection (lower panels), its local distribution is retained. The scale bar indicates percentage of maximum activity in the respective image

To our knowledge, approaches in animal models comparing different cell types during the initial phase have used post-mortem techniques [30]. We therefore aimed at establishing an in-vivo cell tracking method that is sensitive enough to compare the retention rates of different cell types.

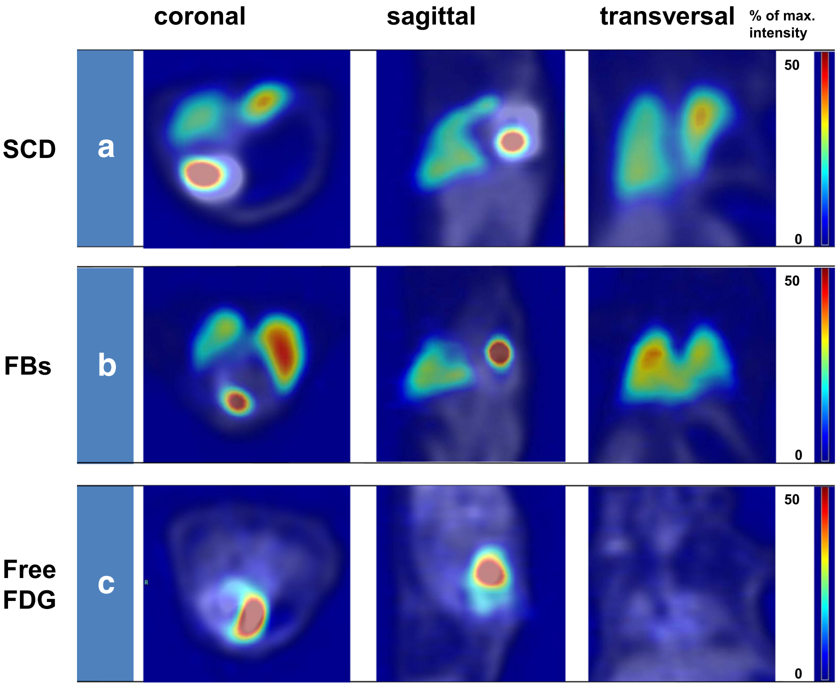

Fig. 5 Thoracic fusion images of landmarking scans (*grey*) and dynamic scans (colored) of the delivered cells at 25 min after myocardial injection. Whereas the majority of transplanted **a** SCD and **b** FB is located in the lungs, no significant accumulation of activity in the latter is observed after intramyocardial injection of c free FDG. The scale bar indicates the percentage of maximum activity in the respective image

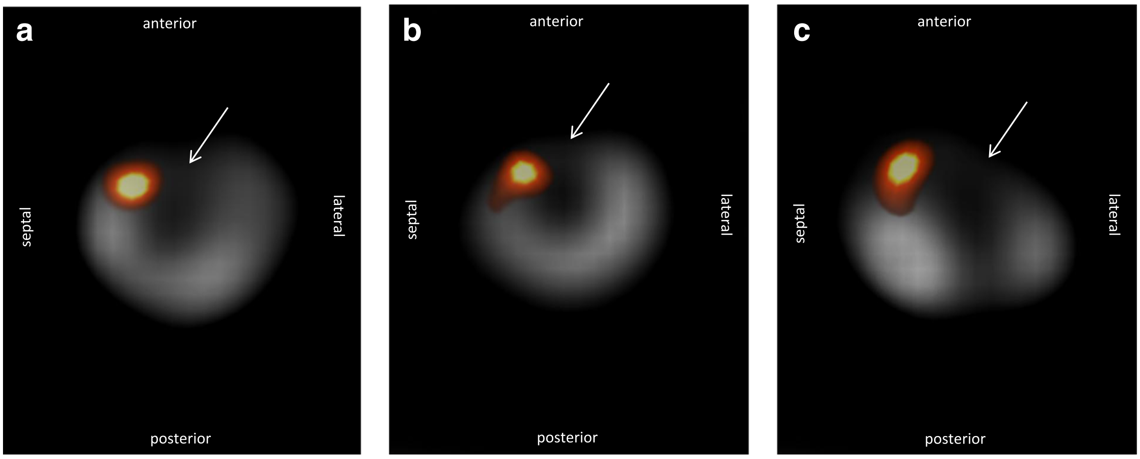

Fig. 6 Location of transplanted cells within the myocardium. Representative coronal slices of the fusion images of transplanted **a** SCD, **b** FB, and **c** free FDG, and the landmarking scan. FDG is absent in the areas of MI (*arrows*). The injected activity (*yellow spot*) is located in the border zone of the MI

Role of fibroblasts in cardiac repair

Studies comparing the therapeutic potential of different cell types have used fibroblasts mainly as controls representing non-contractile cells [31, 9, 32, 33]. However, the paper by Kolossov et al. cited above found that the typically low engraftment rates of ES-cell derived cardiomyocytes can be significantly increased by co-transplanting fibroblasts [7]. This is in agreement with the fact that fibroblasts constitute 26 % of the cell population within murine hearts, and thus represent the second-largest cell fraction after myocytes (54 %) [34]. Furthermore, fibroblasts have been reported to play an important role during embryonic development of the heart [35]. Therefore, while they have been formerly considered to be passive bystanders causing organ fibrosis, their presumptive role has changed to that of an important player in both healthy and diseased adult hearts [35]. In this regard, cardiac FB play a crucial role in force propagation, cardiac vessel homeostasis, and electrical signal conduction [11, 10]. These properties make them attractive both as direct targets for pharmaceuticals to reduce ventricular remodeling [10], and as components of cell-based therapies [36].

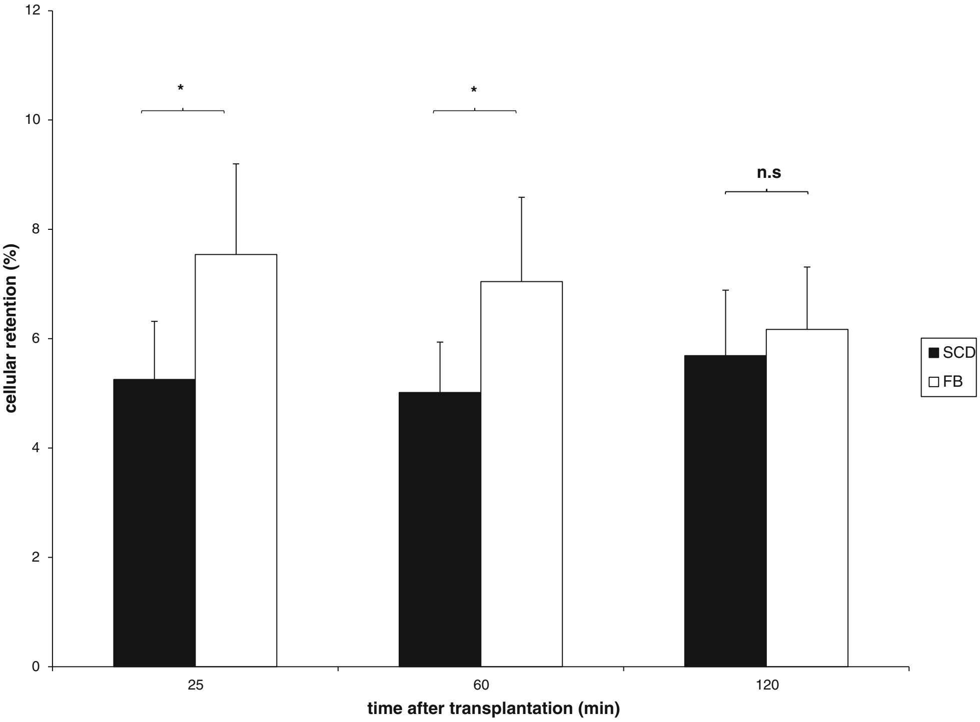

Fig. 7 Retention of transplanted cells at the site of the intramyocardial injection. Until 60 min after cell transplantation, FB were significantly better retained at the injection site than SCD (P=0.02 at 25 min, P=0.02 at 60 min), whereas retention rates did not differ any longer at 120 min p-st injection. This indicates cell-specific differences regarding cell loss during the first hour after injection. A fraction of~5 % unaffected by this massive initial washout remained at the site of injection independently of the applied cell type during the second hour (120 min, SCD vs. FB P=0.64). Retention rates of SCD did not differ significantly between the respective time points (P>0.05)

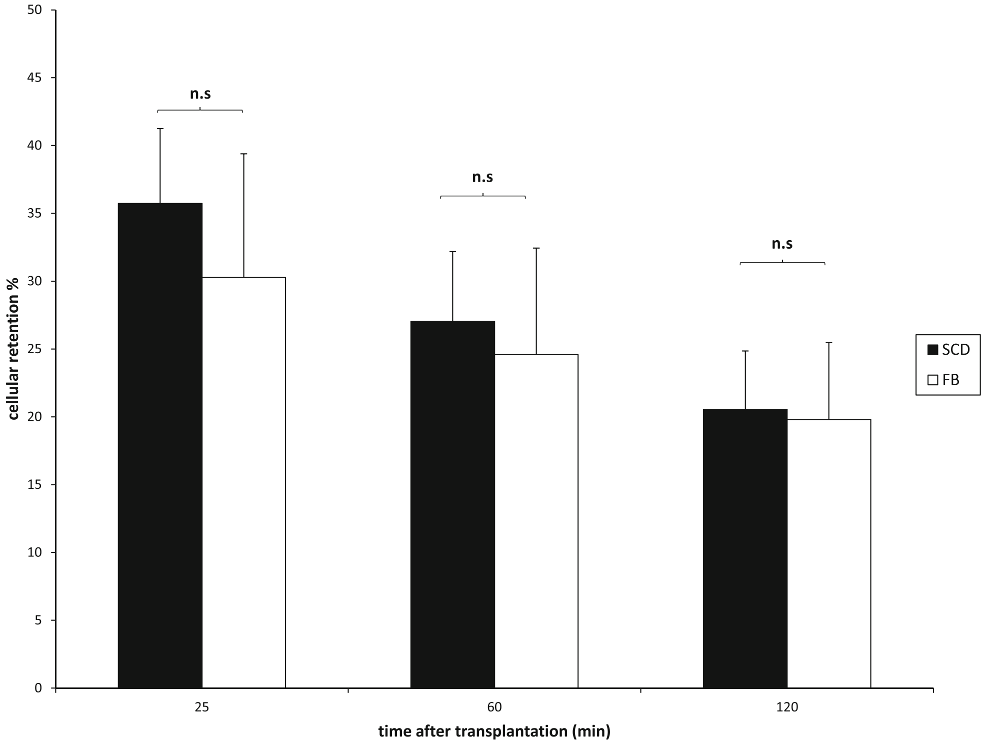

Fig. 8 Lung retention of transplanted cells. The majority of both cell types is located in the lungs. No significant differences are observed between lung retention rates of either SCD or FB at the respective time points ($p>0.05$). The data are presented as the mean±SD

Considering that massive initial cell loss occurs independently of the applied cell type, our data against the background of previous findings by others [10, 13, 14] indicate that FB can exert supportive effects on co-transplanted SCD during a later phase when long-term engraftment takes place. Further investigation is urgently needed to elucidate the role of fibroblasts in cardiac regeneration and their potential use in cardiomyoplasty.

Majority of transplanted cells located in lungs—low engraftment in the heart

We have recently reported very low initial retention rates of transplanted ESC derivatives at the injection site [16]. Retention kinetics between the two cell types only differ significantly during the first hour after transplantation. This could be due to different morphologies and surface protein patterns of

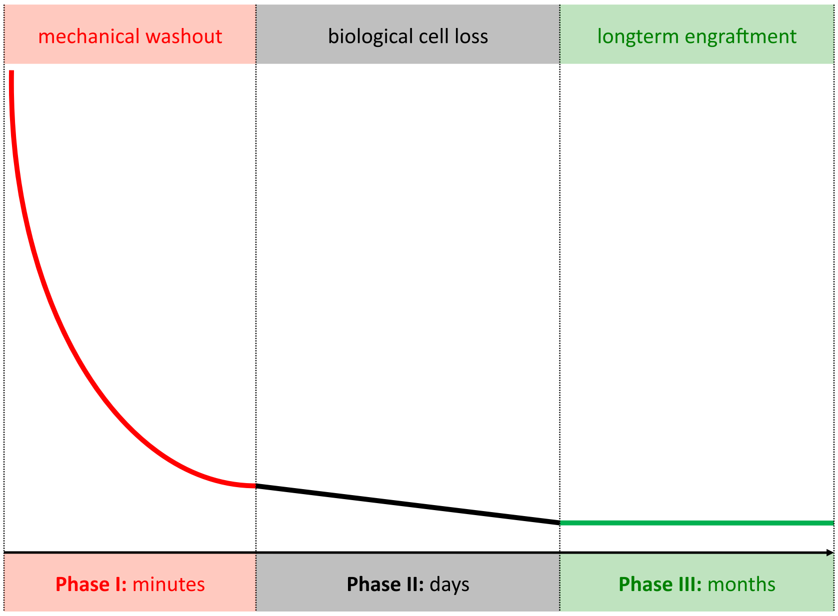

Fig. 9 Fate and survival of an intracardial cell transplant. The fate of transplanted cells can be divided into three phases. In **Phase I** about 90 % of the injected cells are mechanically washed out by the contracting myocardium within the first 25 min after application [16]. Further cell loss in **Phase II** is ascribed to the life-threatening biological milieu in the post-MI tissue [23]. Only 1–2 % of the transplanted cells survive these burdens [30, 24] and finally reach **Phase III** of long-term engraftment

the cell populations used. Yet, FB and SCD are retained at similar rates after 2 h, thus indicating that the underlying mechanism is independent of the cell type. We consider the mechanical extrusion of transplanted cells to be the major reason for the massive initial cell loss [14]. Others have attributed a further decrease of retained cells to reperfusion following myocardial ischemia [14, 37]. Regarding that cell residence time plays an important role in influencing myocardial repair [28], we assume that sustained occlusion infarcts would benefit most from cardiac stem cell therapies.

While the pulmonary trapping of both intramyocardial and intracoronary cell transplants regularly occurred in small-animal studies [13, 14], clinical studies applying bone marrow-derived stem cells did not report a pronounced detection of cells in the lungs [24, 38], or any corresponding adverse events such as pulmonary embolisms [4]. Cells were in fact localized to a great extent in the spleen and liver [39, 38]. Even if cellular entrapment were to occur in clinical applications, this could be overcome by the administration of a vasodilator targeting pulmonary vessels [40].

Therefore, we do not consider pulmonary entrapment to be an adverse event, but rather an indirect indicator for acute mechanical cell loss in **Phase I** (Fig. 9) in small-animal models. As described above in detail, massive initial washout is the predominant factor causing high cell loss after transplantation. Considering that the number and physical presence of transplanted cells is mandatory for the therapeutic effect [27, 28], we believe that studies targeting the highly sensitive quantification of the initial cell retention are of the highest relevance. Using our approach will allow future studies to assess the impact of genetic and morphological differences of various cell types on initial retention.

The role of tracer efflux in direct cell labeling and biodistribution of free FDG

Cell labeling procedures were identical, but intracellular retention of the radiotracer differed significantly between SCD and FB. Twenty-five minutes after labeling, SCD had released only 9 % of the initially cell-bound FDG, whereas the respective release rate for FB was 65 %. The cell- and tissue-specific stability of radiolabeling has been observed by various groups [41–43]. FDG is pharmacologically trapped by phosphorylation—catalyzed by the almost ubiquitously expressed enzyme hexokinase [43]. Only dephosphorylated FDG can be released from the cell. Caraco at al. were the first to correlate the release of FDG to the expression levels of glucose-6-phosphatase [44]. Although the cells' inherent property to release FDG was described decades ago [43], it has not been included in cell tracking approaches using FDG labeling [24, 13]. In contrast, others have concluded from this tracer efflux that FDG labeling is not suitable for tracking cell migration [45, 46]. Yet, as FDG has unique features, making it an ideal tracer for quantitative cell tracking during the initial phase, we recently introduced a method to integrate the time-dependent release of FDG into the analysis of PET data [16]. FDG uptake is highly dependent on the glucose concentration in the surrounding milieu, since FDG is a glucose analogue and competes with glucose for the transporter. Thus, low glucose concentrations are leading to significantly higher FDG uptake [45]. Therefore, different methods for efflux correction were applied for cellular quantification at the injection site and in the lungs with respect to cell-specific FDG retention rates. The highest activity concentration was measured at the injection site in a VOI of 20 μl. As a consequence, we did not consider the background activity caused by the released radiolabel to deteriorate quantitative PET data. Yet, we performed a correction for FDG-efflux as described previously [16]. In contrast, the size of the VOIs used for assessing cellular entrapment in the lungs was 2,000 μl. Therefore, background activity represents a considerable source of irritation (Fig. 2) and was included in PET data analysis of the lungs.

The main proportion of the injected FDG accumulated in the bladder (Fig. 2 and 4) due to renal excretion into the urinary tract, as described in seminal studies by Gallagher and colleagues assessing the biodistribution of FDG [43]. Brain uptake was relatively low, presumably due to anesthesia with isoflurane [47]. Surprisingly, we detected 7 % of the injected dose in the area of the lungs (Fig. 2). Lower retention rates were detected by Gallagher et al., which can be explained by the fact that the lungs were excised for consecutive measurement of radioactivity, thus excluding radioactivity from large vessels in the thorax [43].

Conclusion

Using high-resolution PET imaging, we have provided the first comparison of different transplanted cell types with respect to their acute retention in the mouse model of myocardial infarction. We achieved unprecedented accuracy by using a cell- and organ-specific approach correcting PET data for cellular FDG efflux.

Thereby, we observed a massive initial cell loss of ~95 % that leads to low rates of long-term engraftment for both SCD and FB. Our findings show that FB are not privileged compared to SCD regarding their acute retention kinetics. We conclude that the supportive effects of FB could be massively increased by strategies that reduce mechanical washout and thus improve the efficacy of cardiac stem cell therapies.

Acknowledgments We thank Christiane Groß, Barbara Markieton, and Judith Arcifa for expert technical assistance. This work was supported by the FöFoLe Program of the LMU Munich [C.L. and W.M.F.], the BMBF [01GN0960 to R.D. and W.M.F.], and the Deutsche

Forschungsgemeinschaft [DA 1296/2-1 to R.D. and FR 705/14-2 to W.M.F.].

Conflict of interest statement The authors declare that they have no conflicts of interest.

References

1. Bernhardt AM, Rahmel A, Reichenspurner H. The unsolved problem of organ allocation in times of organ shortage: the German solution? J Heart Lung Transplant: Off Publ Int Soc Heart Transplant. 2013;32(11):1049–51. doi:10.1016/j.healun.2013.08.012.
2. Laflamme MA, Murry CE. Regenerating the heart. Nat Biotechnol. 2005;23(7):845–56. doi:10.1038/nbt1117.
3. Donndorf P, Kundt G, Kaminski A, Yerebakan C, Liebold A, Steinhoff G, et al. Intramyocardial bone marrow stem cell transplantation during coronary artery bypass surgery: a meta-analysis. J Thorac Cardiovasc Surg. 2011;142(4):911–20. doi:10.1016/j.jtcvs.2010.12.013.
4. Zimmet H, Porapakkham P, Porapakkham P, Sata Y, Haas SJ, Itescu S, et al. Short- and long-term outcomes of intracoronary and endogenously mobilized bone marrow stem cells in the treatment of ST-segment elevation myocardial infarction: a meta-analysis of randomized control trials. Eur J Heart Fail. 2012;14(1):91–105. doi:10.1093/eurjhf/hfr148.
5. Hansson EM, Lendahl U. Regenerative medicine for the treatment of heart disease. J Intern Med. 2013;273(3):235–45. doi:10.1111/joim.12033.
6. Menasche P, Alfieri O, Janssens S, McKenna W, Reichenspurner H, Trinquart L, et al. The myoblast autologous grafting in ischemic cardiomyopathy (MAGIC) trial: first randomized placebo-controlled study of myoblast transplantation. Circulation. 2008;117(9):1189–200. doi:10.1161/CIRCULATIONAHA.107.734103.
7. Kolossov E, Bostani T, Roell W, Breitbach M, Pillekamp F, Nygren JM, et al. Engraftment of engineered ES cell-derived cardiomyocytes but not BM cells restores contractile function to the infarcted myocardium. J Exp Med. 2006;203(10):2315–27. doi:10.1084/jem.20061469.
8. Scorsin M, Hagege A, Vilquin JT, Fiszman M, Marotte F, Samuel JL, et al. Comparison of the effects of fetal cardiomyocyte and skeletal myoblast transplantation on postinfarction left ventricular function. J Thorac Cardiovasc Surg. 2000;119(6):1169–75.
9. van der Bogt KE, Sheikh AY, Schrepfer S, Hoyt G, Cao F, Ransohoff KJ, et al. Comparison of different adult stem cell types for treatment of myocardial ischemia. Circulation. 2008;118(14 Suppl):S121–9. doi:10.1161/CIRCULATIONAHA.107.759480.
10. Souders CA, Bowers SL, Baudino TA. Cardiac fibroblast: the renaissance cell. Circ Res. 2009;105(12):1164–76. doi:10.1161/CIRCRESAHA.109.209809.
11. Sussman MA, McCulloch A, Borg TK. Dance band on the Titanic: biomechanical signaling in cardiac hypertrophy. Circ Res. 2002;91(10):888–98.
12. Chang GY, Xie X, Wu JC. Overview of stem cells and imaging modalities for cardiovascular diseases. J Nucl Cardiol: Off Publ Am Soc Nucl Cardiol. 2006;13(4):554–69. doi:10.1016/j.nuclcard.2006.05.012.
13. Terrovitis J, Lautamaki R, Bonios M, Fox J, Engles JM, Yu J, et al. Noninvasive quantification and optimization of acute cell retention by in vivo positron emission tomography after intramyocardial cardiac-derived stem cell delivery. J Am Coll Cardiol. 2009;54(17):1619–26. doi:10.1016/j.jacc.2009.04.097.
14. Bonios M, Terrovitis J, Chang CY, Engles JM, Higuchi T, Lautamaki R, et al. Myocardial substrate and route of administration determine acute cardiac retention and lung bio-distribution of cardiosphere-derived cells. J Nucl Cardiol: Off Publ Am Soc Nucl Cardiol. 2011;18(3):443–50. doi:10.1007/s12350-011-9369-9.
15. Lautamaki R, Terrovitis J, Bonios M, Yu J, Tsui BM, Abraham MR, et al. Perfusion defect size predicts engraftment but not early retention of intra-myocardially injected cardiosphere-derived cells after acute myocardial infarction. Basic Res Cardiol. 2011;106(6):1379–86. doi:10.1007/s00395-011-0197-5.
16. Lang C, Lehner S, Todica A, Boening G, Franz WM, Bartenstein P, et al. Positron emission tomography based in-vivo imaging of early phase stem cell retention after intramyocardial delivery in the mouse model. Eur J Nucl Med Mol Imaging. 2013;40(11):1730–8. doi:10.1007/s00259-013-2480-1.
17. Muller M, Fleischmann BK, Selbert S, Ji GJ, Endl E, Middeler G, et al. Selection of ventricular-like cardiomyocytes from ES cells in vitro. FASEB J Off Publ Fed Am Soc Exp Biol. 2000;14(15):2540–8. doi:10.1096/fj.00-0002com.
18. David R, Brenner C, Stieber J, Schwarz F, Brunner S, Vollmer M, et al. MesP1 drives vertebrate cardiovascular differentiation through Dkk-1-mediated blockade of Wnt-signalling. Nat Cell Biol. 2008;10(3):338–45. doi:10.1038/ncb1696.
19. Smith RR, Barile L, Cho HC, Leppo MK, Hare JM, Messina E, et al. Regenerative potential of cardiosphere-derived cells expanded from percutaneous endomyocardial biopsy specimens. Circulation. 2007;115(7):896–908. doi:10.1161/CIRCULATIONAHA.106.655209.
20. Deindl E, Zaruba MM, Brunner S, Huber B, Mehl U, Assmann G, et al. G-CSF administration after myocardial infarction in mice attenuates late ischemic cardiomyopathy by enhanced arteriogenesis. FASEB J Off Publ Fed Am Soc Exp Biol. 2006;20(7):956–8. doi:10.1096/fj.05-4763fje.
21. van Laake LW, Passier R, Monshouwer-Kloots J, Nederhoff MG, Ward-van Oostwaard D, Field LJ, et al. Monitoring of cell therapy and assessment of cardiac function using magnetic resonance imaging in a mouse model of myocardial infarction. Nat Protoc. 2007;2(10):2551–67. doi:10.1038/nprot.2007.371.
22. Teng CJ, Luo J, Chiu RC, Shum-Tim D. Massive mechanical loss of microspheres with direct intramyocardial injection in the beating heart: implications for cellular cardiomyoplasty. J Thorac Cardiovasc Surg. 2006;132(3):628–32. doi:10.1016/j.jtcvs.2006.05.034.
23. Robey TE, Saiget MK, Reinecke H, Murry CE. Systems approaches to preventing transplanted cell death in cardiac repair. J Mol Cell Cardiol. 2008;45(4):567–81. doi:10.1016/j.yjmcc.2008.03.009.
24. Hofmann M, Wollert KC, Meyer GP, Menke A, Arseniev L, Hertenstein B, et al. Monitoring of bone marrow cell homing into the infarcted human myocardium. Circulation. 2005;111(17):2198–202. doi:10.1161/01.CIR.0000163546.27639.AA.
25. Reffelmann T, Konemann S, Kloner RA. Promise of blood- and bone marrow-derived stem cell transplantation for functional cardiac repair: putting it in perspective with existing therapy. J Am Coll Cardiol. 2009;53(4):305–8. doi:10.1016/j.jacc.2008.10.018.
26. Lovell MJ, Mathur A. Cardiac stem cell therapy: progress from the bench to bedside. Heart. 2010;96(19):1531–7. doi:10.1136/hrt.2009.192385.
27. Martin-Rendon E, Brunskill SJ, Hyde CJ, Stanworth SJ, Mathur A, Watt SM. Autologous bone marrow stem cells to treat acute myocardial infarction: a systematic review. Eur Heart J. 2008;29(15):1807–18. doi:10.1093/eurheartj/ehn220.
28. Ziebart T, Yoon CH, Trepels T, Wietelmann A, Braun T, Kiessling F, et al. Sustained persistence of transplanted proangiogenic cells contributes to neovascularization and cardiac function after ischemia. Circ Res. 2008;103(11):1327–34. doi:10.1161/CIRCRESAHA.108.180463.

29. Liang J, Huang W, Yu X, Ashraf A, Wary KK, Xu M, et al. Suicide gene reveals the myocardial neovascularization role of mesenchymal stem cells overexpressing CXCR4 (MSC (CXCR4)). PLoS One. 2012;7(9):e46158. doi:10.1371/journal.pone.0046158.
30. Muller-Ehmsen J, Krausgrill B, Burst V, Schenk K, Neisen UC, Fries JW, et al. Effective engraftment but poor mid-term persistence of mononuclear and mesenchymal bone marrow cells in acute and chronic rat myocardial infarction. J Mol Cell Cardiol. 2006;41(5):876–84. doi:10.1016/j.yjmcc.2006.07.023.
31. Sakai T, Li RK, Weisel RD, Mickle DA, Jia ZQ, Tomita S, et al. Fetal cell transplantation: a comparison of three cell types. J Thorac Cardiovasc Surg. 1999;118(4):715–24.
32. Hutcheson KA, Atkins BZ, Hueman MT, Hopkins MB, Glower DD, Taylor DA. Comparison of benefits on myocardial performance of cellular cardiomyoplasty with skeletal myoblasts and fibroblasts. Cell Transplant. 2000;9(3):359–68.
33. Roell W, Lu ZJ, Bloch W, Siedner S, Tiemann K, Xia Y, et al. Cellular cardiomyoplasty improves survival after myocardial injury. Circulation. 2002;105(20):2435–41.
34. Banerjee I, Fuseler JW, Price RL, Borg TK, Baudino TA. Determination of cell types and numbers during cardiac development in the neonatal and adult rat and mouse. Am J Physiol Heart Circ Physiol. 2007;293(3):H1883–91. doi:10.1152/ajpheart.00514.2007.
35. Kakkar R, Lee RT. Intramyocardial fibroblast myocyte communication. Circ Res. 2010;106(1):47–57. doi:10.1161/CIRCRESAHA.109.207456.
36. Kobayashi H, Shimizu T, Yamato M, Tono K, Masuda H, Asahara T, et al. Fibroblast sheets co-cultured with endothelial progenitor cells improve cardiac function of infarcted hearts. J Artif Organs: Off J Jpn Soc Artif Organs. 2008;11(3):141–7. doi:10.1007/s10047-008-0421-8.
37. Mitchell AJ, Sabondjian E, Blackwood KJ, Sykes J, Deans L, Feng Q, et al. Comparison of the myocardial clearance of endothelial progenitor cells injected early versus late into reperfused or sustained occlusion myocardial infarction. Int J Cardiovasc Imaging. 2013;29(2):497–504. doi:10.1007/s10554-012-0086-5.
38. Kang WJ, Kang HJ, Kim HS, Chung JK, Lee MC, Lee DS. Tissue distribution of 18 F-FDG-labeled peripheral hematopoietic stem cells after intracoronary administration in patients with myocardial infarction. J Nucl Med: Off Publ Soc Nucl Med. 2006;47(8):1295–301.
39. Schots R, De Keulenaer G, Schoors D, Caveliers V, Dujardin M, Verheye S, et al. Evidence that intracoronary-injected CD133+ peripheral blood progenitor cells home to the myocardium in chronic postinfarction heart failure. Exp Hematol. 2007;35(12):1884–90. doi:10.1016/j.exphem.2007.07.012.
40. Gao J, Dennis JE, Muzic RF, Lundberg M, Caplan AI. The dynamic in vivo distribution of bone marrow-derived mesenchymal stem cells after infusion. Cells Tissues Organs. 2001;169(1):12–20.
41. Adonai N, Nguyen KN, Walsh J, Iyer M, Toyokuni T, Phelps ME, et al. Ex vivo cell labeling with 64Cu-pyruvaldehyde-bis (N4-methylthiosemicarbazone) for imaging cell trafficking in mice with positron-emission tomography. Proc Natl Acad Sci U S A. 2002;99(5):3030–5. doi:10.1073/pnas.052709599.
42. Botti C, Negri DR, Seregni E, Ramakrishna V, Arienti F, Maffioli L, et al. Comparison of three different methods for radiolabelling human activated T lymphocytes. Eur J Nucl Med. 1997;24(5):497–504.
43. Gallagher BM, Fowler JS, Gutterson NI, MacGregor RR, Wan CN, Wolf AP. Metabolic trapping as a principle of oradiopharmaceutical design: some factors responsible for the biodistribution of [18 F] 2-deoxy-2-fluoro-D-glucose. J Nucl Med: Off Publ, Soc Nucl Med. 1978;19(10):1154–61.
44. Caraco C, Aloj L, Chen LY, Chou JY, Eckelman WC. Cellular release of [F-18]2-fluoro-2-deoxyglucose as a function of the glucose-6-phosphatase enzyme system. J Biol Chem. 2000;275(24):18489–94. doi:10.1074/jbc.M908096199.
45. Stojanov K, de Vries EF, Hoekstra D, van Waarde A, Dierckx RA, Zuhorn IS. [18 F] FDG labeling of neural stem cells for in vivo cell tracking with positron emission tomography: inhibition of tracer release by phloretin. Mol Imaging. 2012;11(1):1–12.
46. Prince HM, Wall DM, Ritchie D, Honemann D, Harrrison S, Quach H, et al. In vivo tracking of dendritic cells in patients with multiple myeloma. J Immunother. 2008;31(2):166–79. doi:10.1097/CJI.0b013e31815c5153.
47. Wolfs E, Struys T, Notelaers T, Roberts SJ, Sohni A, Bormans G, et al. 18 F-FDG labeling of mesenchymal stem cells and multipotent adult progenitor cells for PET imaging: effects on ultrastructure and differentiation capacity. J Nucl Med: Off Publ, Soc Nucl Med. 2013;54(3):447–54. doi:10.2967/jnumed.112.108316.

International Journal of
Molecular Sciences

Article

^{18}F-FDG PET-Based Imaging of Myocardial Inflammation Following Acute Myocardial Infarction in a Mouse Model

Praveen Vasudevan [1,2], Ralf Gäbel [1,2], Jan Stenzel [3], Joanna Förster [3], Jens Kurth [4], Brigitte Vollmar [5], Bernd Joachim Krause [4], Hüseyin Ince [6], Robert David [1,2,]* and Cajetan Immanuel Lang [6]

1 Department of Cardiac Surgery, Rostock University Medical Center, 18057 Rostock, Germany; Praveen.Vasudevan@med.uni-rostock.de (P.V.); Ralf.Gaebel@med.uni-rostock.de (R.G.)
2 Department of Life, Light and Matter, Rostock, University of Rostock, 18057 Rostock, Germany
3 Core Facility Multimodal Small Animal Imaging, University Medical Center, 18057 Rostock, Germany; jan2.stenzel@gmail.com (J.S.); Joanna.Foerster@med.uni-rostock.de (J.F.)
4 Department of Nuclear Medicine, Rostock University Medical Center, 18057 Rostock, Germany; Jens.Kurth@med.uni-rostock.de (J.K.); Bernd.Krause@med.uni-rostock.de (B.J.K.)
5 Rudolf-Zenker-Institute for Experimental Surgery, Rostock University Medical Center, 18057 Rostock, Germany; Brigitte.Vollmar@med.uni-rostock.de
6 Department of Cardiology, Rostock University Medical Center, 18057 Rostock, Germany; Hueseyin.Ince@med.uni-rostock.de (H.I.); Cajetan.Lang@med.uni-rostock.de (C.I.L.)
* Correspondence: Robert.David@med.uni-rostock.de

Received: 9 April 2020; Accepted: 6 May 2020; Published: 8 May 2020

Abstract: Cellular inflammation is an integral part of the healing process following acute myocardial infarction and has been under intense investigation for both therapeutic and prognostic approaches. Monocytes and macrophages are metabolically highly active and show increased uptake rates of glucose and its analog, ^{18}F-FDG. Yet, the specific allocation of the radioactivity to the inflammatory cells via positron emission tomography (PET) imaging requires the suppression of glucose metabolism in viable myocardium. In mice, the most important model organism in basic research, this can be achieved by the application of ketamine/xylazine (KX) for anesthesia instead of isoflurane. Yet, while the consensus exists that glucose metabolism is effectively suppressed, a strategy for reproducible image analysis is grossly lacking and causes uncertainty concerning data interpretation. We introduce a simple strategy for systematic image analysis, which is a prerequisite to evaluate therapies targeting myocardial inflammation. Mice underwent permanent occlusion of the left anterior descending artery (LAD), inducing an acute myocardial infarction (MI). Five days after MI induction, 10MBq ^{18}F-FDG was injected intravenously and a static PET/CT scan under ketamine/xylazine anesthesia was performed. For image reconstruction, we used an algorithm based on three-dimensional ordered subsets expectation maximization (3D-OSEM) followed by three-dimensional ordinary Poisson maximum a priori (MAP) reconstruction. Using this approach, high focal tracer uptake was typically located in the border zone of the infarct by visual inspection. To precisely demarcate the border zone for reproducible volume of interest (VOI) positioning, our protocol relies on positioning VOIs around the whole left ventricle, the inferobasal wall and the anterolateral wall guided by anatomical landmarks. This strategy enables comparable data in mouse studies, which is an important prerequisite for using a PET-based assessment of myocardial inflammation as a prognostic tool in therapeutic applications.

Keywords: FDG-PET; imaging inflammation; acute myocardial infarction; mouse model; image analysis

1. Introduction

According to the World Health Organization, coronary artery disease (CAD) is the world's biggest killer, accounting for almost 10 million deaths per year worldwide. CAD is defined by atherosclerosis of the coronary arteries leading to a reduction of the blood flow to the myocardium [1]. Plaques involved in this atherosclerotic process may rupture and form a blood clot, which in turn occludes the respective coronary artery and causes an acute myocardial infarction (AMI). Modern interventional and surgical approaches have drastically reduced the mortality of AMI. Yet, the irreversible loss of working cardiomyocytes eventually results in congestive heart failure over time in many patients [2].

Therefore, strategies to minimize the loss of viable myocardium and to support the healing process following ischemic damage of the heart have been under intense investigation during the last decades. Early trials performed since the 1970s have aimed to reduce myocardial damage following AMI by administrating unspecific inhibitors of inflammation such as corticosteroids, ibuprofen and indomethacin [3]. None of these concepts aiming at the unspecific reduction of myocardial inflammation have proven successful in clinical trials [4]. Despite negative results in early studies, these studies paved the way for more specific approaches targeting at distinct leucocyte subpopulations.

Recent evidence reveals that it is rather the amplitude and duration of inflammation and the timely and spatial resolution within the heart, which defines the quality of the scar following MI and the amount of tissue loss [5] than the mere extent of inflammation. Inflammation is an integral part of the complex process of myocardial healing and predominantly orchestrated by distinct monocyte subpopulations. A simplified concept distinguishes two functional subpopulations based on their immunophenotype, namely the extent of "Ly-6C" expression. Ly-6C^{high} monocytes dominate the inflammatory phase, whereas Ly-6C^{low} plays a central role in the proliferative phase by stimulating fibroblasts, angiogenesis and collagen formation [6].

For this reason, the concept of the unspecific suppression of inflammation has changed to a targeted modulation of cellular inflammation for both therapeutic and prognostic approaches [5]. Therapeutic modulations of these monocyte subpopulations can be assessed in post-mortem experiments by flow cytometry in animal models. In contrast, clinical translation of these concepts requires non-invasive experimental setups.

^{18}F-FDG PET is well established for imaging inflammation in patients and animals due to high levels of glucose transporters and thus increased ^{18}F-FDG uptake of activated inflammatory cells [7]. Clear allocation of focal ^{18}F-FDG accumulation requires low rates of baseline glucose in the tissue of interest, which hampers straightforward application of this method to the metabolically highly active heart. This issue has been solved by the introduction of specific protocols for suppressing glucose uptake in cardiomyocytes in both patients and mice [5,8–10]. The latter play an important role in this field of research, as the mouse is a key small animal model in basic research and enables the correlation of molecular biology and in-vivo imaging approaches. The use of ketamine/xylazine (KX) for anesthesia has been shown to suppress myocardial ^{18}F-FDG uptake effectively [5,9,10]. In our own previous work, a reduction of almost 90% could be achieved in healthy mice [11]. This concept is based on the observation that KX for anesthesia reduces serum insulin levels in rodents and thus prevents translocation of glucose transporter (GLUT) 4 to membranes of cardiomyocytes [12]. In contrast, glucose influx in activated leucocytes depends rather on GLUT 1 and GLUT3. Both transporters are expressed and translocated independently of insulin [13]. This concept has been substantiated by Lee et al. who could attribute ^{18}F-FDG uptake to inflammatory CD11b^{+} myeloid cells in a mouse model of myocardial infarction [5]. Yet, the use of this approach for the assessment and quantification of cellular inflammation in the context of therapy monitoring is currently hampered by the lack of strategies for image analysis. In this protocol we describe an approach for measuring of the focal tracer uptake based on positioning volumes of interest (VOI) around the whole left ventricle, the inferobasal and the anterolateral wall. This strategy will help researchers to generate comparable data when using ^{18}F-FDG PET for imaging cellular inflammation and its modulation post-acute myocardial infarction.

2. Results

The ketamine/xylazine protocol for anesthetizing healthy mice suppresses glucose metabolism of viable cardiomyocytes in healthy mice significantly compared to isoflurane (Figures 1 and 2). When setting the ranges of the color bars to identical minimum and maximum values, the effect can be clearly visualized.

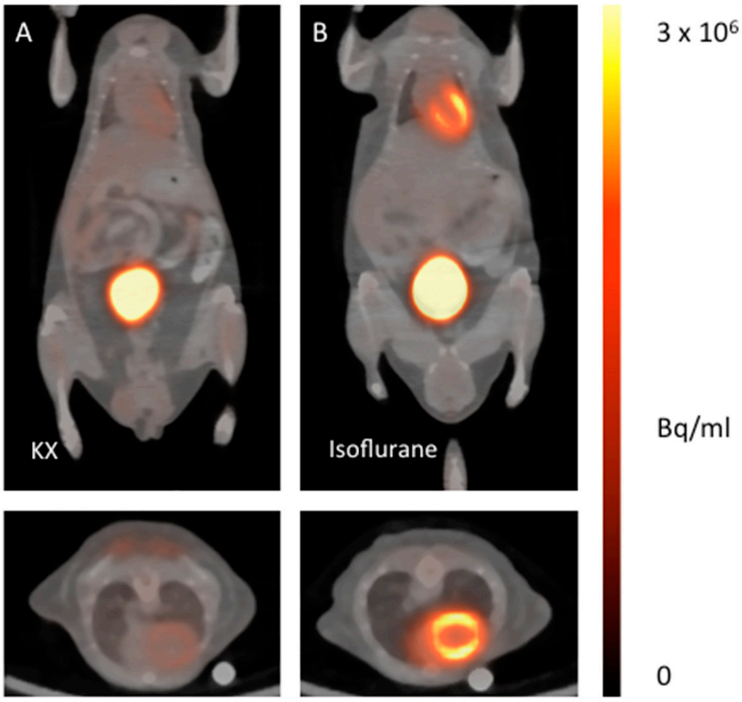

Figure 1. ^{18}F-FDG PET/CT fusion images of healthy mice anesthetized with ketamine/xylazine (**A**) in comparison with isoflurane (**B**). The upper images show representative coronal planes, the lower images the corresponding axial plane.

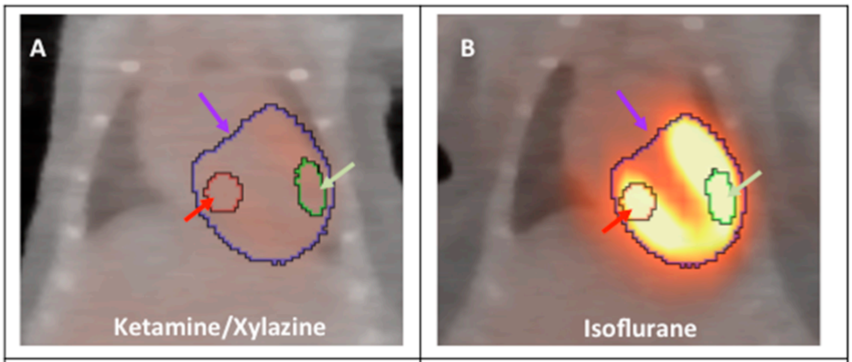

	%ID/g	%ID/g
Whole LV	5,3 ± 2,8	21,9 ± 6,9
Remote	5,5 ± 3,0	24,6 ± 7,8
Infarct	5,0 ± 2,5	21,5 ± 8,6

Figure 2. ^{18}F-FDG PET/CT fusion images of healthy mice anesthetized with ketamine/xylazine (**A**) and isoflurane (**B**); $n = 2$ per group. Representative standard VOIs are placed in whole LV (purple arrow), remote (red arrow) and infarct region (green arrow).

This protocol can be used to visualize and quantify infiltrating monocytes in the process of healing following acute myocardial infarction. When glucose metabolism is suppressed, the highest focal tracer accumulation can be detected within the border zone of the infarct (Figure 3A). In contrast, when mice are anesthetized with isoflurane, ^{18}F-FDG accumulates predominantly within the viable myocardium (Figure 3B).

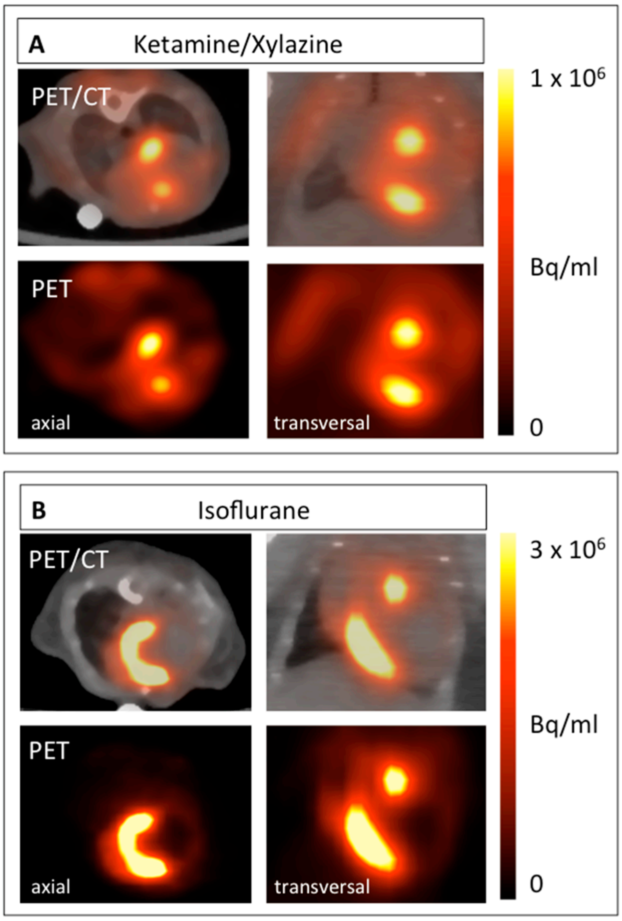

Figure 3. ^{18}F-FDG PET images of mice 5 days after MI induction anesthetized with ketamine/xylazine (**A**) in comparison with isoflurane (**B**). Both axial (left) and coronal planes (right) are shown. The respective PET image is shown under each PET/CT fusion image.

As the exact extent of the border zone cannot be determined the pattern of ^{18}F-FDG accumulation can only be described qualitatively from the mere PET/CT images (Figure 3). Therefore, we developed a protocol to quantify this change in the ^{18}F-FDG upake pattern relying on an indirect approach. To this end, VOIs were positioned around the entire left ventricle (LV), the inferobasal wall and the anterolateral wall. These regions can be localized relatively easily from the PET/CT images as shown in Figure 4. As defining these VOIs in infarcted animals is difficult, a healthy animal anesthetized with isoflurane was used for VOI definition. By importing these VOIs from healthy animals for image analysis, the respective regions of the LV in infarcted animals could be easily reproduced (Figure 5).

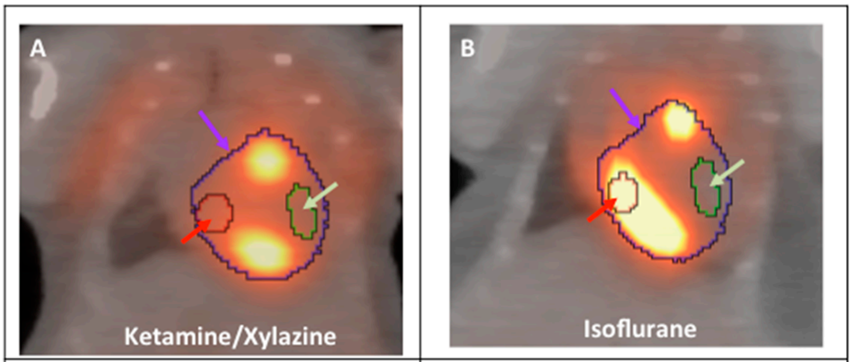

	%ID/g	%ID/g
Whole LV	6,7 ± 1,8	48,9 ± 10,6 *
Remote	4,4 ± 0,3	12,6 ± 6,5 *
Infarct	5,1 ± 1,6	69,4 ± 18,4 *

Figure 4. Representative examples of the analysis strategy underlying the protocol for both mice anesthetized with isoflurane (**A**) and ketamine/xylazine (**B**) 5 days after MI induction (n = 4 per group). The "entire left ventricle" VOI reflects the global FDG uptake of the LV (purple arrow). The "remote" VOI was positioned in the inferobasal wall and reflects viable myocardium (red arrow). The "infarct" VOI reflects infarct tissue and contains almost no cardiomyocytes (green arrow). *: $p < 0.05$ compared to animals anesthetized with ketamine/xylazine. Values are presented as mean ± SD. Values are presented as mean ± SD. p-values were calculated using the student t-test.

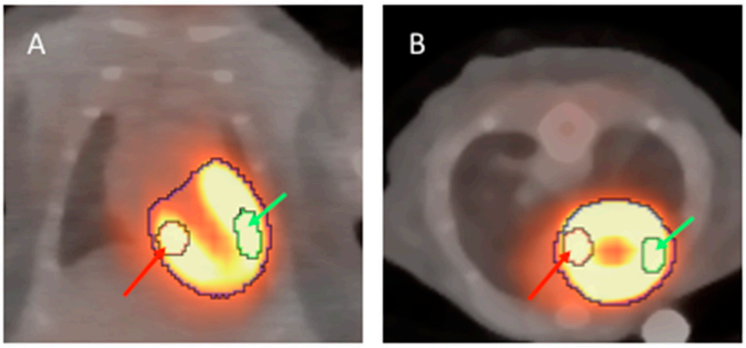

Figure 5. ^{18}F-FDG PET/CT fusion images of a healthy mouse anesthetized with isoflurane. The left ventricle can be clearly identified in both coronal (**A**) and axial (**B**) planes. VOIs of 5 µL are placed in the inferobasal wall (red arrow) and the anterolateral wall (green arrow).

3. Discussion

Cellular inflammation is an integral part of the healing process after myocardial infarction and thus an attractive target for both therapeutic and diagnostic approaches. Non-invasive imaging tools are indispensible for translation of such approaches into clinical practice. Therefore, a protocol for the imaging of cellular inflammation in mice based on ^{18}F-FDG PET has been evaluated by us and others [5,9–11]. The mouse is of specific interest due to its relevance in basic research and the availability of imaging modalities, which can be used for both mice and men.

The prerequisite for specific imaging of inflammation is an effective protocol for suppression of myocardial glucose uptake, which could be achieved by the use of ketamine/xylazine (KX) for anesthesia in different mouse strains by several groups [5,9–11]. In contrast to the consensus on suppressing myocardial glucose uptake, strategies concerning the analysis of obtained images and data interpretation are less coherent. Furthermore, the time point chosen for image acquisition ranges from 3–7 days post MI between available studies [5,9,10]. Therefore, it is important to correlate the imaging data with the respective monocyte or macrophage population, which is dominating the healing process at the respective time point. Both ours and the data obtained by Nahrendorf´s group detected the highest focal ^{18}F-FDG accumulations in the border zone five days after MI [5,11]. This can be clearly seen in PET/CT images and correlates well with histological findings [5]. Yet, there is no reproducible VOI positioning strategy available for quantification of radioactivity in the border zone.

Hence, we introduced an indirect approach to describe the ^{18}F-FDG distribution pattern by positioning three VOIs into defined areas of the heart. The fist VOI encompasses the whole LV and reflects global glucose metabolism. Then, two representative VOIs of approximately 5 µL are placed into the infarct region (anterolateral wall) and the remote area (inferobasal wall). Both regions can be easily located by from anatomical landmarks in the PET/CT images from a healthy animal anasthetized with isoflurane. We believe that our approach provides a method that helps to obtain a comparable result in the imaging myocardial inflammation by ^{18}F-FDG PET/CT. Yet, further research on the glucose metabolism of the different monocyte subpopulations will be important in order to further improve the quality of molecular imaging in this field.

4. Limitations

Our strategy for image analysis and interpretation provides an indirect approach for the semi-quantitative assessment of myocardial inflammation. The border zone cannot be quantified by this approach, as it consists of an overlap of both remote and infarcted myocardia. Therefore, our strategy should be complemented by other imaging approaches for studying the border zone. The left and right ventricles as well as the atria cannot be distinguished reliably from CT images. Furthermore, the use of ketamine/xylazine effectively suppresses myocardial glucose uptake making the delineation of the left ventricle impossible in the respective scan. Yet, left ventricular volume can be perfectly assessed from ^{18}F-FDG PET scans under anesthesia with isoflurane, as described by Todica et al. [14]. Therefore, an additional scan to obtain an “LV VOI template” using isoflurane is necessary in our approach.

5. Materials and Methods

5.1. Animal Model

The experiments in this study were approved by the federal animal care committee of the *Landesamt für Landwirtschaft, Lebensmittelsicherheit und Fischerei Mecklenburg-Vorpommern* (local animal protection authority, Germany) (registration no. LALLF M-V/TSD/7221.3-1.1-054/15; approved by 16 February 2018). Mice of the strain 129S6/SvEvTac were bred in the animal facility of the Rostock University Medical Center. Animals used were 12–14 weeks old, had a body weight of about 20 g and had the same access to food and water. Acute myocardial infarction was induced by permanent occlusion of the LAD as described previously [11]. For establishing of the protocol described, at least one healthy animal and two animals with myocardial infarctions should be included. PET imaging was performed 5 days after MI induction.

5.2. PET Imaging

In order to obtain images showing the glucose metabolism of the myocardium of a healthy animal, animals with myocardial infarction were anesthetized by inhalation of isoflurane (4% for induction and 1–2.5% maintenance during preparation and scanning). The healthy control is used to define and align the VOIs. For imaging cellular inflammation, the respective mouse was anesthetized by i.p injection of ketamine/xylazine (ketamine 84 mg/kg and xylazine 11.2 mg/kg) 20 min before tracer application. The KX control is used to verify the suppression of glucose metabolism.

Images were acquired on a small animal PET/CT scanner (Inveon MM-PET/CT, Siemens Medical Solutions, Knoxville, TN, USA) according to a standard protocol: 10MBq ^{18}F-FDG was injected intravenously via a custom-made micro catheter placed in a tail vein. Mice were imaged after an uptake period of 60 min in a prone position for 20 min. Respiration of the mice was controlled and core body temperature was constantly kept at 38 °C via a heating pad during the imaging procedure. A Feldkamp algorithm was used to reconstruct CT images.

The 3-dimensional (3-D) iterative ordered-subset expectation maximization reconstruction algorithm (3D-OSEM/OP-MAP) with the following parameters was used for reconstruction of the PET images: 4 iterations (OSEM), 32 iterations (MAP), 1.7 mm target resolution and 128 × 128 matrix size. Reconstruction included corrections for random coincidences, dead time, attenuation, scatter, and decay.

5.3. PET Image Analysis

Image analysis was performed using an Inveon Research Workplace 4.2 (Siemens, Knoxville, TN, USA). PET and CT images were fused by the use of an automated volumetric fusion algorithm and then verified by an experienced reader for perfect alignment and adjusted when necessary. For qualitative analysis and a comparison of different groups, the activity concentration in the PET images were displayed as "Voxel Intensity" (Bq/mL). For a visual comparison of animals anesthetized with isoflurane and ketamine/xylazine, the scale bar was set from 0 to 3×10^6 Bq/mL (isoflurane) and 1×10^6 Bq/mL (KX) respectively.

The healthy animal anesthetized with isoflurane was used for defining the VOIs, which were used in the following analyses of infarcted animals. The whole left ventricle (LV) shows intense 18F-FDG uptake enabling easy VOI positioning (Figure 5). The VOIs were placed into the respective regions as described below, and then saved into a selected folder:

Global uptake in LV ("whole LV"): A spherical VOI was drawn around the LV and its size adjusted with the "edit" function, using the CT image for correct anatomical positioning. The VOI will typically have a volume of 200 μL.

Infarcted Myocardium: A spherical VOI of 5 μL (+/− 0.1μL) was positioned in the anterolateral wall, based on anatomical landmarks from CT and PET images.

Remote Myocardium: A spherical VOI of 5 μL (+/− 0.1μL) was positioned in the inferobasal wall, based on anatomical landmarks from CT and PET images.

For a semi-quantitative comparison of myocardial ^{18}F-FDG uptake of infarcted hearts, the VOIs which have been defined in the healthy animal before were imported. VOIs were adjusted and fine-tuned based on anatomical landmarks from the PET and CT images.

5.4. Statistics

The data are presented as mean values ± standard deviation (SD). Student's *t*-test was used to assess the statistical difference between the groups. Values of $p < 0.05$ were considered statistically significant.

Author Contributions: Conceptualization, C.I.L.; methodology, J.S., J.F. and J.K.; formal analysis, C.I.L. and P.V.; investigation, C.I.L., P.V., R.G.; writing—original draft preparation, P.V. and C.I.L.; writing—review and editing, J.K., R.D., H.I.; visualization, P.V. and C.I.L.; supervision, C.I.L. and R.D.; funding acquisition, C.I.L., R.D., B.J.K. and B.V. All authors have read and agree to the published version of the manuscript.

Funding: This work was supported by the Federal Ministry of Education and Research Germany (FKZ 0312138A and FKZ 316159), the State Mecklenburg-Western Pomerania with EU Structural Funds (ESF/IVWM-B34-0030/10 and ESF/IVBM-B35-0010/12) and the DFG (DA1296/6-1), the German Heart Foundation (F/01/12) and German Heart Research Foundation (F/34/15). In addition, RD is supported by the EU Structural Fund (ESF/14-BM-A55-0024/18), the FORUN Program of Rostock University Medical Centre (889066), the Josef and Käthe Klinz Foundation (T319/29737/2017), the DAMP Foundation and the BMBF (VIP+ 00240). The small animal PET/CT was funded by the Deutsche Forschungsgemeinschaft (INST 2268/6-1 FUGG). C.L. was supported by the Clinician Scientist Program of Rostock University Medical Center.

Conflicts of Interest: The authors declare no conflict of interest.

Abbreviations

FDG	fluorodeoxyglucose
PET	positron emission tomography
KX	ketamine/xylazine
CT	computer tomography
VOI	volume of interest
AMI	acute myocardial infarction
MI	myocardial infarction
%ID/g	% of injected dose per gram
SD	standard deviation
LV	left ventricle
GLUT	glucose transporter

References

1. Knuuti, J.; Wijns, W.; Saraste, A.; Capodanno, D.; Barbato, E.; Funck-Brentano, C.; Prescott, E.; Storey, R.F.; Deaton, C.; Cuisset, T.; et al. 2019 ESC Guidelines for the diagnosis and management of chronic coronary syndromes. *Eur. Heart J.* **2020**, *41*, 407–477. [CrossRef] [PubMed]
2. Fang, J.; Mensah, G.A.; Croft, J.B.; Keenan, N.L. Heart failure-related hospitalization in the U.S., 1979 to 2004. *J. Am. Coll. Cardiol.* **2008**, *52*, 428–434. [CrossRef] [PubMed]
3. Seropian, I.M.; Toldo, S.; Van Tassell, B.W.; Abbate, A. Anti-inflammatory strategies for ventricular remodeling following ST-segment elevation acute myocardial infarction. *J. Am. Coll. Cardiol.* **2014**, *63*, 1593–1603. [CrossRef] [PubMed]
4. Van Hout, G.P.; Jansen of Lorkeers, S.J.; Wever, K.E.; Sena, E.S.; Kouwenberg, L.H.; van Solinge, W.W.; Macleod, M.R.; Doevendans, P.A.; Pasterkamp, G.; Chamuleau, S.A.; et al. Translational failure of anti-inflammatory compounds for myocardial infarction: A meta-analysis of large animal models. *Cardiovasc. Res.* **2016**, *109*, 240–248. [CrossRef] [PubMed]
5. Lee, W.W.; Marinelli, B.; van der Laan, A.M.; Sena, B.F.; Gorbatov, R.; Leuschner, F.; Dutta, P.; Iwamoto, Y.; Ueno, T.; Begieneman, M.P.; et al. PET/MRI of inflammation in myocardial infarction. *J. Am. Coll. Cardiol.* **2012**, *59*, 153–163. [CrossRef] [PubMed]
6. Nahrendorf, M.; Swirski, F.K.; Aikawa, E.; Stangenberg, L.; Wurdinger, T.; Figueiredo, J.L.; Libby, P.; Weissleder, R.; Pittet, M.J. The healing myocardium sequentially mobilizes two monocyte subsets with divergent and complementary functions. *J. Exp. Med.* **2007**, *204*, 3037–3047. [CrossRef] [PubMed]
7. Love, C.; Tomas, M.B.; Tronco, G.G.; Palestro, C.J. FDG PET of infection and inflammation. *Radiographics* **2005**, *25*, 1357–1368. [CrossRef] [PubMed]
8. Rischpler, C.; Dirschinger, R.J.; Nekolla, S.G.; Kossmann, H.; Nicolosi, S.; Hanus, F.; van Marwick, S.; Kunze, K.P.; Meinicke, A.; Gotze, K.; et al. Prospective Evaluation of 18F-Fluorodeoxyglucose Uptake in Postischemic Myocardium by Simultaneous Positron Emission Tomography/Magnetic Resonance Imaging as a Prognostic Marker of Functional Outcome. *Circ. Cardiovasc. Imaging* **2016**, *9*, e004316. [CrossRef] [PubMed]
9. Thackeray, J.T.; Bankstahl, J.P.; Wang, Y.; Wollert, K.C.; Bengel, F.M. Clinically relevant strategies for lowering cardiomyocyte glucose uptake for 18F-FDG imaging of myocardial inflammation in mice. *Eur. J. Nucl. Med. Mol. Imaging* **2015**, *42*, 771–780. [CrossRef] [PubMed]
10. Thackeray, J.T.; Bankstahl, J.P.; Wang, Y.; Korf-Klingebiel, M.; Walte, A.; Wittneben, A.; Wollert, K.C.; Bengel, F.M. Targeting post-infarct inflammation by PET imaging: Comparison of (68)Ga-citrate and (68)Ga-DOTATATE with (18)F-FDG in a mouse model. *Eur. J. Nucl. Med. Mol. Imaging* **2015**, *42*, 317–327. [CrossRef] [PubMed]
11. Vasudevan, P.; Gaebel, R.; Doering, P.; Mueller, P.; Lemcke, H.; Stenzel, J.; Lindner, T.; Kurth, J.; Steinhoff, G.; Vollmar, B.; et al. 18F-FDG PET-Based Imaging of Myocardial Inflammation Predicts a Functional Outcome Following Transplantation of mESC-Derived Cardiac Induced Cells in a Mouse Model of Myocardial Infarction. *Cells* **2019**, *8*, 1613. [CrossRef] [PubMed]
12. Saha, J.K.; Xia, J.; Grondin, J.M.; Engle, S.K.; Jakubowski, J.A. Acute hyperglycemia induced by ketamine/xylazine anesthesia in rats: Mechanisms and implications for preclinical models. *Exp. Biol. Med. (Maywood)* **2005**, *230*, 777–784. [CrossRef] [PubMed]

13. Ahmed, N.; Kansara, M.; Berridge, M.V. Acute regulation of glucose transport in a monocyte-macrophage cell line: Glut-3 affinity for glucose is enhanced during the respiratory burst. *Biochem. J.* **1997**, *327 Pt 2*, 369–375. [CrossRef]
14. Todica, A.; Beetz, N.L.; Gunther, L.; Zacherl, M.J.; Grabmaier, U.; Huber, B.; Bartenstein, P.; Brunner, S.; Lehner, S. Monitoring of Cardiac Remodeling in a Mouse Model of Pressure-Overload Left Ventricular Hypertrophy with [(18)F]FDG MicroPET. *Mol. Imaging Biol.* **2018**, *20*, 268–274. [CrossRef] [PubMed]

cells

MDPI

Article

18F-FDG PET-Based Imaging of Myocardial Inflammation Predicts a Functional Outcome Following Transplantation of mESC-Derived Cardiac Induced Cells in a Mouse Model of Myocardial Infarction

Praveen Vasudevan [1,2], Ralf Gaebel [1,2], Piet Doering [3,4], Paula Mueller [1,2], Heiko Lemcke [1,2], Jan Stenzel [5], Tobias Lindner [5], Jens Kurth [3], Gustav Steinhoff [1,2], Brigitte Vollmar [5], Bernd Joachim Krause [3], Hueseyin Ince [6], Robert David [1,2] and Cajetan Immanuel Lang [6,*]

[1] Department of Cardiac Surgery, Rostock University Medical Center, 18057 Rostock, Germany; praveen.vasudevan@med.uni-rostock.de (P.V.); Ralf.Gaebel@med.uni-rostock.de (R.G.); Paula.Mueller@uni-rostock.de (P.M.); Heiko.Lemcke@med.uni-rostock.de (H.L.); Gustav.Steinhoff@med.uni-rostock.de (G.S.); Robert.David@med.uni-rostock.de (R.D.)

[2] Department of Life, Light and Matter, University of Rostock, 18059 Rostock, Germany

[3] Department of Nuclear Medicine, Rostock University Medical Center, 18057 Rostock, Germany; Piet.doering@uni-rostock.de (P.D.); Jens.Kurth@med.uni-rostock.de (J.K.); Bernd.Krause@med.uni-rostock.de (B.J.K.)

[4] Rudolf-Zenker-Institute for Experimental Surgery, Rostock University Medical Center, 18057 Rostock, Germany

[5] Core Facility Multimodal Small Animal Imaging, Rostock University Medical Center, 18057 Rostock, Germany; Jan.Stenzel@med.uni-rostock.de (J.S.); Tobias.Lindner@med.uni-rostock.de (T.L.); Brigitte.Vollmar@med.uni-rostock.de (B.V.)

[6] Department of Cardiology, Rostock University Medical Center, 18057 Rostock, Germany; Hueseyin.Ince@med.uni-rostock.de

[*] Correspondence: Cajetan.Lang@med.uni-rostock.de; Tel.: +49-381-494-61-05

Received: 21 October 2019; Accepted: 9 December 2019; Published: 11 December 2019

Abstract: Cellular inflammation following acute myocardial infarction has gained increasing importance as a target mechanism for therapeutic approaches. We sought to investigate the effect of syngeneic cardiac induced cells (CiC) on myocardial inflammation using 18F-FDG PET (Positron emission tomography)-based imaging and the resulting effect on cardiac pump function using cardiac magnetic resonance (CMR) imaging in a mouse model of myocardial infarction. Mice underwent permanent left anterior descending coronary artery (LAD) ligation inducing an acute inflammatory response. The therapy group received an intramyocardial injection of 10^6 CiC into the border zone of the infarction. Five days after myocardial infarction, 18F-FDG PET was performed under anaesthesia with ketamine and xylazine (KX) to image the inflammatory response in the heart. Flow cytometry of the mononuclear cells in the heart was performed to analyze the inflammatory response. The effect of CiC therapy on cardiac function was determined after three weeks by CMR. The 18F-FDG PET imaging of the heart five days after myocardial infarction (MI) revealed high focal tracer accumulation in the border zone of the infarcted myocardium, whereas no difference was observed in the tracer uptake between infarct and remote myocardium. The CiC transplantation induced a shift in 18F-FDG uptake pattern, leading to significantly higher 18F-FDG uptake in the whole heart, as well as the remote area of the heart. Correspondingly, high numbers of $CD11^+$ cells could be measured by flow cytometry in this region. The CiC transplantation significantly improved the left ventricular ejection function (LVEF) three weeks after myocardial infarction. The CiC transplantation after myocardial infarction leads to an improvement in pump function through modulation of the cellular inflammatory response five days after myocardial infarction. By combining CiC transplantation and the cardiac glucose uptake suppression protocol with KX in a mouse model, we show for the first time, that imaging of cellular inflammation after myocardial infarction using 18F-FDG PET can be used as an early prognostic tool for assessing the efficacy of cardiac stem cell therapies.

Keywords: inflammation; 18F-FDG PET; cardiomyocytes; cardiac induced cells; cardiac function; non-invasive imaging

---

1. Introduction

Inflammatory activity of the innate immune system following myocardial infarction substantially influences remodeling after myocardial infarction (MI) and the evolution of heart failure [1]. Therefore, anti-inflammatory therapies have been under intense investigation since the early 1970s. Yet, none of the clinical trials testing pharmacological strategies aiming at unspecific reduction of myocardial inflammation has proven successful [2]. The main reason for these disappointing findings is the complexity of the well-orchestrated activity of different leukocyte populations. The amplitude and duration of inflammation and the timely and spatial resolution within the heart define the quality of the scar following MI and the amount of tissue loss rather than the mere extent of inflammation [1]. Hence, the concept of suppressing inflammation has changed to a further elaborated concept of "modulating cellular inflammation". The balance of pro- and anti-inflammatory immune cells and their recruiting mechanisms are discussed as both therapeutic and prognostic targets [1]. Further understanding of this intricate cellular immune response to myocardial ischemia in a translational setting requires non-invasive molecular imaging tools. The 18F-FDG PET (Positron emission tomography) using specific protocols for suppressing glucose uptake in cardiomyocytes has recently been introduced to detect cellular inflammation following MI in both patients and C57BL/6 mice [1,3–5]

Protocols to suppress physiological myocardial 18F-FDG uptake require low-carbohydrate diet the day before imaging followed by a 12 h fasting period and intravenous application of heparin before the actual scan [3]. In mice, myocardial glucose metabolism can be effectively suppressed by replacing the commonly used anaesthetic isofluorane for a ketamine/xylazine-based protocol [1].

However, to our knowledge, no studies have used these protocols for measuring therapeutic effects of therapies aiming at improving myocardial healing following MI. Therefore, we implanted syngeneic cardiac induced cells committed to the cardiac lineage in order to improve post-MI cardiac function in 129Sv mice as measured my cardiac magnetic resonance (CMR). Cellular inflammation was detected by 18F-FDG PET in vivo and by post-mortem flow cytometry in both infarcted and remote myocardium.

We hypothesize that PET-based imaging and quantification of cellular inflammation can be used as a molecular imaging tool for both quantification and spatial distribution of monocytes and as an early prognostic tool to predict the effect of cardiac stem cell therapies modulating post-MI inflammation.

2. Materials and Methods

2.1. Stem Cell Culture and Cardiovascular Differentiation

W4 murine embryonic stem cells (mESCs), originally isolated from the 129S6 mouse strain [6], were grown according to standard protocols as described previously [7]. In brief, cells were cultured in DMEM supplemented with 15% FBS Superior (Biochrom AG, Berlin, Germany), 1% Cell Shield® (Minerva Biolabs GmbH, Berlin, Germany), 100 µM non-essential amino acids, 1000 U/mL leukemia inhibitory factor (Phoenix Europe GmbH, Mannheim, Germany) and 100 µM β-mercaptoethanol (Sigma-Aldrich GmbH, Steinheim, Germany) at 37 °C, 5% CO_2, and 20% O_2. For cardiovascular differentiation we used cardiogenic differentiation medium, containing IBM (Iscove's Basal Medium, Biochrom AG) supplemented with 10% FBS Superior, 1% Cell Shield®, 100 µM non-essential amino acids, 450 μm 1-thioglycerol (Sigma-Aldrich GmbH), and 213 μg/mL ascorbic acid (Sigma-Aldrich GmbH), as described previously [7,8]. Cardiovascular differentiation was initiated by hanging-drop culture for two days at 37 °C, 5% CO_2, and 20% O_2. 400 cells per drop were plated on the cover of a square petri dish and grown for 2 days to start formation of embryoid bodies (EB). Afterwards, EB were grown additional four days in suspension culture [9] and then harvested for transplantation and PCR analysis. These cells will be referred to as cardiac induced cells (CiC). They were cultured till day 30 for beating foci analysis.

2.2. Animal Model

The present study was approved by the federal animal care committee of the Landesamt für Landwirtschaft, Lebensmittelsicherheit und Fischerei Mecklenburg-Vorpommern (LALLF, Germany) (registration no. LALLF M-V/TSD/7221.3-1.1-054/15). The 129S6/SvEvTac were bred in the animal facility of the Rostock University Medical Center and maintained in specified pathogen-free conditions. The mice had access to water and standard laboratory chow ad libitum and received humane care according to the German legislation on protection of animals and the Guide for the Care and Use of Laboratory Animals (NIH publication 86–23, revised 1985), and all efforts were made to minimize suffering. Mice were anaesthetized with pentobarbital (50 mg/kg, intraperitoneal). Following thoracotomy, the left anterior descending coronary artery (LAD) was ligated to induce acute myocardial infarction. The MI group received an intramyocardial injection of 10 μL PBS mixed with 10 μL Growth Factor Reduced Matrigel™ Matrix (Corning, Berlin, Germany). The MI induction plus cell transplantation (MIC) group received a suspension of 1×10^6 syngeneic in PBS (10μL) mixed with 10 μL Growth Factor Reduced Matrigel™ Matrix. Injections of 4 × 5 μL were given along the infarct border. The injection site was controlled visually at the time of transplantation [10].

Healthy mice (n = 33) were divided into 7 groups for 18F-FDG PET imaging 5 days following MI using different protocols for anaesthesia:

(1) no intervention, isofluorane (n = 2)
(2) no intervention, ketamine/xylazine (n = 2)
(3) MI group, isofluorane (n = 4)
(4) MI group, ketamine/xylazine (n = 6)
(5) MIC group, ketamine/xylazine (n = 7)

Cardiac function was assessed in separate groups three weeks following MI by cardiac MRI:

(6) MI only (n = 6)
(7) MIC (n = 6)

Flow cytometric analysis was performed in separate groups (MI, n = 5 and MIC, n = 5).

2.3. qRT-PCR

RNA was isolated from the cells using the NucleoSpin® RNA isolation kit (Macherey-Nagel, Dueren, Germany). First strand cDNA was then synthesized using the cDNA synthesis kit (Thermo Fisher Scientific, Waltham, MA, USA) according to the manufacturer's instructions. The qPCR reaction was then carried out with the Taqman® Universal PCR Master Mix (Thermo Fisher Scientific) and performed on a StepOnePlus Real-Time PCR system (Applied Biosystems, Foster city, CA, USA). Primers of the following target genes: *Pou5f1* (Mm00658129_gH), *cTnnt2* (Mm01290256_m1), *MesP1* (Mm00801883_m1), and *Nkx2.5* (Mm01309813_s1) were purchased from Thermo Fisher Scientific. Gene expression values of the target genes at day 6 were then normalized to the housekeeping gene *Hprt* (Mm00446968_m1; Thermo Fisher Scientific) and compared relative to the expression values at day 0 using the ΔΔCt method for relative quantifications.

2.4. Beating Foci Analysis

The number of beating foci per EB was analyzed from day 7 to day 30 of differentiation. The EB were observed under a microscope (Carl Zeiss, Oberkochen, Germany) and the beating foci per each EB were then visually analyzed using the ZEN2011 software (Carl Zeiss).

2.5. Flow Cytometry

Single cell cardiac monocyte suspensions were prepared for flow cytometry, as previously described [11] Briefly, the remote and infarct tissue of the heart was dissected and enzymatically digested separately in HBSS with Ca^{2+} and Mg^{2+}(450 U/mL collagenase type I, 125 U/mL collagenase type XI, 120 U/mL DNase I, 60 U/mL hyaluronidase, all Sigma-Aldrich) for 30 min at 37 °C. The digested samples were then passed through a 100 µm filter and centrifuged to enrich for mononuclear cells. Red blood cells were then lysed using erythrocytes lysis buffer (eBioscience, San Diego, CA, USA) and the digest was then washed and suspended in MACS® buffer (PBS, 2 mM EDTA, 0.5% BSA). Samples were then labeled using Zombie Aqua dye (BioLegend, San Diego, CA, USA.), washed, resuspended in MACS buffer containing FCR Block (Miltenyi Biotec GmbH, Bergisch Gladbach, Germany), and stained (see Table 1 for antibody list). Stained samples were then analyzed on a BD FACS LSR II® running BD FACS Diva software (version 6.1.2, Franklin Lakes, NJ, USA). The various immune cell populations in the heart tissue were then assessed, as described in Figure 1.

Table 1. Antibodies used for flow cytometry.

Target	Clone	Source
CD45	30-F11	Biolegend
CD11b	M1/70	Biolegend
CD11c	N418	Biolegend
NK1.1	PK136	Biolegend
Ly6G	1A8	Biolegend
Ly6C	Hk1.4	Biolegend
CCR2	475301	R and D
MHC-II	AF6-120.1	Biolegend

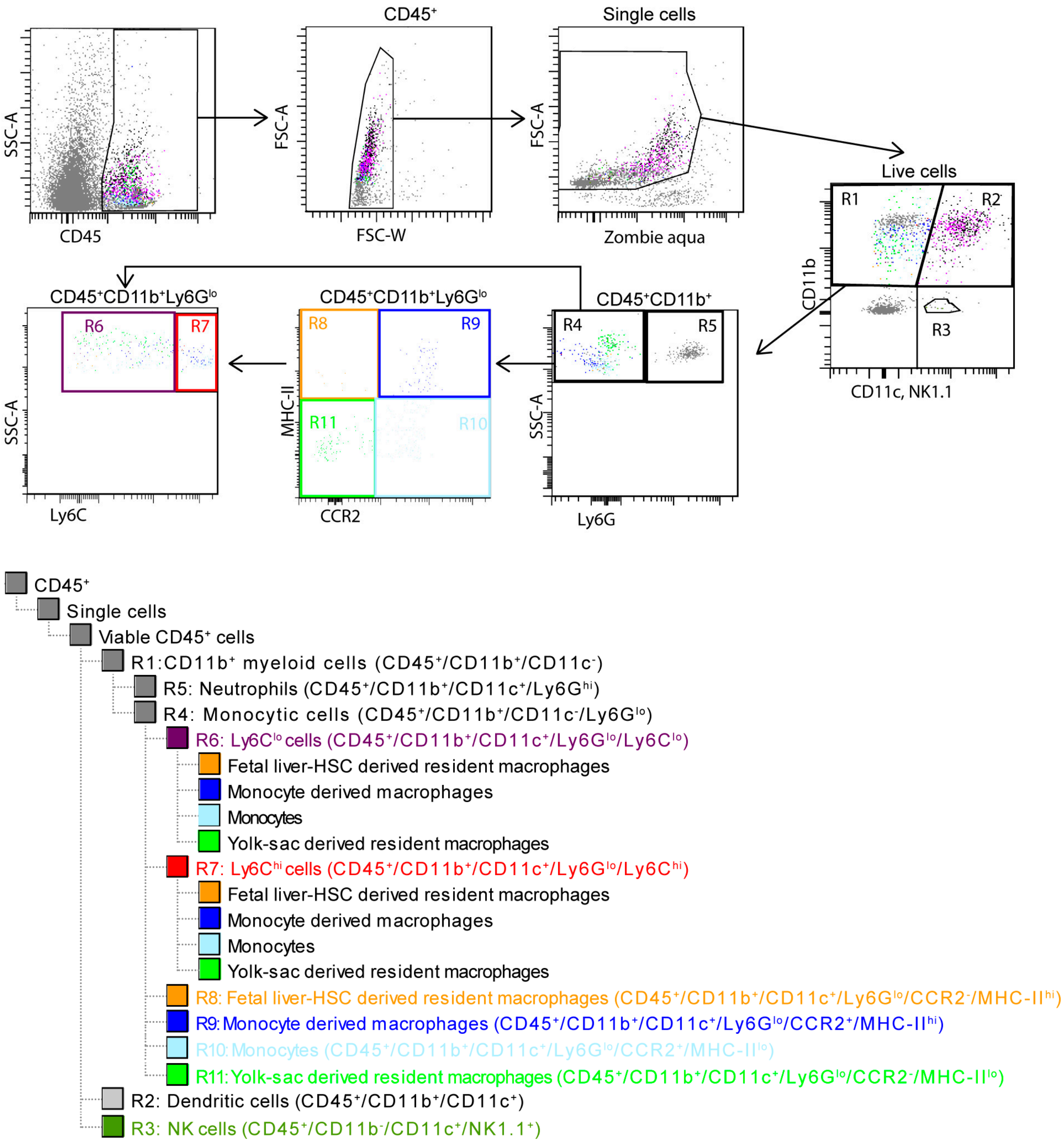

Figure 1. Gating strategy for identifying the different immune populations in the heart. Mononuclear cells expressing CD45 were gated and doublets (FSC-W vs. FSC-A) were excluded. Dead cells were excluded by Zombie aqua. The live single CD45$^+$ cells were then grouped into R1, CD11b+ myeloid cells (CD45$^+$/CD11b$^+$/CD11c$^-$); R2, dendritic cells (CD45$^+$/CD11b$^+$/CD11c$^+$); and R3, NK cells (CD45$^+$/CD11b$^-$/CD11c$^-$/NK1.1$^+$) based on their relative expression of CD11b and CD11c. R5, neutrophils (CD45$^+$/CD11b$^+$/CD11c$^-$/Ly6G^{hi}) were then excluded from R1 based on their Ly6G expression. The remaining R4 monocytic cells were then further characterized into R6, Ly6C^{hi} or commonly known as M1 cells (CD45$^+$/CD11b$^+$/CD11c$^-$/Ly6G^{lo}/Ly6C^{hi}); R7, Ly6C^{lo} or commonly known as M2 cells (CD45$^+$/CD11b$^+$/CD11c$^-$/Ly6G^{lo}/Ly6C^{lo}) based on their Ly6C expression; and into R8, fetal liver HSC-derived resident macrophages (CD45$^+$/CD11b$^+$/CD11c$^-$/Ly6G^{lo}/CCR2$^-$/MHC-II^{hi}); R9, monocyte derived macrophages (CD45$^+$/CD11b$^+$/CD11c$^-$/Ly6G^{lo}/CCR2$^+$/MHC-II^{hi}); R10, monocytes (CD45$^+$/CD11b$^+$/CD11c$^-$/Ly6G^{lo}/CCR2$^+$/MHC-II^{lo}); and R11, yolk sac-derived resident macrophages (CD45$^+$/CD11b$^+$/CD11c$^-$/Ly6G^{lo}/CCR2$^-$/MHC-II^{lo}) based on their CCR2 and MHC-II expression. These CCR2 and MHC-II gated populations were then back gated on R6 and R7 and their relative contribution to the M1 (Ly6C^{hi}) and M2 (Ly6C^{lo}) cells was assessed.

2.6. PET Imaging

For the PET study, mice of the groups 1,3, 6, and 7 were anaesthetized by inhalation of isoflurane (4% for induction and 1% to 2.5% maintenance during preparation and scanning), whereas mice of the groups 2,4, and 5 were anaesthetized by i.p. injection of ketamine/xylazine (ketamine 84 mg/kg and xylazine 11.2 mg/kg) 20 min before tracer application. All PET/CT scans were performed on a small animal PET/CT scanner (Inveon MM-PET/CT, Siemens Medical Solutions, Knoxville, TN, USA) [12] according to a standard protocol: Mice were injected intravenously with a dose of approximately 10 MBq 18F-FDG via a custom-made micro catheter placed in a tail vein. After an uptake period of 60 min, mice were imaged in prone position for 20 min. During the imaging session, respiration of the mice was controled and core body temperature was constantly kept at 38 °C via a heating pad. For attenuation correction and anatomical reference, whole body CT scans were acquired. CT images were reconstructed with a Feldkamp algorithm. The PET images were reconstructed with the three-dimensional (3D) iterative ordered subset expectation maximization reconstruction algorithm (3D-OSEM/OP-MAP) with the following parameters: 4 iterations (OSEM), 32 iterations (MAP), 1.7 mm target resolution, and 128 × 128 matrix size. Reconstruction included corrections for random coincidences, dead time, attenuation, scatter, and decay.

2.7. PET Image Analysis

Image analyses were performed using an Inveon Research Workplace (Siemens, Knoxville, TN, USA), as described previously [13]. PET (Positron emission tomography) and CT (Computerized tomography) images were fused by the use of an automated volumetric fusion algorithm and then verified by an experienced reader for perfect alignment. Consecutively, standardized representative volumes of interest (VOI) were manually placed in the remote area and in the infarcted region as well as the whole heart guided by anatomical landmarks, as described in detail in Figure 2. Correct VOI positioning was visually verified in axial, coronal, and sagittal projection.

Carimas 2 software (Turku PET Centre, Turku, Finland) was used for generating polar maps of the left ventricle according to the manual provided by the developer. Results are presented using 17-segmental standardized myocardial segmentation.

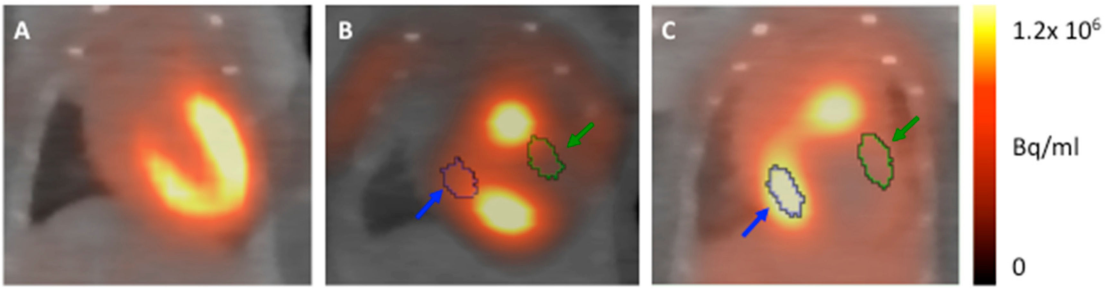

Figure 2. Representative images visualizing our volumes of interest (VOI) positioning strategy: (**A**) Myocardium of healthy mice anaesthetized with isofluorane can be clearly delineated and served as a reference for VOI positioning. (**B** and **C**) Anaesthesia with ketamine/xylazine. A VOI of 5 µL was positioned in both anterolateral wall (infarct area, green) and remote area (inferobasal, blue). Thereby both anatomical landmarks form the CT scan and the image of healthy myocardium (**A**) was used.

2.8. Cardiac Magnetic Resonance Imaging

Cardiac magnetic resonance (CMR) measurements were performed on a 7 Tesla small animal MRI system (BioSpec 70/30, maximum gradient strength 440 mT/m, Bruker BioSpin Gmbh, Ettlingen, Germany) equipped with a 1H transmit volume coil (86 mm, volume resonator) and a 2-by-2 receive-only surface coil array (both Bruker BioSpin GmbH). After induction of anaesthesia using 2% to 3.5% isoflurane in oxygen, animals were placed in a supine position on a dedicated mouse bed and surface coil was placed on the chest of the mice. Respiration rate and body temperature were monitored using an MR-compatible small animal monitoring and gating system (Model 1030, SA Instruments, Inc., Stony Brook, NY, USA), and stable body temperature was maintained by a warm water heating. Anaesthesia was maintained during the experiment with isoflurane oxygen (1.5% to 2%) to achieve a respiration rate of about 35 to 55 breaths.

After planning sequences, for the short axes view final images of the left ventricular ejection fraction (LVEF) measurements were acquired using a IntraGate gradient-echo cine sequences (IntraGate Cine-FLASH) in six short-axis planes completely covering the left ventricle. Acquisition parameters included: echo time (TE) 2.38 ms, repetition time (TR) 5.89 ms, flip angle 15°, 14 frames per cardiac cycle, oversampling 140, averages 1, field of view (FOV) 29.4 × 25.2 mm, matrix size 211 × 180, resolution in-plane 0.14 × 0.14 mm, slice thickness 1 mm, and scan time per slice 2 min.

2.9. Cardiac Magnetic Resonance Analysis

LVEF was assessed from the cine sequences using the freely available software Segment v2.0 R5165 (Medviso, Lund, Sweden) (http://segment.heiberg.se) [14]. The left ventricular (LV) endocardium in these slices was manually segmented to exclude the papillary muscles. The volumes of these segments were then integrated along the six planes of the LV and LVEF was then calculated from their summated end systolic and end diastolic volumes.

2.10. Statistics

All data are presented as mean values ± standard deviation (SD). Flow cytometric data and qPCR values are presented as mean values ± standard error of mean. Student's *t*-test was used for statistical analysis of parametric data and the Mann–Whitney test was used for nonparametric analysis of flow cytometric data. Values of $p < 0.05$ were considered statistically significant.

3. Results

3.1. Cardiac Induced Cells Show Increased Cardiac Markers and Beating Activity During Differentiation

In order to ascertain the differentiation status of the cells, we examined the expression of various markers at the beginning and at day six of differentiation (Figure 3A). We observed the expression of early cardiac markers such as *MesP1*, *Nkx2.5*, and cardiac troponin (*cTnnt2*). They were increased several fold at day six, whereas the expression of the pluripotency marker, *Pou5f1* (also known as *Oct4*), was strongly decreased. This indicates the cardiac lineage commitment of the cells. We also investigated the beating activity of the cells along the differentiation process to determine their functional capability (Figure 3B). In accordance with the strong induction with the induction of the cardiac markers, the cells were robustly beating and the number of beating foci per EB consistently increases over time till day 30 of differentiation. Therefore, these cardiac-induced cells have committed to the cardiac lineage with the potential to form beating cells in the host after transplantation.

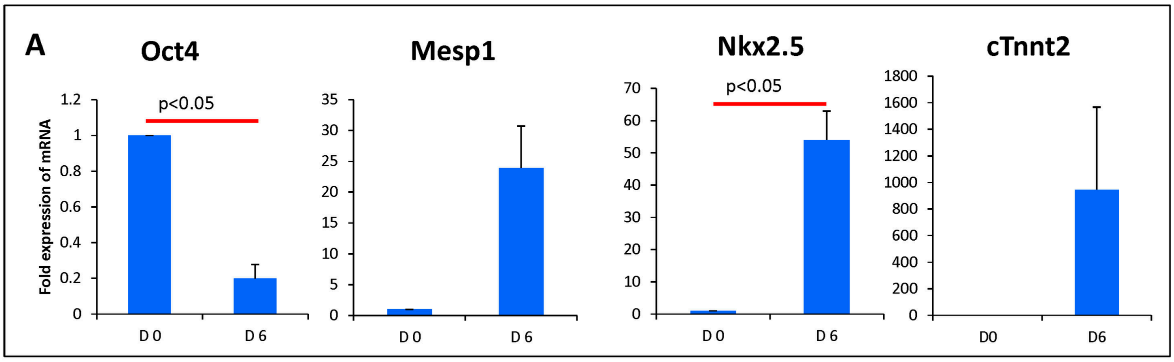

Figure 3. *Cont.*

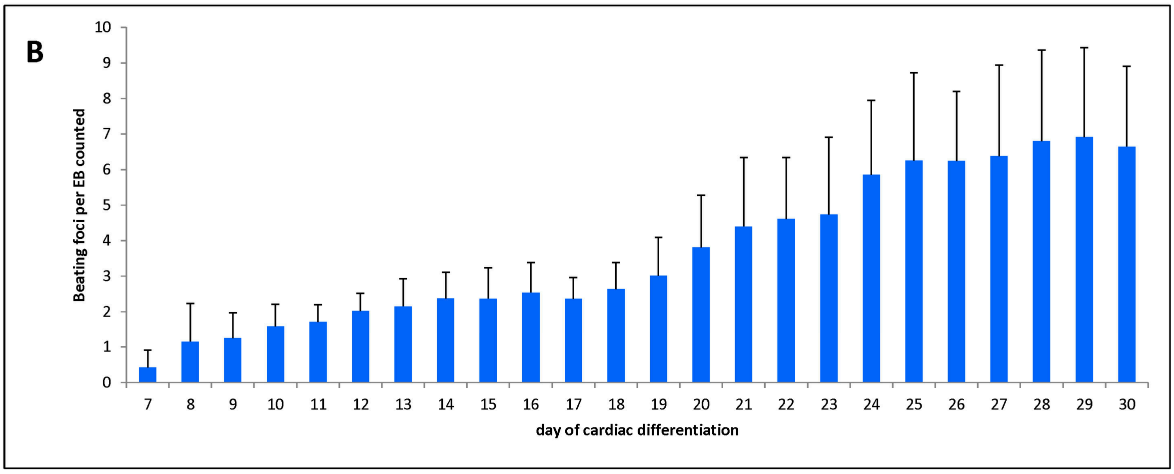

Figure 3. Characterization of cardiac-induced cells: (**A**) Analysis of mRNA expression after six days of cardiac differentiation shows a decrease of the pluripotency marker *Oct4*, whereas cardiac markers are upregulated. The mRNA expression was normalized to the expression of the house keeping gene *hprt*. Values are expressed as fold increase as compared with day 0. Values are presented as mean ± SEM. (**B**) Starting at day 7 of the cardiac differentiation protocol, beating foci per embryoid bodies (EB) were counted until the end of differentiation (n = 3). Values are presented as mean ± SD. *p*-value was calculated using the student *t*-test.

3.2. Impact of Anaesthesia on the FDG-Uptake Pattern in the Infarcted Heart

First, we examined if the myocardial glucose uptake suppression protocol established by Thackeray et al. [5] for C57BL/6 J mice can be applied in the mouse strain 129Sv used in our study on healthy mice (Figure 4).

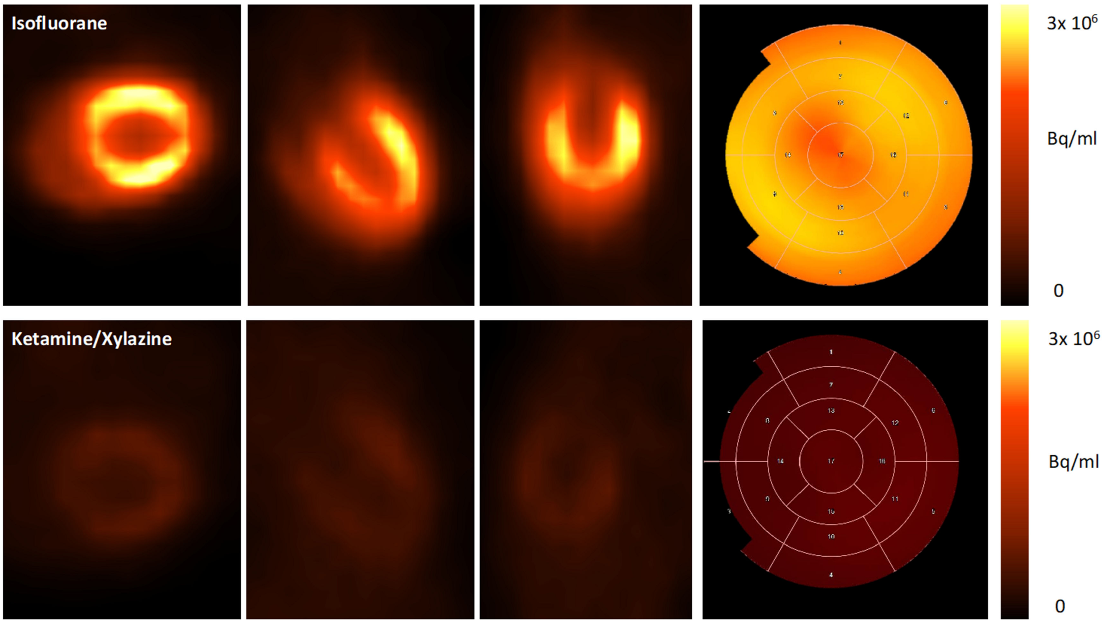

Figure 4. Representative images of healthy mice anaesthetized with isofluorane (upper row) and ketamine/xylazine (lower row). Uptake of 18F-FDG is effectively suppressed by the use of ketamine/xylazine as can be seen in axial, coronal, and sagittal planes, as well as the polar maps.

Secondly, 18F-FDG PET was performed five days after permanent LAD ligation. Under anaesthesia with isofluorane, the highest tracer accumulation was detected in the viable myocardium, whereas ketamine/xylazine (KX) led to accentuated tracer accumulation within the border zone (Figure 5).

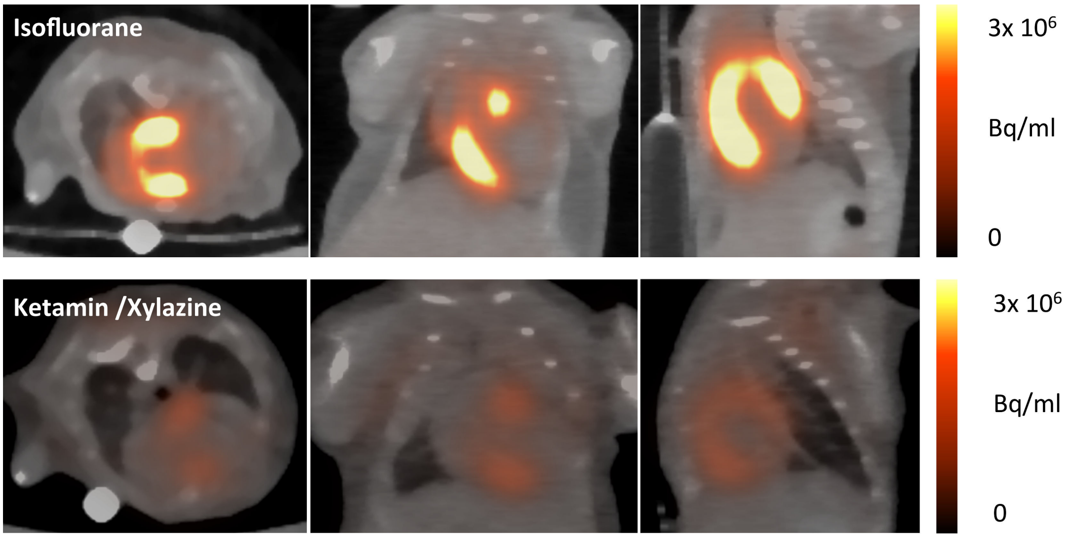

Figure 5. Sample axial, coronal, and sagittal myocardial 18F-FDG images at five days post-surgical myocardial infarction (MI) induction. Isofluorane leads to high tracer accumulation in the healthy myocardium, whereas the infarcted area can be clearly identified as an area of low glucose metabolism (upper row). When using ketamine/xylazine, the most intense tracer accumulation is detected in the area of the border zone, whereas 18F-FDG uptake in healthy myocardium remains suppressed.

The 18F-FDG uptake was significantly reduced by the use of ketamine/xylazine as compared with isofluorane for anaesthesia in the whole heart (5.2 ± 0.7% ID/g vs. 46.1 ± 11.2% ID/g; $p = 0.02$) and both remote (4.1 ± 0.6% ID/g vs. 79.3 ± 22.7% ID/g; $p < 0.0001$) and infarcted myocardium (4.35 ± 0.4% ID/g vs. 11.6 ± 6.0% ID/g, $p = 0.002$) (Figure 6).

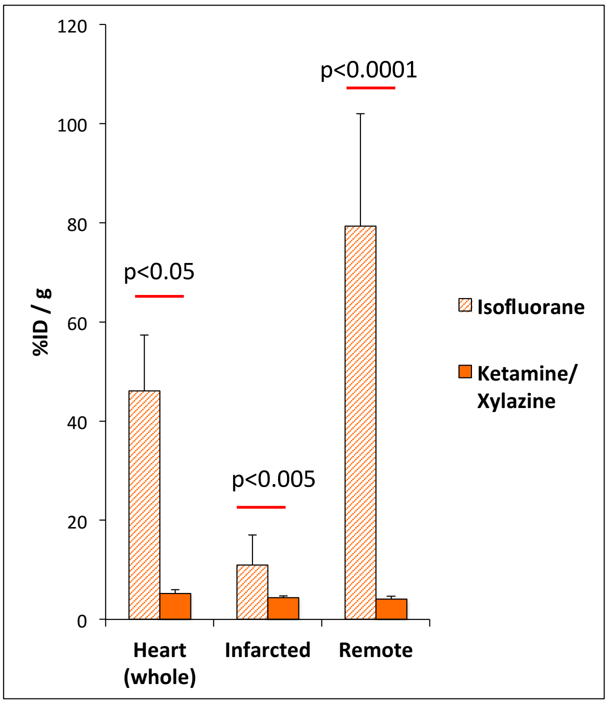

Figure 6. Regional quantitative analysis of 18F-FDG uptake five days after myocardial infarction in the whole heart, the infarct and the remote myocardium. Mice were anaesthetized with isofluorane or ketamine/xylazine, respectively. Values are presented as mean ± SD. p-value was calculated using the student t-test.

With KX, there was no difference in tracer uptake between remote and infarcted myocardium (4.1 ± 0.6% ID/g vs. 4.4 ± 0.4% ID/g; $p = 0.5$). In contrast isoflurane lead to significantly higher 18F-FDG uptake in the remote as compared with the infarcted myocardium (79.3 ± 22.7% ID/g vs. 11.6 ± 6.0% ID/g; $p = 0.001$).

3.3. FDG-Uptake Pattern is Fundamentally Changed by Cell Transplantation

We then compared 18F-FDG uptake patterns in untreated to animals treated with CiC therapy (MIC) using the ketamine/xylazine protocol (Figures 7 and 8). Transplantation of embryoid bodies containing 10^6 syngeneic cardiac induced cells following acute myocardial infarction led to an increase in 18F-FDG uptake in the remote myocardium as compared with the MI group (10.7 ± 4.3% ID/g vs. 4.1 ± 0.6% ID/g; p = 0.003) (Figure 9). Interestingly, tracer accumulation in the center of the infarcted area was not altered by cell therapy (4.3 ± 1.4% ID/g in MIC vs. 4.4 ± 0.4% ID/g in MI; $p = 0.9$). Furthermore 18F-FDG uptake in the whole heart was significantly increased in the MIC group (8.0 ± 2.9% ID/g vs. 5.2 ± 1.1% ID/g; $p < 0.05$).

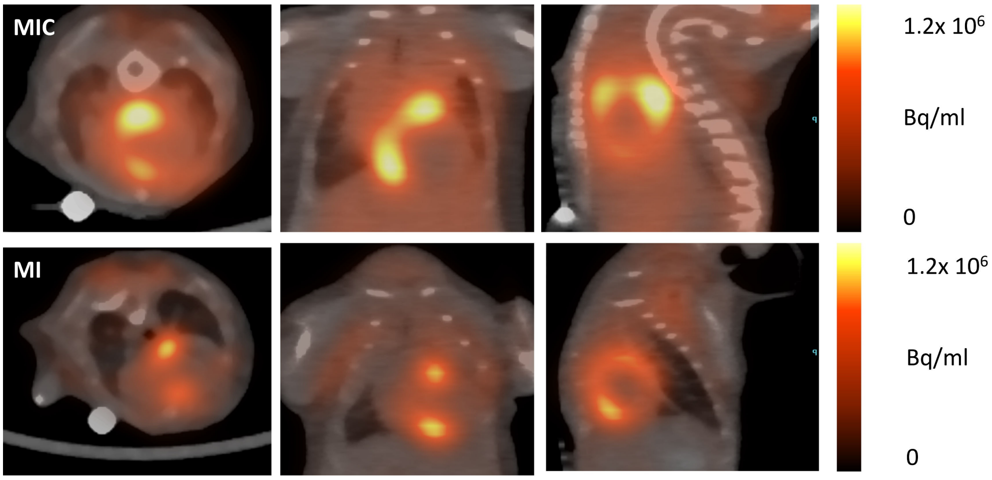

Figure 7. Sample axial, coronal, and sagittal myocardial 18F-FDG images at five days post-surgical MI induction and MI induction plus cell transplantation (MIC). Mice were anaesthetized with ketamine/xylazine. The MI group showed intense tracer accumulation in the border zone, whereas in cell-treated animals the highest tracer accumulation was found in the remote area.

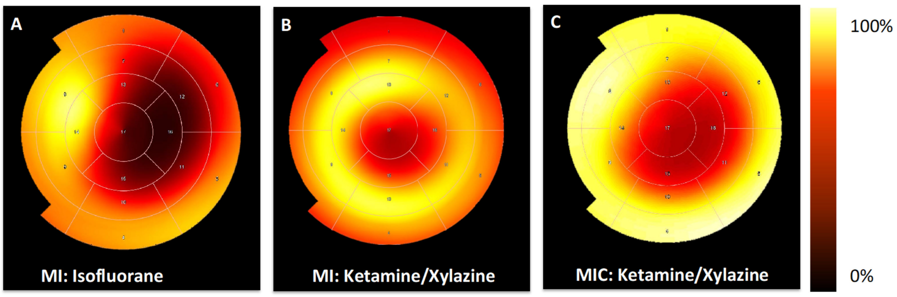

Figure 8. Representative 17-segment tomographic polar maps visualizing distinctive differences of FDG-distribution in the left ventricle between the groups. The apex is in the middle and the anterior wall at top, the inferior wall at bottom, the septum in left and the lateral wall in the right. High tracer uptake is visualized by the yellow colors, lower upake by red and black. (**A**) MI group anaesthetized with isofluorane, the infarct region shows low FDG uptake as compared with remote myocardium; (**B**) MI group anaesthetized with ketamine/xylazine, the most intense FDG uptake came in the border zone; and (**C**) MI + cardiac induced cells (CiC) group anaesthetized with ketamine/xylazine shows a change of the FDG uptake to a pattern, which is similar to (A) with low FDG accumulation within the infarct region and highest uptake in the remote area.

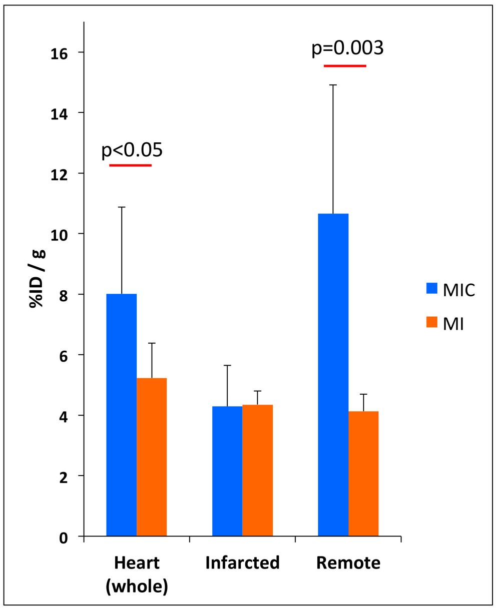

Figure 9. Regional quantitative analysis of 18F-FDG uptake five days after myocardial infarction in the whole heart, infarct, and remote myocardium. Both MI and MIC group were anaesthetized using ketamine/xylazine. Values are presented as mean ± SD. *p*-value was calculated using the student *t*-test.

3.4. Improvement of Cardiac Function Through Cell Therapy Assessed by CMR

In order to assess the value of 18F-FDG-based imaging of cellular inflammation post-MI as an early predictor of functional outcome following cardiac cell therapy, cine CMR was performed three weeks after LAD ligation in separate groups. LVEF was significantly reduced by LAD ligation as compared with healthy animals (24.2 ± 4.1% vs. 59.3 ± 3.7%; $p < 0.001$). Cell therapy led to a significant increase of LVEF (31.7 ± 3.5% vs. 24.2 ± 4.1%; $p = 0.007$) (Figure 10). From this we conclude, that the change in the 18F-FDG uptake pattern, as described above, is a valuable early predictor of therapeutic efficacy.

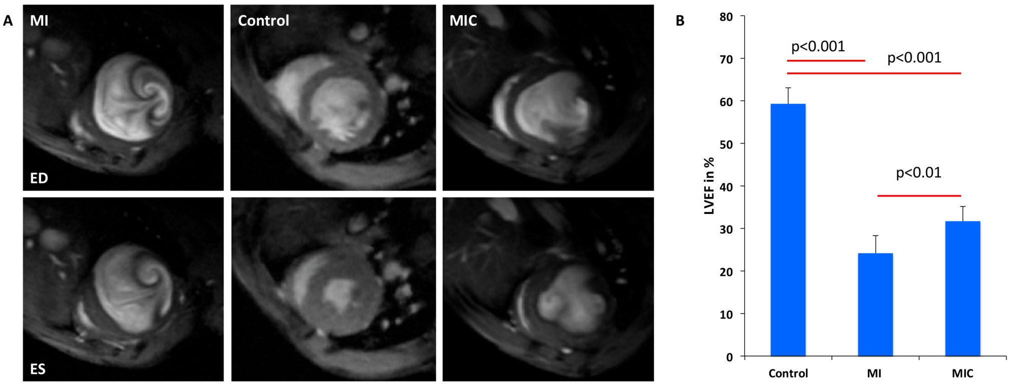

Figure 10. Improved cardiac function after transplantation of embryonic stem cells (ESC) derived CiC following acute myocardial infarction at 3 weeks following MI. (**A**) Magnetic resonance imaging analyses of infarcted animals receiving either CiC (MIC) or matrigel and healthy animals and (**B**) left ventricular ejection fraction was significantly higher in CiC animals vs. control animals (n = 6, *p*-value was calculated using the student *t*-test).

3.5. Modulation of the Immune Response Through Cell Therapy Assessed by Flow Cytometry

In order to identify the immune response within the myocardium, we analyzed the mononuclear cell (MNC) suspension isolated from the remote and infarct area of the hearts of 129Sv mice five days after MI or MIC (Figure 1).

We observed a significantly higher percentage of NK cells ($CD45^+/CD11b^-/CD11c^+/NK1.1^+$) in the infarct area (0.82 ± 0.04 vs. 0.56 ± 0.03; $p = 0.01$) as compared with the remote area in MI mice. Cell therapy influences the various immune subpopulations differently in infarct and remote areas of the heart. On the one hand, cell therapy led to a significantly higher percentage of $CD11b^+$ myeloid cells (Figure 11A) in the remote area (49.28 ± 3.92 vs. 31.17 ± 2.72; $p = 0.01$) of MIC hearts as compared with MI hearts. This agrees well with the increased 18F-FDG uptake observed in the remote area of MIC mice (Figure 9), which has been attributed mainly to $CD11b^+$ cells [1]. On the other hand, cell therapy led to a decrease in the percentage of NK cells (Figure 11A) in the infarct area (0.41 ± 0.05 vs. 0.82 ± 0.04; $p = 0.007$) when compared to MI hearts.

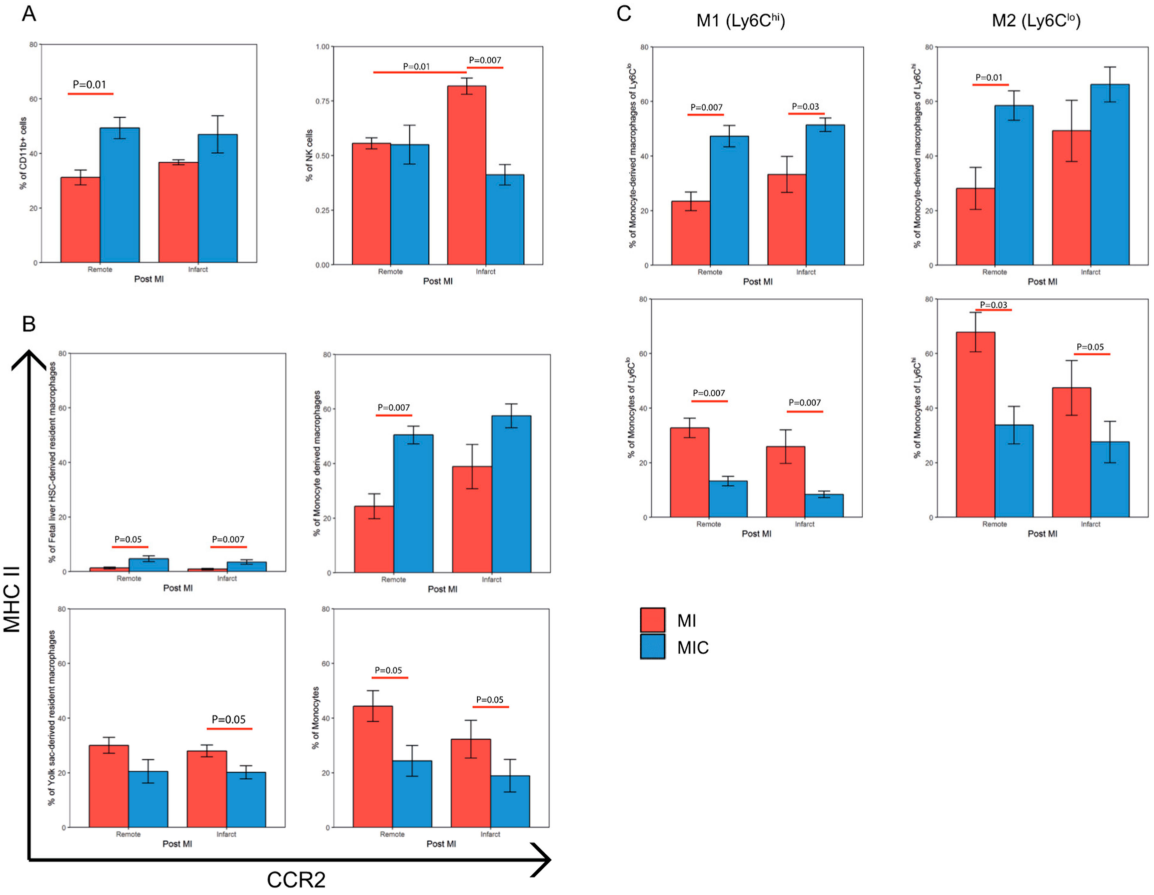

Figure 11. Effect of CiC transplantation on the percentage of various immune cell subpopulations in the heart based on flow cytometric analysis. Mice were subjected to MI/MI+ cells and the remote and infarct area of the hearts were dissected, digested, and the isolated mononuclear cells were stained using various antibodies. These immune cell populations were then characterized using the gating strategy described before and represented as three major groups. (**A**) $CD11b^+$ and NK cells, (**B**) populations based on their CCR2/MHC-II expression, and (**C**) contribution of the populations towards the M1 ($Ly6C^{hi}$) and M2 ($Ly6C^{lo}$) cells, n = 5. Values are represented as mean ± SEM. Significance was calculated using the Mann–Whitney test.

Interestingly, we also observed various differences in various $CD11b^+$ subpopulations based on their relative CCR2 and MHC-II expression between the MI and MIC groups (Figure 11B,C).

In the remote area, cell therapy led to an increase in the percentage of fetal liver HSC-derived resident macrophages (4.68 ± 1.03 vs. 1.29 ± 0.32; $p = 0.05$) and an increase in the percentage of monocyte-derived macrophages (50.48 ± 3.24 vs. 24.35 ± 4.54; $p = 0.007$), and their relative contribution to the percentage of M1 ($Ly6C^{hi}$) (58.48 ± 5.41 vs. 28.11 ± 7.72; $p = 0.01$) and M2 ($Ly6C^{lo}$) (47.28 ± 3.95 vs. 23.39 ± 3.38%; $p = 0.007$) cells along with a subsequent decrease in the percentage of monocytes

(24.33 ± 5.61 vs. 44.36 ± 5.62; $p = 0.05$) and their relative contribution to the percentage of M1 (Ly6C^{hi}) (33.76 ± 6.9 vs. 67.85 ± 7.22; $p = 0.03$) and M2 (Ly6C^{lo}) (13.25 ± 1.74 vs. 32.71 ± 3.56; $p = 0.007$) cells as compared with MI.

In the infarct area, we observed an increase in the percentage of fetal liver HSC-derived resident macrophages (4.68 ± 1.03 vs. 1.29 ± 0.32; $p = 0.05$) as well as monocyte-derived macrophages (57.46 ± 4.37 vs. 38.89 ± 8.13) and their relative contribution to the percentage of M2 (Ly6C^{lo}) (51.44 ± 2.47 vs. 33.25 ± 6.6%; $p = 0.03$) cells with a subsequent decrease in the percentage of monocytes (18.88 ± 5.99 vs. 32.25 ± 6.88; $p = 0.05$) and their relative contribution to the percentage of M1 (Ly6C^{hi}) (27.6 ± 7.59 vs. 47.4 ± 10.04; $p = 0.05$) and M2 (Ly6C^{lo}) (8.39 ± 1.17 vs. 25.85 ± 6.15; $p = 0.007$) along with a decrease in the percentage of yolk sac-derived resident macrophages (20.16 ± 2.43 vs. 27.95 ± 2.15; $p = 0.05$) as compared with the MI group.

Therefore, CiC transplantation in the heart increases the CD11b$^+$ cells in the remote area of the heart while favoring an increase in the MHC-II^{hi} subset of CD11b$^+$ cells (monocyte derived macrophages and fetal liver HSC-derived resident macrophages) in both the infarct and remote areas.

4. Discussion

Translational cardiovascular research has evolved at an incredible pace within the last decade and resulted in significantly higher survival rates after acute myocardial infarction. In contrast to highly efficient approaches based on early revascularization and pharmacological prevention of adverse ventricular remodeling, replacement of irreversibly lost cardiomyocytes has not been achieved yet, despite huge efforts in the field of regenerative medicine.

Recently, cellular inflammation following ischemic myocardial injury has been identified as a key player in the process of myocardial healing. Thereby, the local distribution patterns of specific monocyte and macrophage subpopulations have been proposed to determine the quality of myocardial healing [15,16].The vast majority of data has been obtained from rodent studies because their hearts can easily be excised for in vitro experiments such as flow cytometric measurements of single cells suspensions. Most researchers focus on the invasion of two distinct macrophage subpopulations, usually referred to as M1 and M2 macrophages. The early M1 macrophage subset is attracted to the site of myocardial injury via CCL2, expressing pro-inflammatory mediators and proteases for degradation of infarcted tissue. Subsequently, M2 macrophages are recruited via CX3CL1 for mediating synthesis of extracellular matrix and angiogenesis [3]. However, the M1/M2 classification does not adequately explain the complete spectrum of macrophage phenotypes. Recently, macrophages which do not express CCR2 in the neonatal heart have been shown to regenerate the infarcted tissue [15] while the adult heart involves CCR2$^+$ monocyte-derived macrophages also taking part in the remodeling process [17].

Preclinical studies have examined the effect of therapeutic applications, such as stem cell injections, to modify the qualitative and quantitative composition of the post infarct cellular immune response [18–20]. This modulation of the innate cellular immune response resulted in improved cardiac pump function, reduction of scar size, and adverse remodeling [18]. Findings from a meta-analysis by our group have ascribed high therapeutic potential to cardiovascular cell preparations [21]. Therefore, we sought to transplant ESC-derived cardiac induced cells to improve myocardial healing and also investigate whether they influence the ischemic cellular immune response.

The above-mentioned experiments are based on post-mortem analyses such as flow cytometry and immunohistochemistry of excised organs, and thus have been restricted to preclinical research. However, clinical translation requires methods that allow in-vivo visualization and quantification of inflammatory cells. Lee et al. established 18F-FDG PET for imaging the inflammatory cell activity in the heart, based on suppressing glucose metabolism in myocytes [1]. Interestingly, anaesthesia with ketamine/xylazine is both sufficient and highly effective in reducing glucose uptake in cardiomyocytes, hence, enabling visualization of inflammatory activity in the heart [1]. According to Lee et al., 18F-FDG uptake at the site of myocardial inflammation related to the content of local CD11b$^+$ monocyte/macrophage concentration in C57BL6 mice [1], at day 5 after MI induction.

On the basis of these findings by other groups, we hypothesized the following:

(A) Distribution pattern of CD11b$^+$ myeloid cells at day five after MI induction can be modified by intramyocardial transplantation of CiC;
(B) This change can be visualized and quantified by 18F-FDG PET using ketamine/xylazine anaesthesia;
(C) The specific 18F-FDG uptake pattern correlates with functional outcome as measured by cardiac magnetic resonance imaging.

We were able to replicate the glucose uptake suppression protocol based on anaesthesia with KX [5] in 129sv mice and achieved an almost 88% reduction in the glucose uptake in the whole myocardium as compared with isoflurane anaesthesia. We did not find any significant difference in the 18F-FDG uptake levels between the remote and infarcted myocardium using KX anaesthesia, which is in line with findings from Thackeray et al. [4,5]. Furthermore, intense focal tracer uptake was localized in the border zone. Similarly, Lee et al. also reported accentuated FDG uptake in the border zone corresponding to high numbers of infiltrating CD11b$^+$ cells [1]. Despite visual assessment of this high focal tracer accumulation, quantitative analysis in this region was only performed by Thackeray et al. However, their VOI positioning strategy remains unclear from the manuscript. This might be due to a certain overlap of the border zone to the adjacent regions which makes demarcation of the border zone difficult. In order to produce comparable data in this aspect, VOI positioning strategies should be provided in future studies.

Interestingly, transplantation of 10^6 cardiac induced cells after MI significantly increased FDG uptake in both the whole heart and the remote myocardium, but not in the infarct region. Moreover, CiC transplantation led to a 7% improvement in LVEF three weeks after MI. The magnitude of LVEF improvement is well in line with previous reports [21]. Therefore, we conclude that the change in the myocardial 18F-FDG uptake pattern represents a valid tool for early PET-based in vivo prediction of myocardial healing post MI.

A deeper investigation of the immune response in the heart five days after MI using flow cytometry revealed an increase in the percentage of CD11b$^+$ cells and a shift towards increased monocyte-derived macrophages in the remote area of cell-treated mice. We also observed a reduction in the yolk sac-derived resident macrophages in the infarct area of cell-treated mice. We did not however observe a shift in the M1/M2 polarization phenotype, as observed in previous studies involving MSCs [18]. It is interesting to note that increased monocyte-derived macrophages and reduced yolk sac-derived macrophages in the heart have been previously attributed to adverse cardiac remodeling and scar formation [17]. However, these studies did not involve the transplantation of cells into the infarcted heart and it is well known that the gene expression profile and the characteristics of the immune cells are affected based on their location in the myocardium and the cells they interact with [22].

However, unbiased expression profiling of these cells over various time points and under the influence of CiC has yet to be carried out. The influence of CiC transplantation on the immune response in the heart has not been studied until now and our work suggests possible new mechanisms and targets for improving the efficiency of CiC.

The 18F-FDG-based imaging strategies for myocardial inflammation are highly attractive and have been applied in a clinical setting despite some limitations, which have yet to be overcome [3]. Both cardiomyocytes [4] and infiltrating inflammatory cells [23] in the setting of acute myocardial injury possess high levels of glucose metabolism. Metabolism of healthy cardiomyocytes is mainly based on fatty acid oxidation, whereas ischemia triggers increased anaerobic glycolysis, which requires much higher rates of glucose [24]. This might hamper direct correlation of focal 18F-FDG uptake and high concentration of CD11b$^+$ cells in the infarcted region. The use of KX for anaesthesia has been shown to reduce serum insulin levels in rodents, thus, preventing translocation of GLUT4 to membranes of cardiomyocytes and reducing 18F-FDG uptake [25]. In contrast, leucocyte glucose influx in a setting of acute inflammation depends more on GLUT1 and GLUT3, which are expressed and translocated independently of insulin [26]. Whereas, this KX protocol is well suited for preclinical research, different strategies are used for suppression of myocardial glucose uptake in patients including prolonged fasting, dietary modifications, and heparin loading before imaging [27]. This might hamper straightforward translation of imaging protocols established in rodents to clinical application.

Furthermore, the transplantation of CiC adds more complexity to its use in imaging the myocardium. It becomes difficult to attribute the observed 18F-FDG uptake pattern to the inflammatory cells alone since the ability of CiC to alter the cardiac metabolism is poorly understood. It is, therefore, difficult to delineate the relative contribution of 18F-FDG uptake between the host cardiomyocytes, immune cells, and the CiC. The heterogeneity of the inflammatory response and the relative 18F-FDG uptake between the different immune cell populations is also clearly not understood. Further research is necessary to understand metabolic changes in the different cells involved in healing myocardium.

Nevertheless, this is the first study to investigate 18F-FDG-based PET imaging of inflammation as an early indicator for assessing long term therapeutic efficiency in a rodent model of acute myocardial infarction. Furthermore, the current work illustrates the benefit of CiC transplantation to improved cardiac function after MI possibly through its beneficial modulation of the innate inflammatory response. Using such non-invasive techniques in the field of translational research will foster a better understanding of the inflammatory response and how its modulation could lead to altered cardiac function. It is also a valuable tool for monitoring various immune modulation and cell therapies and broadens the horizon for understanding the mechanisms of these therapeutic strategies.

Author Contributions: Conceptualization, C.I.L. and P.V.; methodology, T.L., J.S., and J.K.; formal analysis, C.I.L., P.V., and P.D.; investigation, C.I.L., P.V., R.G., P.M., and H.L.; writing—original draft preparation, P.V. and C.I.L.; writing—review and editing, J.K., R.D, G.S., and H.I.; visualization, P.V. and C.I.L; supervision, C.I.L. and R.D.; funding acquisition, C.I.L., R.D, B.J.K., and B.V.

Funding: This work was supported by the Federal Ministry of Education and Research Germany (FKZ 0312138A and FKZ 316159), the State Mecklenburg-Western Pomerania with EU Structural Funds (ESF/IVWM-B34-0030/10 and ESF/IVBM-B35-0010/12) and the DFG (DA1296/6-1), the German Heart Foundation (F/01/12) and the German Heart Research Foundation (F/34/15). In addition, R.D. is supported by the EU Structural Fund (ESF/14-BM-A55-0024/18), the FORUN Program of Rostock University Medical Centre (889001 and 889003), the Josef and Käthe Klinz Foundation (T319/29737/2017), the DAMP Foundation, and the BMBF (VIP+ 00240). The small animal PET/CT was funded by the Deutsche Forschungsgemeinschaft (INST 2268/6-1 FUGG). The small animal MRI system was funded by the European Regional Development Fund (EFRE UHROM 16). C.I.L. was supported by the Clinician Scientist Program of the Rostock University Medical Center.

Conflicts of Interest: The authors declare no conflict of interest.

Abbreviations

CiC	cardiac induced cells
mESCs	murine embryonic stem cells
MI	myocardial infarction
EB	embryoid bodies
LAD	left anterior descending coronary artery
FOV	field of view
VOI	volumes of interest
CMR	cardiac magnetic resonance
LV	left ventricle
LVEF	left ventricular ejection fraction
SD	standard deviation
SEM	standard error of mean
MNC	mononuclear cell
KX	ketamine/xylazine
PET	positron emission tomography
CT	computerized tomography

References

1. Lee, W.W.; Marinelli, B.; van der Laan, A.M.; Sena, B.F.; Gorbatov, R.; Leuschner, F.; Dutta, P.; Iwamoto, Y.; Ueno, T.; Begieneman, M.P.V.; et al. PET/MRI of inflammation in myocardial infarction. *J. Am. Coll. Cardiol.* **2012**, *59*, 153–163. [CrossRef] [PubMed]
2. Van Hout, G.P.; Jansen of Lorkeers, S.J.; Wever, K.E.; Sena, E.S.; Kouwenberg, L.H.; van Solinge, W.W.; Macleod, M.R.; Doevendans, P.A.; Pasterkamp, G.; Chamuleau, S.A.J.; et al. Translational failure of anti-inflammatory compounds for myocardial infarction: A meta-analysis of large animal models. *Cardiovasc. Res.* **2016**, *109*, 240–248. [CrossRef] [PubMed]
3. Rischpler, C.; Dirschinger, R.J.; Nekolla, S.G.; Kossmann, H.; Nicolosi, S.; Hanus, F.; van Marwick, S.; Kunze, K.P.; Meinicke, A.; Götze, K.; et al. Prospective Evaluation of 18F-Fluorodeoxyglucose Uptake in Postischemic Myocardium by Simultaneous Positron Emission Tomography/Magnetic Resonance Imaging as a Prognostic Marker of Functional Outcome. *Circ. Cardiovasc. Imaging* **2016**, *9*, e004316. [CrossRef] [PubMed]
4. Thackeray, J.T.; Bankstahl, J.P.; Wang, Y.; Wollert, K.C.; Bengel, F.M. Clinically relevant strategies for lowering cardiomyocyte glucose uptake for 18F-FDG imaging of myocardial inflammation in mice. *Eur. J. Nucl. Med. Mol. Imaging* **2015**, *42*, 771–780. [CrossRef]
5. Thackeray, J.T.; Bankstahl, J.P.; Wang, Y.; Korf-Klingebiel, M.; Walte, A.; Wittneben, A.; Wollert, K.C.; Bengel, F.M. Targeting post-infarct inflammation by PET imaging: Comparison of (68)Ga-citrate and (68)Ga-DOTATATE with (18)F-FDG in a mouse model. *Eur. J. Nucl. Med. Mol. Imaging* **2015**, *42*, 317–327. [CrossRef]
6. Auerbach, W.; Dunmore, J.H.; Fairchild-Huntress, V.; Fang, Q.; Auerbach, A.B.; Huszar, D.; Joyner, A.L. Establishment and chimera analysis of 129/SvEv- and C57BL/6-derived mouse embryonic stem cell lines. *Biotechniques* **2000**, *29*, 1024–1028. [CrossRef]
7. Thiele, F.; Voelkner, C.; Krebs, V.; Muller, P.; Jung, J.J.; Rimmbach, C.; Steinhoff, G.; Noack, T.; David, R.; Lemcke, H. Nkx2.5 Based Ventricular Programming of Murine ESC-Derived Cardiomyocytes. *Cell. Physiol. Biochem.* **2019**, *53*, 337–354.
8. Cao, N.; Liu, Z.; Chen, Z.; Wang, J.; Chen, T.; Zhao, X.; Ma, Y.; Qin, L.; Kang, J.; Wei, B.; et al. Ascorbic acid enhances the cardiac differentiation of induced pluripotent stem cells through promoting the proliferation of cardiac progenitor cells. *Cell Res.* **2012**, *22*, 219–236. [CrossRef]
9. Rimmbach, C.; Jung, J.J.; David, R. Generation of murine cardiac pacemaker cell aggregates based on ES-cell-programming in combination with Myh6-promoter-selection. *J. Vis. Exp.* **2015**, e52465. [CrossRef]
10. Muller, P.; Gaebel, R.; Lemcke, H.; Wiekhorst, F.; Hausburg, F.; Lang, C.; Zarniko, N.; Westphal, B.; Steinhoff, G.; David, R.; et al. Intramyocardial fate and effect of iron nanoparticles co-injected with MACS((R)) purified stem cell products. *Biomaterials* **2017**, *135*, 74–84. [CrossRef]
11. Klopsch, C.; Gaebel, R.; Lemcke, H.; Beyer, M.; Vasudevan, P.; Fang, H.Y.; Quante, M.; Vollmar, B.; Skorska, A.; David, R.; et al. Vimentin-Induced Cardiac Mesenchymal Stem Cells Proliferate in the Acute Ischemic Myocardium. *Cells Tissues Organs* **2018**, *206*, 35–45. [CrossRef] [PubMed]
12. Bao, Q.; Newport, D.; Chen, M.; Stout, D.B.; Chatziioannou, A.F. Performance evaluation of the inveon dedicated PET preclinical tomograph based on the NEMA NU-4 standards. *J. Nucl. Med.* **2009**, *50*, 401–408. [CrossRef] [PubMed]
13. Lang, C.; Lehner, S.; Todica, A.; Boening, G.; Franz, W.M.; Bartenstein, P.; Hacker, M.; David, R. Positron emission tomography based in-vivo imaging of early phase stem cell retention after intramyocardial delivery in the mouse model. *Eur. J. Nucl. Med. Mol. Imaging* **2013**, *40*, 1730–1738. [CrossRef] [PubMed]
14. Heiberg, E.; Sjogren, J.; Ugander, M.; Carlsson, M.; Engblom, H.; Arheden, H. Design and validation of Segment—Freely available software for cardiovascular image analysis. *BMC Med. Imaging* **2010**, *10*, 1. [CrossRef]
15. Aurora, A.B.; Olson, E.N. Immune modulation of stem cells and regeneration. *Cell Stem Cell* **2014**, *15*, 14–25. [CrossRef]
16. Ben-Mordechai, T.; Palevski, D.; Glucksam-Galnoy, Y.; Elron-Gross, I.; Margalit, R.; Leor, J. Targeting macrophage subsets for infarct repair. *J. Cardiovasc. Pharmacol. Ther.* **2015**, *20*, 36–51. [CrossRef]
17. Lavine, K.J.; Epelman, S.; Uchida, K.; Weber, K.J.; Nichols, C.G.; Schilling, J.D.; Ornitz, D.M.; Randolph, G.J.; Mann, D.L. Distinct macrophage lineages contribute to disparate patterns of cardiac recovery and remodeling in the neonatal and adult heart. *Proc. Natl. Acad. Sci. USA* **2014**, *111*, 16029–16034. [CrossRef]

18. Ben-Mordechai, T.; Holbova, R.; Landa-Rouben, N.; Harel-Adar, T.; Feinberg, M.S.; Abd Elrahman, I.; Blum, G.; Epstein, F.H.; Silman, Z.; Cohen, S.; et al. Macrophage subpopulations are essential for infarct repair with and without stem cell therapy. *J. Am. Coll. Cardiol.* **2013**, *62*, 1890–1901. [CrossRef]
19. Hasan, A.S.; Luo, L.; Yan, C.; Zhang, T.X.; Urata, Y.; Goto, S.; Mangoura, S.A.; Abdel-Raheem, M.H.; Zhang, S.; Li, T.-S. Cardiosphere-Derived Cells Facilitate Heart Repair by Modulating M1/M2 Macrophage Polarization and Neutrophil Recruitment. *PLoS ONE* **2016**, *11*, e0165255. [CrossRef]
20. Czapla, J.; Matuszczak, S.; Wisniewska, E.; Jarosz-Biej, M.; Smolarczyk, R.; Cichon, T.; Głowala-Kosińska, M.; Śliwka, J.; Garbacz, M.; Szczypior, M.; et al. Human Cardiac Mesenchymal Stromal Cells with CD105+CD34- Phenotype Enhance the Function of Post-Infarction Heart in Mice. *PLoS ONE* **2016**, *11*, e0158745. [CrossRef]
21. Lang, C.I.; Wolfien, M.; Langenbach, A.; Muller, P.; Wolkenhauer, O.; Yavari, A.; Ince, H.; Steinhoff, G.; Krause, B.; David, R.; et al. Cardiac Cell Therapies for the Treatment of Acute Myocardial Infarction: A Meta-Analysis from Mouse Studies. *Cell. Physiol. Biochem.* **2017**, *42*, 254–268. [CrossRef] [PubMed]
22. Sonnenberg, G.F.; Hepworth, M.R. Functional interactions between innate lymphoid cells and adaptive immunity. *Nat. Rev. Immunol.* **2019**, *19*, 599–613. [CrossRef] [PubMed]
23. Love, C.; Tomas, M.B.; Tronco, G.G.; Palestro, C.J. FDG PET of infection and inflammation. *Radiographics* **2005**, *25*, 1357–1368. [CrossRef] [PubMed]
24. Peterson, L.R.; Gropler, R.J. Radionuclide imaging of myocardial metabolism. *Circ. Cardiovasc. Imaging* **2010**, *3*, 211–222. [CrossRef]
25. Saha, J.K.; Xia, J.; Grondin, J.M.; Engle, S.K.; Jakubowski, J.A. Acute hyperglycemia induced by ketamine/xylazine anesthesia in rats: Mechanisms and implications for preclinical models. *Exp. Biol. Med. (Maywood)* **2005**, *230*, 777–784. [CrossRef]
26. Ahmed, N.; Kansara, M.; Berridge, M.V. Acute regulation of glucose transport in a monocyte-macrophage cell line: Glut-3 affinity for glucose is enhanced during the respiratory burst. *Biochem. J.* **1997**, *327 Pt 2*, 369–375. [CrossRef]
27. Schatka, I.; Bengel, F.M. Advanced imaging of cardiac sarcoidosis. *J. Nucl. Med.* **2014**, *55*, 99–106. [CrossRef]

cells MDPI

Article

[68Ga]-NODAGA-RGD Positron Emission Tomography (PET) for Assessment of Post Myocardial Infarction Angiogenesis as a Predictor for Left Ventricular Remodeling in Mice after Cardiac Stem Cell Therapy

Cajetan Immanuel Lang [1], Piet Döring [2,3], Ralf Gäbel [2,4], Praveen Vasudevan [2,4], Heiko Lemcke [2,4], Paula Müller [2,4], Jan Stenzel [5], Tobias Lindner [5], Markus Joksch [5], Jens Kurth [3], Carina Bergner [3], Hans-Jürgen Wester [6], Hüseyin Ince [1], Gustav Steinhoff [2,4], Brigitte Vollmar [7], Robert David [2,4,*], and Bernd Joachim Krause [3]

[1] Department of Cardiology, Rostock University Medical Center, 18057 Rostock, Germany; Cajetan.Lang@med.uni-rostock.de (C.I.L.); Hueseyin.Ince@med.uni-rostock.de (H.I.)
[2] Department of Cardiac Surgery, Rostock University Medical Center, 18057 Rostock, Germany; Piet.Doering@uni-rostock.de (P.D.); Ralf.Gaebel@med.uni-rostock.de (R.G.); Praveen.Vasudevan@med.uni-rostock.de (P.V.); Heiko.Lemcke@med.uni-rostock.de (H.L.); Paula.Mueller@uni-rostock.de (P.M.); Gustav.Steinhoff@med.uni-rostock.de (G.S.)
[3] Department of Nuclear Medicine, Rostock University Medical Center, 18057 Rostock, Germany; Jens.Kurth@med.uni-rostock.de (J.K.); Carina.Bergner@med.uni-rostock.de (C.B.); Bernd.Krause@med.uni-rostock.de (B.J.K.)
[4] Department of Life, Light and Matter, Rostock, University of Rostock, 18057 Rostock, Germany
[5] Core Facility Multimodal Small Animal Imaging, University Medical Center, 18057 Rostock, Germany; Jan.Stenzel@med.uni-rostock.de (J.S.); Tobias.Lindner@med.uni-rostock.de (T.L.); Markus.Joksch@med.uni-rostock.de (M.J.)
[6] Pharmaceutical Radiochemistry, Technische Universität München, 85748 Garching, Germany; H.J.Wester@tum.de
[7] Rudolf-Zenker-Institute for Experimental Surgery, Rostock University Medical Center, 18057 Rostock, Germany; Brigitte.Vollmar@med.uni-rostock.de
* Correspondence: Robert.David@med.uni-rostock.de

Received: 31 March 2020; Accepted: 27 May 2020; Published: 30 May 2020

Abstract: Angiogenesis plays a central role in the healing process following acute myocardial infarction. The PET tracer [68Ga]-NODAGA-RGD, which is a ligand for the $\alpha_v\beta_3$ integrin, has been investigated for imaging angiogenesis in the process of healing myocardium in both animal and clinical studies. It´s value as a prognostic marker of functional outcome remains unclear. Therefore, the aim of this work was to establish [68Ga]-NODAGA-RGD for imaging angiogenesis in the murine infarct model and evaluate the tracer as a predictor for cardiac remodeling in the context of cardiac stem cell therapy. [68Ga]-NODAGA-RGD PET performed seven days after left anterior descending coronary artery (LAD) occlusion in 129S6 mice showed intense tracer accumulation within the infarct region. The specificity was shown in a sub-group of animals by application of the competitive inhibitor cilengitide prior to tracer injection in a subgroup of animals. Myocardial infarction (MI) significantly reduced cardiac function and resulted in pronounced left ventricular remodeling after three weeks, as measured by cardiac MRI in a separate group. Cardiac induced cells (CiC) that were derived from mESC injected intramyocardially in the therapy group significantly improved left ventricular ejection fraction (LVEF). Surprisingly, CiC transplantation resulted in significantly lower tracer accumulation seven days after MI induction. Accordingly, we successfully established the PET tracer [68Ga]-NODAGA-RGD for the assessment of $\alpha_v\beta_3$ integrin expression in the healing process after MI in the mouse model. Yet, our results indicate that the mere extent of angiogenesis following MI does not serve as a sufficient prognostic marker for functional outcome.

Keywords: angiogenesis; myocardial infarction; [^{68}Ga]-NODAGA-RGD; $\alpha_v\beta_3$-integrin; cardiac induced cells

---

1. Introduction

Acute myocardial infarction (MI) is a leading cause of death in most developed countries and is mostly induced by the occlusion of a coronary artery. Early revascularization reduces infarct size and improves the prognosis of MI patients [1]. Yet, the remaining damage causes pathological remodeling of the myocardium and it can potentially result in congestive heart failure. Myocardial healing following the ischemic event is a highly dynamic and complex process, which can be divided into three distinct phases [2]. The early inflammatory phase is dominated by infiltrating leucocytes scavenging the wound of necrotic tissue. A wound containing fibroblasts, macrophages, and a rich vascular network is formed at the next stage. Fibroblasts differentiate into myofibroblasts and deposit a provisional extracellular matrix, which is rich in fibrin and fibronectin. This proliferative phase is highly energy demanding and it depends on effective angiogenesis, a process that is defined as sprouting of pre-existing post-capillary venules into the provisional extracellular matrix. Eventually, myofibroblasts undergo apoptosis, microvessels regress, and a collagen-rich mature scar replaces the metabolically active immature scar [2].

Angiogenesis, being both an integral and an indispensable part of the wound healing [3], has been shown to be essential for myocardial regeneration after MI [4]. Where the inhibition of angiogenesis promotes heart failure in a murine model of cardiac hypertrophy [5], the induction of angiogenesis by cardiac stem cell therapies has been suggested by many researchers to preserve cardiac function following myocardial infarction in both small and large animals [6].

Despite these promising findings of proangiogenic therapeutic approaches in preclinical models, the results from clinical trials have been disappointing. Unfortunately, the reason for this remains unexplained, as only functional effects (such as LVEF and NYHA classification) of novel therapies can be assessed in patients. The underlying suggested biological mechanism—angiogenesis—is not amenable to established clinical diagnostic methods. The urgent need for non-invasive assessment of angiogenesis has inspired the field of molecular imaging to develop novel tracers that target the process of post-infarction angiogenesis. Thereby, the majority of single photon emission tomography (SPECT) and positron emission tomography (PET) tracers have been designed for binding to the $\alpha_v\beta_3$-integrin via the amino acid sequence RGD [7]. This integrin represents a vitronectin receptor, which is highly expressed at the tips of capillaries sprouting into the provisional matrix of granulation tissue [3,8–10]. Accordingly, imaging myocardial angiogenesis following ischemic damage has been successfully established with different tracers for various animal models in the preclinical setting at the level of qualitative and visual assessment of $\alpha_v\beta_3$-integrin expression [11,12].

Surprisingly, in animals, there is only one study correlating focal accumulation of [^{18}F]-galacto-RGD with infarct size [12], and another single study correlates the amount of tracer uptake with angiogenesis following stem cell therapy [13]. Furthermore, PET based imaging for the mouse model is not available to date, despite its unique features for basic research.

We have recently introduced a therapeutic approach for myocardial repair that is based on the transplantation of cardiac induced cells (CiC). These cells are derived from murine embryonic stem cells, exhibit an expression profile of cardiac marker genes, beat robustly, and improve cardiac function when transplanted after myocardial infarction in mice. Cell therapy also changed the inflammatory profile, as assessed by [^{18}F]-FDG PET [14]. Thus, we hypothesized that CiC transplantation modulates angiogenesis in the process of post-ischemic myocardial healing and chose this therapeutic approach for evaluating [^{68}Ga]-NODAGA-RGD PET for imaging angiogenesis and its modulation in a murine model of myocardial infarction.

Therefore the goal of the preset study was to:

1. establish the PET Tracer [^{68}Ga]-NODAGA-RGD for imaging angiogenesis in a murine model of myocardial infarction;
2. assess the effect of CiC transplantation on LV-remodeling post infarction measured by cardiac MRI (CMR); and,
3. evaluate whether $\alpha_v\beta_3$-integrin expression in the infarct, as measured by [^{68}Ga]-NODAGA-RGD-PET, predicts cardiac function following cell therapy.

2. Materials and Methods

2.1. Stem Cell Culture and Cardiovascular Differentiation

In order to avoid immune rejection of the transplanted cells W4 murine embryonic stem cells (mESCs), originally isolated from the 129S6 mouse strain [15], were used for syngeneic transplantation into 129S6/SvEvTac mice. The cells were grown in DMEM supplemented with 15% FBS Superior (Biochrom AG, Berlin, Germany), 1% Cell Shield® (Minerva Biolabs GmbH, Berlin, Germany), 100 µM non-essential amino acids, 1000 U/mL leukemia inhibitory factor (Phoenix Europe GmbH, Germany), and 100 µM β-mercaptoethanol (Sigma–Aldrich GmbH, Taufkirchen, Germany) at 37 °C, 5% CO_2, and 20% O_2, according to established protocols in our laboratory [16]. We initiated cardiovascular differentiation by the use of cardiogenic differentiation medium, containing IBM (Iscove's Basal Medium, Biochrom AG, Berlin, Germany) supplemented with 10% FBS Superior, 1% Cell Shield®, 100 µM non-essential amino acids, 450 µm 1-thioglycerol (Sigma–Aldrich GmbH), and 213 µg/mL ascorbic acid (Sigma–Aldrich GmbH), as described previously [16]. Thereby, differentiation was initiated by hanging-drop culture for two days at 37 °C, 5% CO_2, and 20% O_2. We started the formation of embryoid bodies (EB) by plating 400 cells per drop on the cover of a square petri dish. After two days of hanging-drop culture, EB were grown for an additional four days in suspension culture [17], and then harvested for transplantation. In the following we will refer to these cells as cardiac induced cells (CiC), which we characterized in detail in a previous work [14].

2.2. Animal Model

The federal animal care committee of the Landesamt für Landwirtschaft, Lebensmittelsicherheit und Fischerei Mecklenburg-Vorpommern (LALLF, Rostock, Germany) approved all animal experiments performed in this study (registration no. LALLF M-V/TSD/7221.3-1.1-054/15). For syngeneic transplantation, we used 129S6/SvEvTac mice, which were bred and maintained in the animal facility of the Rostock University Medical Center, as described previously [14]. Acute myocardial infarction was induced by surgical ligation of the left anterior descending coronary artery (LAD) following thoracotomy. Intramyocardial injections were performed immediately after MI induction, as described before [18]. The MI group received an intramyocardial injection of 10 µL PBS mixed with 10 µL Growth Factor Reduced Matrigel™ Matrix (Corning, Berlin, Germany). The MIC group received a suspension of 1 x 10^6 CiC in PBS (10µL) mixed with 10 µL matrigel. Injections of 4 x 5 µL were given along the infarct border. The site of injection was visually controlled at the time of transplantation.

The mice were divided into four groups for [^{68}Ga]-NODAGA-RGD imaging seven days following MI:

1) SHAM (n = 6)
2) MI (n = 6)
3) MI + blocked (n = 3)
4) MIC (n = 5)

Cardiac function was assessed in separate groups three weeks following MI by cardiac MRI:

5) MI only (n = 6)
6) MIC (n = 6)

2.3. PET Imaging

Mice were anaesthetized by the inhalation of isoflurane (4% for induction and 1–2.5% maintenance during preparation and scanning) for the PET study. We performed all PET/CT scans on a small animal PET/CT scanner (Inveon MM-PET/CT, Siemens Medical Solutions, Knoxville, TN, USA), according a standard protocol. Prior to the scan, the mice were injected intravenously with a dose of approximately 15–20 MBq [^{68}Ga]-NODGAGA-RGD via a custom-made micro catheter placed in a tail vein. After an uptake period of 30 min., static images were acquired in prone position for 45 min. The respiration of the mice was controlled and core body temperature was constantly kept at 38° C via a heating pad during the PET scan. Whole body CT scans were acquired for attenuation correction and anatomical land marking. The PET data sets were corrected for random coincidences, dead time, scatter, and attenuation. The reconstruction of the PET images was performed with the three-dimensional (3-D) iterative ordered-subset expectation maximization reconstruction algorithm (3D-OSEM/OP-MAP) with the following parameters: four iterations (OSEM), 32 iterations (MAP), 1.7 mm target resolution, and 128 × 128 matrix size. The data were decay-corrected to the time of injection. Three mice were injected with a blocking dose of cilengitide (0.018 mg/g body weight) 10 minutes prior to the tracer injection in order to verify whether the tracers binds specifically to the RGD sequence [11].

2.4. PET Image Analysis

An Inveon Research Workplace (Siemens, Knoxville, TN, USA) was used for image analysis, as described previously [19]. The PET and CT images were fused by the use of an automated volumetric fusion algorithm and then verified by an experienced reader for perfect alignment. Consecutively, standardized representative volumes of interest (VOI) were manually placed into the infarcted region at the site of maximal focal tracer accumulation. A volume of 20 μL was chosen for the VOI, aiming at covering most the granulation tissue. Correct positioning of the VOI was visually verified in axial, coronal, and sagittal projection.

2.5. Cardiac Magnetic Resonance Imaging and Analysis

Cardiac magnetic resonance (CMR) measurements were performed on a seven-Tesla small animal MRI system (BioSpec 70/30, maximum gradient strength 440 mT/m, Bruker BioSpin Gmbh, Ettlingen, Germany) equipped with a 1H transmit volume coil (86 mm, volume resonator) and a two-by-two receive-only surface coil array (both Bruker BioSpin GmbH), as described previously [14]. Images for left ventricular ejection fraction (LVEF) measurements were acquired using a IntraGate gradient-echo cine sequences (Intragate Cine-FLASH) in six short-axis planes completely covering the left ventricle following the planning sequences for the axis view. Thereby, the acquisition parameters included: echo time (TE): 2.38 ms, repetition time (TR): 5.89 ms, flip angle: 15°, 14 frames per cardiac cycle, oversampling: 140, averages: 1, field of view (FOV): 29.4 × 25.2 mm, matrix size: 211 × 180, resolution in-plane: 0.14 × 0.14 mm, slice thickness: 1 mm, scan time per slice: 2 minutes (Figure 1). Cardiac function and morphology were assessed from the cine sequences while using the freely available software Segment v2.0 R5165 (http://segment.heiberg.se) [20], as described previously [14].

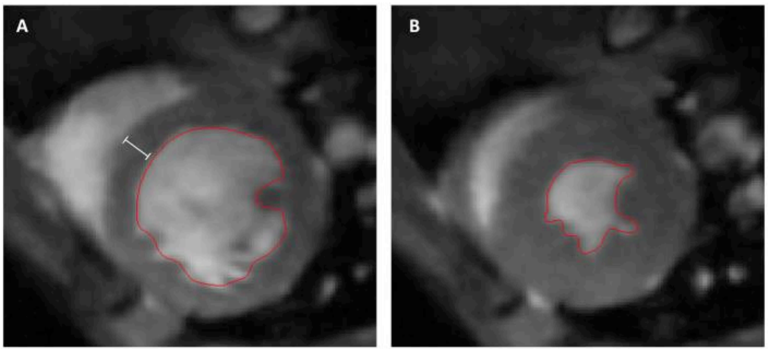

Figure 1. Representative short-axis slices of the left ventricle. The endocardium is marked with a red line for volumetric assessment of the left ventricle. (**A**) end-diastolic image; the white bar represents the interventricular septal thickness (IVSd). (**B**) end-systolic image.

2.6. Histology

The mice were euthanized after the PET scan, hearts were removed, embedded in O.C.T.TM compound (Tissue-Tek®; Zoeterwoude, Netherlands), and snap-frozen in liquid nitrogen. For histological examination of the infarction area, the heart tissue was divided into four horizontal levels from the apex to the base. For the discrimination of the scar from uninjured myocardium heart sections (5 μm) were stained with Sirius Red (Division Chroma, Muenster, Germany) and Fast Green FCF (Sigma–Aldrich), respectively. The infarct size and wall thickness were determined by the use of the Axio Vision LE Rel. 4.5 software (Carl Zeiss GmbH).

2.7. Tracer Preparation

[^{68}Ga]-NODAGA-RGD (Figure 2) was synthesized by means of a GRP module (Fa. Scintomics) while using a Ga peptide labeling kit (Sc-01, ABX, Radeberg) and 10 μg of NODAGA-RGD trifluoroacetate (9805, ABX, Radeberg). The sequence is carried out, as follows: the activity from the GalliaPharm generator (Eckert & Ziegler) was trapped on the included PS-H^+ cartridge, which was eluted into the reactor (preloaded with the NODAGA-RGD dissolved in 3 mL of 1.5 M HEPES) with a sodium chloride solution (1.5 mL, 5 M). The mixture was heated for 10 min. at 125 °C. Afterwards, the solution passed an ethanol-preconditioned Light C18 cartridge, whereby the product was trapped. After rinsing with water, the elution of the product was achieved with 4 mL of a 50% ethanol/water mixture. A 50% ethanol/water mixture replaced the PBS buffer of the kit, which normally fills up the product to an acceptable ethanol concentration. All solvents of the synthesis product were removed via evaporation in order to achieve an activity concentration of about 1 GBq/mL. The dried product was dissolved in 100 μL of a 0.9% sodium chloride solution (Fa. B. BRAUN, Melsungen). The molar activity after this preparation was in the range 20.4–38.1 MBq/nmol. The pH value of the final solution was 6. The activities were determined using a dose calibrator (MED Isomed 2010).

Analytical HPLC was performed using a CS MultoHigh 100 RP18 column (5 μm, 4 × 250 mm) on a Shimadzu HPLC pump and UV detector (220 nm) connected to a radiodetector. Mobile phase: A = water with 0.1% TFA, B = acetonitrile with 0.1% TFA, gradient: 0–0.5 min. 10% B, 0.5–7.0 min. 55% B, 7.0–30.0 min. 55% B. Flow rate 1 mL/min. Radiochemical identity and purity was verified via high performance liquid chromatography comparing the retention time of [^{68}Ga]-NODAGA-RGD (t_R = 8.4 min.) with those of [^{69}Ga]-NODAGA-RGD (9807, ABX, Radeberg, t_R = 8.4 min.).

Additionally, thin layer chromatography was performed on a Raytest miniGita Star while using iTLC SG paper (Agilent) and a mixture of NH_4OAc in water and methanol (1:1) as mobile phase. No free [^{68}Ga] could be observed.

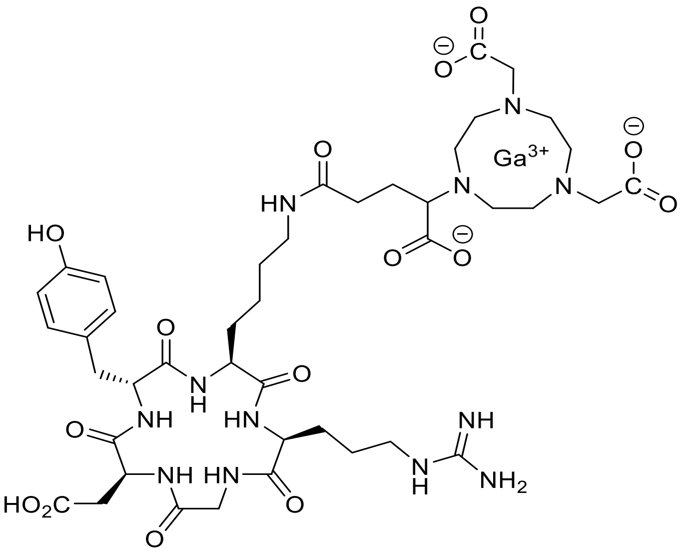

Figure 2. Structure of [^{68}Ga]-NODAGA-RGD.

2.8. Autoradiography

The excised hearts were frozen and embedded in O.C.T.TM Compound (Tissue-Tek®). Serial LV short-axis cryosections of 20-µm thickness were obtained. After quick air drying, the sections were exposed to an imaging plate (Dürr NDT Image Plate HR 20x25, Dürr Medical, Germany). Exposure with the samples was carried out overnight due to the limited quantum efficiency of the imaging plates at high energies (such as the 511 keV of PET radionuclides) [21]. Imaging plates were scanned with an image plate scanner (CR 35 BIO, Elysia-raytest GmbH, Germany; internal resolution of 30 µm), and the images were analyzed for background-corrected count densities with an image analysis program (AIDA Image Analyzer, Elysia-raytest GmbH, Straubenhardt, Germany).

2.9. Statistics

All of the data in this manuscript are presented as mean values ± standard deviation (SD). Student's t-test was used for statistical analysis of parametric data. The Mann–Whitney test was used for analysis of nonparametric data. Values of p <0.05 were considered to be statistically significant.

3. Results

3.1. PET- Imaging of $\alpha_v\beta_3$-Integrin after Myocardial Infarction

The expression of $\alpha_v\beta_3$-integrin has been shown in both rats and pigs to be an appropriate surrogate marker for imaging angiogenesis during the healing process of myocardial infarction [10,12]. Yet, a PET tracer for the mouse model is still greatly lacking. Therefore, we assessed [^{68}Ga]-NODAGA-RGD for $\alpha_v\beta_3$-integrin imaging in the mouse model seven days after induction of acute myocardial infarction. The MI animals show significantly higher focal tracer accumulation in the infarct region as compared to the SHAM group (1.51 ± 0.36% ID/g vs. 0.72 ± 0.24% ID/g; $p < 0.005$) (Figure 3D). We injected the competitive inhibitor cilengitide 10 min. prior to the application of the tracer in a subgroup of three animals, which suppressed the uptake of [^{68}Ga]-NODAGA-RGD to the level the SHAM group in order to assess the specificity of the tracer (0.79 ± 0.14% ID/g vs. 0.72 ± 0.24% ID/g; $p = 0.71$) (Figure 3D). Tracer accumulation within the granulation tissue of the scar was verified by autoradiography (Figure 3B).

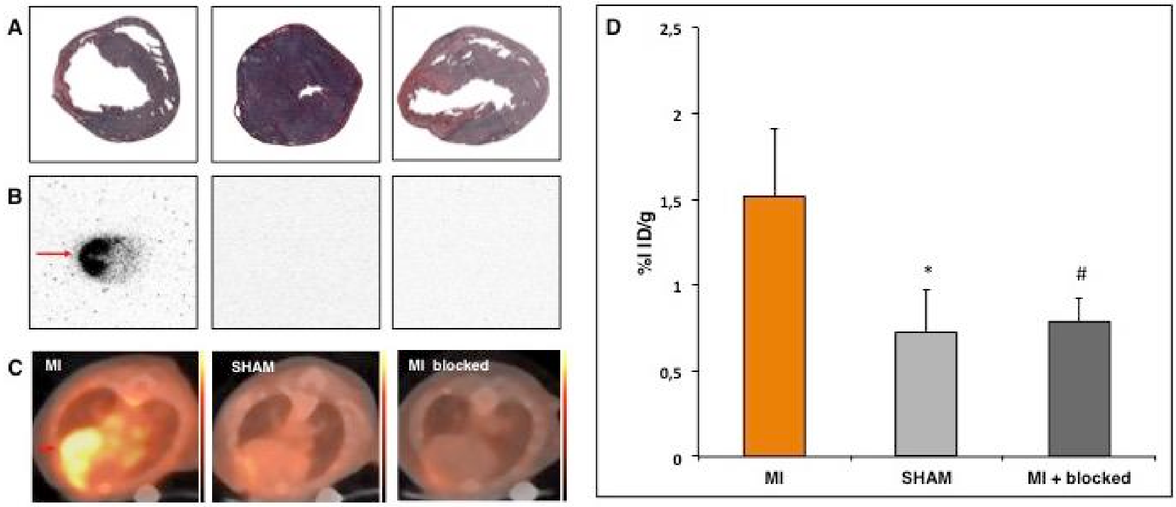

Figure 3. [^{68}Ga]-NODAGA-RGD positron emission tomography (PET) seven days after surgical induction of myocardial infarction shows enhanced focal tracer accumulation within the granulation tissue of the infarct scar. (**A**,**B**) Autoradiograms and Sirius Red stainings of adjacent myocardial cross sections. Highest tracer accumulation was detected in the scar area (red arrow), injection of cilengitide 10 minutes prior to tracer application reduced focal activity to SHAM level. (**C**) Axial PET/CT showing high focal uptake of [^{68}Ga]-NODAGA-RGD with in the scar, which is suppressed to SHAM level by cilengitide application. Color bars: 0 to 160 kBq/mL (MI) and 0 to 130 kBq (SHAM and myocardial infarction (MI) blocked). (**D**) %ID/g was measured by positioning a VOI of 20 μL into the brightest area within the scar. * $p < 0.005$ vs. MI; # $p < 0.05$ vs. MI**.**

3.2. Assessment of Left Ventricular Remodeling Following AMI by the Use of MRI

Cardiac morphology and function were measured by the use of magnetic resonance imaging three weeks following myocardial infarction. When compared to healthy mice, the MI group exhibited the distinctive MI induced changes (Figure 4). MI induced extensive apical and anterolateral scar formation with development of apical aneurysms (Figure 5). The dilation of the left ventricle resulted in dramatically increased volume of the left ventricle. EDV (49.2 ± 5.0 μL vs. 116.1 ± 39.0 μL; $p < 0.005$) and ESV (21.7 ± 1.9 μL vs. 90.7 ± 38.7 μL; $p < 0.005$) were both significantly increased. Left ventricular remodeling resulted in a significantly reduced LVEF (55.9 ± 3.1% vs. 23.3 ± 5.3%; $p < 0.001$). Furthermore left ventricular hypertrophy could be detected (IVSd: 0.66 ± 0.05 mm vs. 0.84 ± 0.05 mm; $p < 0.001$) as a compensatory mechanism, resulting in preserved stroke volume (SV: 27.5 ± 4.0 μL vs. 25.3 ± 4.2 μL; $p = 0.3$).

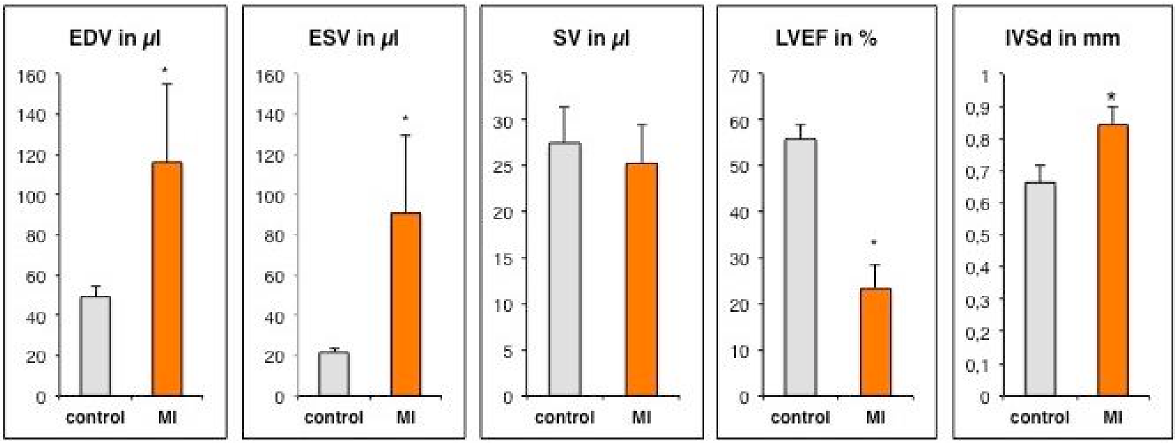

Figure 4. Functional and morphological parameters obtained from cardiac magnetic resonance (CMR) imaging. EDV: enddiastolic volume, ESV: endsystolic volume, SV: stroke volume, LVEF: left ventricular ejection fraction, IVSd: diastolic interventricular wallthickness. Data are presented as

mean with SD. * $p < 0.05$ compared to control group. EDV: end-diastolic volume; ESV: end-systolic volume; SV: stroke volume (EDV-ESV); LVEF: left ventricular ejection fraction (EDV-ESV/EDV*100%); IVSd (diastolic interventricular septal thickness).

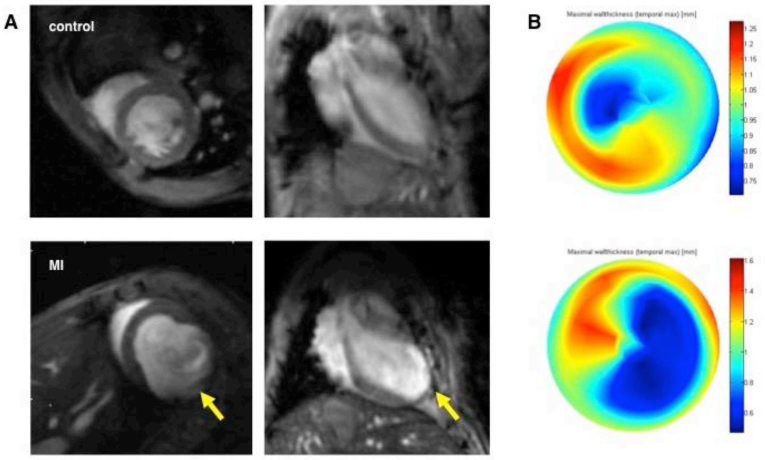

Figure 5. CMR images of representative healthy (upper row) and infarcted animals three weeks after MI (lower row) (**A**) left ventricular (LV) dilation, aneurysm formation in the thinned anteroseptal wall (yellow arrow) and LV hypertrophy can be observed. (**B**) bullseye plots depicting the maximal wall thickness of the left ventricle visualize the thinning of the apex and the anteroseptal wall.

3.3. Effect of Cell Therapy on Cardiac Remodeling Following AMI

Cardiac induced Cells (CiC) were generated, as described previously [14], and injected into the border zone of the infarction after surgical occlusion of the LAD. CMR performed after three weeks showed reduced LV-remodeling resulting in preserved cardiac function as compared to the MI group (Figure 6). Left ventricular dilation was reduced, but it did not reach statistical significance (EDV: 103.6 ± 15.7 µL vs. 116.1 ± 39.0 µL; $p = 0.44$ and ESV: 72.8 ± 15.6 µL vs. 90.7 ± 38.7 µL; $p = 0.28$). CiC therapy resulted in significantly improved functional parameters (LVEF: 30.0 ± 5.0% vs. 23.3 ± 5.3%; $p < 0.05$ and SV: 30.6 ± 3.6 µL vs. 25.3 ± 4.2 µL; $p < 0.05$). Moreover, a trend of more pronounced LV hypertrophy was observed (IVSd: 0.9 ± 0.2 mm vs. 0.84 ± 0.05 mm; $p = 0.4$).

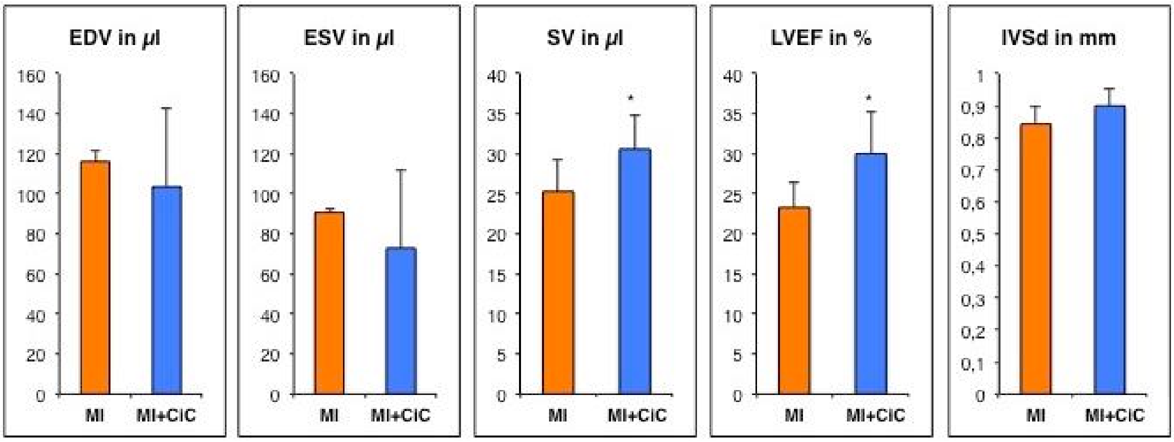

Figure 6. Effect of cardiac induced cells (CiC) transplantation on cardiac function and morphology measured by CMR three weeks after MI induction. Values are mean with SD. * $p < 0.05$ compared to MI group.

3.4. Effect of CiC Transplantation on Angiogenesis and Correlation with LV-Remodelling

We established $\alpha_v\beta_3$-integrin imaging by the use of [^{68}Ga] -NODAGA-RGD PET for detecting the angiogenic response following acute myocardial infarction, as described above. Furthermore, MRI had revealed significant improvement of cardiac function after CiC therapy. We hypothesized that CiC transplantation results in elevated levels of $\alpha_v\beta_3$-integrin expression within the myocardium, as increased neovessel formation has been shown to reduce cardiac remodeling [22].

Yet, intriguingly, [^{68}Ga]-NODAGA-RGD accumulation within the infarct zone was significantly reduced by CiC transplantation when compared to the MI group (1.5 ± 0.4% ID/g vs. 1.0 ± 0.1% ID/g; $p < 0.05$; Figure 7). We wondered whether the observed $\alpha_v\beta_3$-integrin expression correlates with differences in scar size or wall thickness. Yet, we did not find any difference between MIC and MI group based on histological findings (Figure 8). In a previous study, we examined the effect of CiC transplantation on the myocardial inflammation five days after infarct induction [14]. CiC transplantation lead to distinct changes of the inflammatory profile on a cellular level, suggesting changes in the dynamics of infarct healing.

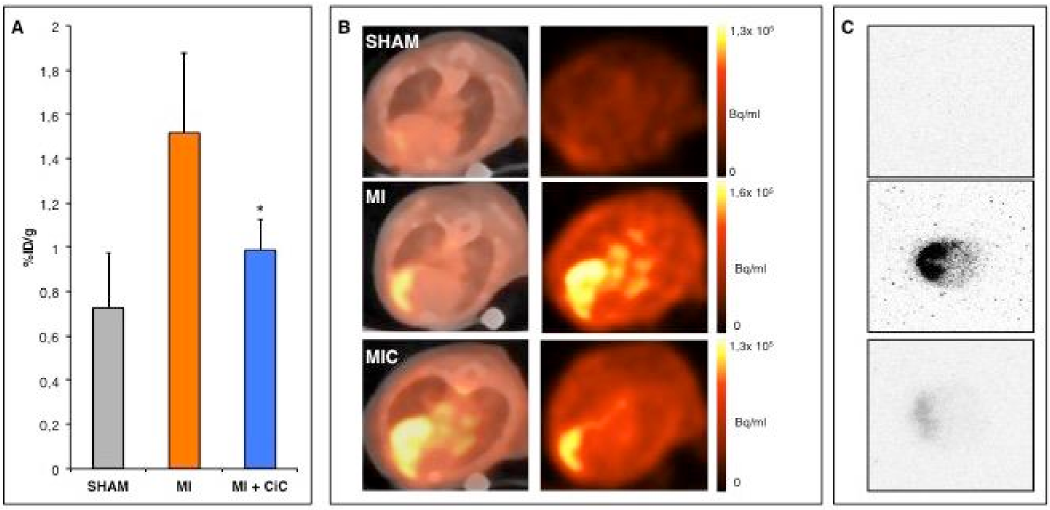

Figure 7. (**A**) Transplantation of CiC significantly reduces uptake of [^{68}Ga]-NODAGA-RDG in the infarct region. * $p < 0.05$ compared to the MI group. (**B**) Representative axial images of the respective group: PET/CT fusion images on the left, PET images on the right. Tracer accumulation can be clearly allocated to the infarct region. (**C**) Focal tracer accumulation is located in the infarct region as shown in representative images from autoradiography.

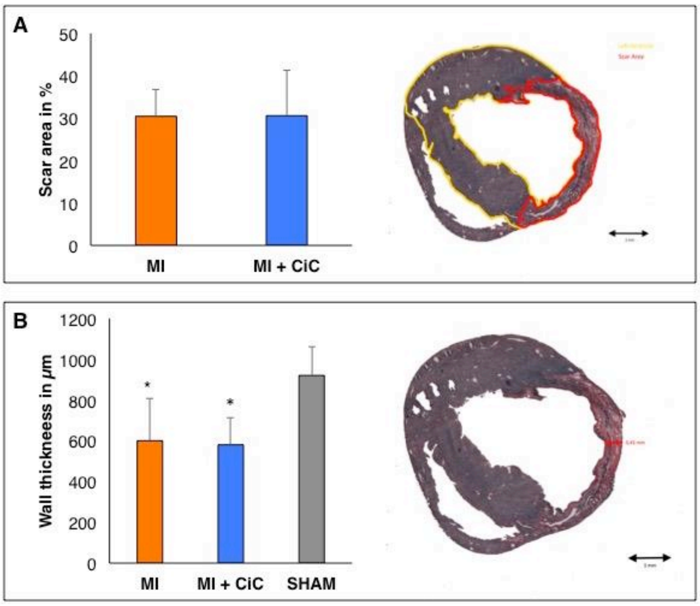

Figure 8. Heart sections of four horizontal infarction levels (5 µm) stained with Sirius Red (collagen) and Fast Green (non-infarcted myocardium). Right side: Representative sections of the MI group showing measurements of (**A**) scar size and (**B**) wall thickness of the infarcted region. * $p < 0.05$ compared to SHAM group.

4. Discussion

Our study is the first to image angiogenesis based on a $\alpha_v\beta_3$-integrin targeted PET tracer in a mouse model of acute myocardial infarction. The $\alpha_v\beta_3$-integrin is highly expressed at the tips of capillaries sprouting into the provisional matrix of granulation tissue [8,23]. Therefore, it represents the most commonly used molecular target in the development of PET tracers for imaging angiogenesis [24]. [^{18}F]-Galacto-RGD was introduced in 2001 by Haubner et al. for non-invasive imaging of $\alpha_v\beta_3$-integrin expression in tumor mouse models [25], and it was rapidly translated into clinical evaluation in cancer patients [26]. Moreover, it was demonstrated that [^{18}F]-Galacto-RGD imaging is sensitive enough to visualize $\alpha_v\beta_3$-expression resulting exclusively from the tumor vasculature [26]. Hence, it was studied to monitor $\alpha_v\beta_3$-integrin expression following acute myocardial infarction in a rat model [27]. The accumulation of [^{18}18]-Galacto-RGD within the infarcted area peaked seven days post MI, correlated strongly with newly formed vessels and it could be blocked by a competitive inhibitor, which suggests the successful imaging of angiogenesis in the process of myocardial healing [27]. Various independent research groups were able to validate the concept of $\alpha_v\beta_3$-integrin imaging—with both SPECT and PET tracers—as a surrogate marker for angiogenesis in the healing process of ischemically damaged myocardium [13,28,29] and skeletal muscle [30,31].

The multi-step synthesis of [^{18}F]-Galacto-RGD is time consuming and it requires an on-site cyclotron, making an automated production process extremely difficult [11,24]. The search for alternative RGD compounds resulted in the development of [^{68}Ga]-NODAGA-RGD, which has similar characteristics to [^{18}F]-Galacto-RGD, making it an ideal candidate for small animal applications [11,24]. [^{68}Ga] tracers have the advantage of easy and fast production with a generator-produced radionuclide [24]. Furthermore, both precursor and the non-radioactive standard are commercially available in cGMP quality [32], endowing [^{68}Ga]-NODAGA-RGD with optimal features for potential clinical translation.

We aimed at establishing [^{68}Ga]-NODAGA-RGD based imaging of angiogenesis in a murine model of myocardial infarction against the background that imaging $\alpha_v\beta_3$-integrin expression following myocardial infarction has already been evaluated in rats. Based on findings from Murry´s group, that formation of granulation tissue and the vascularization of the wound peak seven days after surgical LAD occlusion in mice [33], we chose this time point for [^{68}Ga]-NODAGA-RGD imaging. We detected significantly increased tracer accumulation in the infarct area seven days after surgical induction of MI when compared to SHAM operated animals. The exact localization within granulation tissue of the infarct could be verified by autoradiography. The specific binding of [^{68}Ga]-NODAGA-RGD to $\alpha_v\beta_3$-integrin was shown by blocking tracer accumulation down to SHAM levels with Cilengitide. These findings are well in line with previous SPECT studies in the mouse model, showing intense angiogenesis in the infarct region by the use of $\alpha_v\beta_3$-integrin targeted tracers - [^{111}In]-DTPA-cNGR [9] and [^{99m}Tc]-NC100692 [34] seven days after surgical LAD occlusion. Against this large body of evidence, we conclude that angiogenesis following MI can be visualized and measured by [^{68}Ga]-NODAGA-RGD PET in mice.

We then intended to test the hypothesis that [^{68}Ga]-NODAGA-RGD PET might be a valid tool for predicting cardiac remodeling following acute myocardial infarction, as stated by Schwaiger´s group [12]. Therefore, murine ES-derived cardiac induced cells (CiC) were transplanted following MI induction and CMR measured the effect on cardiac remodeling. We chose this cell preparation based on its ability to improve pump function when transplanted after acute myocardial infarction, as previously described by our group [14]. CiC transplantation induced a pronounced shift in the distribution pattern of inflammatory cells within the heart. Thereby, the amount of monocytes was decreased in favor of an increase of M1 and M2 macrophages in both the remote and infarct area of the myocardium. As macrophages play a central role in the process of myocardial healing and ventricular remodeling [35], we hypothesized that angiogenesis—an integral part of wound healing—would be significantly altered by CiC transplantation.

Cardiac remodeling was significantly reduced by CiC transplantation, resulting in significantly improved LVEF and SV, as measured by CMR three weeks following MI induction. The magnitude of LVEF improvement was in the expected range when compared to results from a meta-analysis performed by our group [36].

We measured [^{68}Ga]-NODAGA-RGD accumulation in the infarct area following CiC transplantation seven days post MI in order to evaluate the correlation between $\alpha_v\beta_3$-integrin expression and LV-remodeling. Surprisingly, cell therapy significantly reduced focal tracer accumulation in the infarct area. CMR showed reduced LV dilation, resulting in significantly increased stroke volume and LVEF in the cell therapy group. Hence, we reasoned that lower $\alpha_v\beta_3$-integrin expression in the infarct area might be a consequence of a mere reduction of myocardial damage caused by cell therapy. Yet, scar size and wall thickness of the infarct showed no difference between control and therapy group seven days post MI. The angiogenic response following MI and its therapeutic modulation is probably more complex than assumed by others and us. CiC transplantation significantly alters the cellular inflammatory response profile five days following acute MI, including a marked shift in monocyte and macrophage subpopulations, which play an important role in angiogenesis [37], as recently shown by our group [14]. CiC therapy seems to modify the complex process of myocardial healing, which leads to distinct changes of both inflammatory and angiogenic responses when compared on day five and day seven post MI. In the specific model used by us, both parameters are valid predictors for therapeutic efficacy of our cell therapy.

Yet, these findings and methods cannot be directly transferred to other mammals or therapeutic approaches targeting myocardial healing, as exemplified in the following paragraph.

Huang at al. transplanted cell aggregates consisting of human umbilical vein endothelial cells (HUVECs) and cord-blood mesenchymal stem cells (cbMSCs) into the peri-infarct zones in a rat model aiming at angiogenesis induction. Angiogenesis, as assessed by [^{68}Ga]-RDG PET, was significantly increased by cell transplantation five days post MI and associated with less cardiac remodeling and a better pump function [13]. They ascribe the increase of angiogenesis on day five to therapeutically induced angiogenesis, which then leads to recovery in blood perfusion.

Lindsey et al. examined the role of the extracellular matrix formation on angiogenesis [34]. Thereby, MMP-9 deletion improved left ventricular function following acute myocardial infarction in mice after seven days. This improvement was associated with an increase of $\alpha_v\beta_3$-integrin expression measured by NC100692 SPECT seven days post MI. Yet, the infarct size showed no significant difference on day seven, which is well in line with our findings.

Sherif et al. correlated heart morphology and angiogenesis of individual data sets of rats [12]. LV remodeling assessed 12 weeks after acute MI by CMR was associated with lower levels of $\alpha_v\beta_3$-integrin expression measured by [^{18}F]-galacto-RGD PET 7 days post MI.

A small clinical trial performed [^{18}F]-fluciclatide PET in Patients 14±7 days after presentation with acute ST-segment elevation MI. Cardiac function was assessed by CMR within seven days after PET. Tracer accumulation was not correlated with infarct size, but with functional recovery, suggesting that [^{18}F]-fluciclatide uptake is not a surrogate of infarction, but relates more to the tissue-healing response to injury [38].

The results from these studies seem to be relatively inconclusive. Yet, these data sets and especially the respective conclusions must be carefully interpreted, as the speed of myocardial healing differs considerably between species [33]. Hence, it is of utmost importance to understand what is actually being imaged via RGD-targeted tracers in the respective context. LAD ligation induces a massive wound, which is consecutively replaced by granulation tissue. In mice, the number of newly formed vessels in the infarct peaks seven days post MI, suggesting that $\alpha_v\beta_3$-integrin expression assessed by PET imaging reflects most of all capillaries sprouting in the freshly formed granulation tissue.

Murry´s group hypothesized that interventions that accelerate the formation of granulation tissue will reduce ventricular remodeling and, thus, decrease heart failure [33]. Vandervelde et al. compared the healing kinetics of infarcts caused by permanent versus transient occlusion of the LAD in mice [39]. Thereby, LV remodeling and the resulting LVEF impairment was significantly more severe in the permanent occlusion group and furthermore associated with prolonged myocardial healing. Minatoguchi et al. found intra-venous G-CSF application in a rabbit model of myocardial infarction to accelerate the healing process resulting in improved cardiac function and post MI LV—remodeling [40].

Hence, we think that therapies targeting the healing process after acute myocardial infarction are very likely to induce a shift in the speed of myocardial healing, which is specific for the respective therapeutic agent applied. Angiogenesis in the context of granulation tissue formation might peak earlier as a consequence. Therefore, comparisons of different therapeutic applications at the identical time point might be difficult, even in the same species. There are only few studies addressing the speed of healing as a predictor of myocardial regeneration, which suggests that further research in this field is of utmost importance.

Author Contributions: Conceptualization, C.I.L. and B.J.K.; methodology, T.L., J.S., J.K., M.J., C.B. and H.-J.W.; formal analysis, C.I.L. and P.D.; investigation, C.I.L., P.D., P.V., R.G., P.M., and H.L.; writing—original draft preparation, C.I.L.; writing—review and editing, J.K., R.D., G.S., H.I.; B.V. and B.J.K.; visualization, C.I.L. and P.D.; supervision, R.D. and B.J.K.; funding acquisition, C.I.L., R.D., B.V. and B.J.K. All authors have read and agreed to the published version of the manuscript.

Funding: This work is supported by the German Heart Research Foundation (F/34/15) and the FORUN Program of Rostock University Medical Centre (889066). The small animal PET/CT is funded by the Deutsche Forschungsgemeinschaft (INST 2268/6-1 FUGG). The small animal MRI system is funded by the European Regional Development Fund (EFRE UHROM 16). C.I.L. is supported by the Clinician Scientist Program of the Rostock University Medical Center. R.D. is supported by the EU structural Fund (ESF/14-BM-A55-0024/18). In addition, R.D and P.M are supported by the DFG (DA1296/6-1). R.D. is further supported by the DAMP foundation, the German Heart Foundation (F/01/12) and the BMBF (VIP+ 00240). In addition, H. L. is supported by the FORUN Program of Rostock University Medical Centre (889001 and 889003) and the Josef and Käthe Klinz Foundation (T319/29737/2017).

Conflicts of Interest: The authors declare no conflict of interest.

Abbreviations

LAD—left anterior descending coronary artery
MI—myocardial infarction
CiC—cardiac induced cells
mESCs—murine embryonic stem cells
EB—embryoid bodies
LVEF—left ventricular ejection fraction
LV—left ventricle
PET—positron emission tomography
SPECT—single photon emission tomography
CMR—Cardiac magnetic resonance
CT—computer tomography
VOI—volumes of interest
IVSd—diastolic interventricular septal thickness
SD—standard deviation
EDV—end-diastolic volume
ESV—end-systolic volume
SV—stroke volume

References

1. Keeley, E.C.; Boura, J.A.; Grines, C.L. Primary angioplasty versus intravenous thrombolytic therapy for acute myocardial infarction: A quantitative review of 23 randomised trials. *Lancet* **2003**, *361*, 13–20, doi:10.1016/S0140-6736(03)12113-7.
2. Frangogiannis, N.G. The mechanistic basis of infarct healing. *Antioxid. Redox Signal.* **2006**, *8*, 1907–1939, doi:10.1089/ars.2006.8.1907.

3. Tonnesen, M.G.; Feng, X.; Clark, R.A. Angiogenesis in wound healing. *J. Investig. Dermatol. Symp. Proc.* **2000**, *5*, 40–46, doi:10.1046/j.1087-0024.2000.00014.x.
4. Cochain, C.; Channon, K.M.; Silvestre, J.S. Angiogenesis in the infarcted myocardium. *Antioxid. Redox Signal.* **2013**, *18*, 1100–1113, doi:10.1089/ars.2012.4849.
5. Shiojima, I.; Sato, K.; Izumiya, Y.; Schiekofer, S.; Ito, M.; Liao, R.; Colucci, W.S.; Walsh, K. Disruption of coordinated cardiac hypertrophy and angiogenesis contributes to the transition to heart failure. *J. Clin. Invest* **2005**, *115*, 2108–2118, doi:10.1172/JCI24682.
6. van der Laan, A.M.; Piek, J.J.; van Royen, N. Targeting angiogenesis to restore the microcirculation after reperfused MI. *Nat. Rev. Cardiol.* **2009**, *6*, 515–523, doi:10.1038/nrcardio.2009.103.
7. Mandic, L.; Traxler, D.; Gugerell, A.; Zlabinger, K.; Lukovic, D.; Pavo, N.; Goliasch, G.; Spannbauer, A.; Winkler, J.; Gyongyosi, M. Molecular Imaging of Angiogenesis in Cardiac Regeneration. *Curr. Cardiovasc. Imaging Rep.* **2016**, *9*, 27, doi:10.1007/s12410-016-9389-6.
8. Hodivala-Dilke, K. $\alpha_v\beta_3$ integrin and angiogenesis: A moody integrin in a changing environment. *Curr. Opin. Cell Biol.* **2008**, *20*, 514–519, doi:10.1016/j.ceb.2008.06.007.
9. Hendrikx, G.; De Saint-Hubert, M.; Dijkgraaf, I.; Bauwens, M.; Douma, K.; Wierts, R.; Pooters, I.; Van den Akker, N.M.; Hackeng, T.M.; Post, M.J.; et al. Molecular imaging of angiogenesis after myocardial infarction by (111)In-DTPA-cNGR and (99m)Tc-sestamibi dual-isotope myocardial SPECT. *EJNMMI Res.* **2015**, *5*, 2, doi:10.1186/s13550-015-0081-7.
10. Gronman, M.; Tarkia, M.; Kiviniemi, T.; Halonen, P.; Kuivanen, A.; Savunen, T.; Tolvanen, T.; Teuho, J.; Kakela, M.; Metsala, O.; et al. Imaging of $\alpha_v\beta_3$ integrin expression in experimental myocardial ischemia with [(68)Ga]NODAGA-RGD positron emission tomography. *J. Transl. Med.* **2017**, *15*, 144, doi:10.1186/s12967-017-1245-1.
11. Laitinen, I.; Notni, J.; Pohle, K.; Rudelius, M.; Farrell, E.; Nekolla, S.G.; Henriksen, G.; Neubauer, S.; Kessler, H.; Wester, H.J.; et al. Comparison of cyclic RGD peptides for $\alpha_v\beta_3$ integrin detection in a rat model of myocardial infarction. *EJNMMI Res.* **2013**, *3*, 38, doi:10.1186/2191-219X-3-38.
12. Sherif, H.M.; Saraste, A.; Nekolla, S.G.; Weidl, E.; Reder, S.; Tapfer, A.; Rudelius, M.; Higuchi, T.; Botnar, R.M.; Wester, H.J.; et al. Molecular imaging of early $\alpha_v\beta_3$ integrin expression predicts long-term left-ventricle remodeling after myocardial infarction in rats. *J. Nucl. Med.* **2012**, *53*, 318–323, doi:10.2967/jnumed.111.091652.
13. Huang, C.C.; Wei, H.J.; Lin, K.J.; Lin, W.W.; Wang, C.W.; Pan, W.Y.; Hwang, S.M.; Chang, Y.; Sung, H.W. Multimodality noninvasive imaging for assessing therapeutic effects of exogenously transplanted cell aggregates capable of angiogenesis on acute myocardial infarction. *Biomaterials* **2015**, *73*, 12–22, doi:10.1016/j.biomaterials.2015.09.009.
14. Vasudevan, P.; Gaebel, R.; Doering, P.; Mueller, P.; Lemcke, H.; Stenzel, J.; Lindner, T.; Kurth, J.; Steinhoff, G.; Vollmar, B.; et al. 18F-FDG PET-Based Imaging of Myocardial Inflammation Predicts a Functional Outcome Following Transplantation of mESC-Derived Cardiac Induced Cells in a Mouse Model of Myocardial Infarction. *Cells* **2019**, *8*, doi:10.3390/cells8121613.
15. Auerbach, W.; Dunmore, J.H.; Fairchild-Huntress, V.; Fang, Q.; Auerbach, A.B.; Huszar, D.; Joyner, A.L. Establishment and chimera analysis of 129/SvEv- and C57BL/6-derived mouse embryonic stem cell lines. *Biotechniques* **2000**, *29*, 1024–1028, 1030, 1032, doi:10.2144/00295st04.
16. Thiele, F.; Voelkner, C.; Krebs, V.; Muller, P.; Jung, J.J.; Rimmbach, C.; Steinhoff, G.; Noack, T.; David, R.; Lemcke, H. Nkx2.5 Based Ventricular Programming of Murine ESC-Derived Cardiomyocytes. *Cell. Physiol. Biochem.* **2019**, *53*, 337–354, doi:10.33594/000000142.
17. Rimmbach, C.; Jung, J.J.; David, R. Generation of murine cardiac pacemaker cell aggregates based on ES-cell-programming in combination with Myh6-promoter-selection. *J. Vis. Exp.* **2015**, 10.3791/52465, e52465, doi:10.3791/52465.
18. Muller, P.; Gaebel, R.; Lemcke, H.; Wiekhorst, F.; Hausburg, F.; Lang, C.; Zarniko, N.; Westphal, B.; Steinhoff, G.; David, R. Intramyocardial fate and effect of iron nanoparticles co-injected with MACS((R)) purified stem cell products. *Biomaterials* **2017**, *135*, 74–84, doi:10.1016/j.biomaterials.2017.05.002.
19. Lang, C.; Lehner, S.; Todica, A.; Boening, G.; Franz, W.M.; Bartenstein, P.; Hacker, M.; David, R. Positron emission tomography based in-vivo imaging of early phase stem cell retention after intramyocardial delivery in the mouse model. *Eur. J. Nucl. Med. Mol. Imaging* **2013**, *40*, 1730–1738, doi:10.1007/s00259-013-2480-1.

20. Heiberg, E.; Sjogren, J.; Ugander, M.; Carlsson, M.; Engblom, H.; Arheden, H. Design and validation of Segment--freely available software for cardiovascular image analysis. *BMC Med. Imaging* **2010**, *10*, 1, doi:10.1186/1471-2342-10-1.
21. Thoms, M. The quantum efficiency of radiographic imaging with image plates. *Nucl. Instrum. Methods Phys. Res.* **1996**, *378*, 598–611, doi:Doi 10.1016/0168-9002(96)00530-X.
22. Kobayashi, K.; Maeda, K.; Takefuji, M.; Kikuchi, R.; Morishita, Y.; Hirashima, M.; Murohara, T. Dynamics of angiogenesis in ischemic areas of the infarcted heart. *Sci. Rep.* **2017**, *7*, 7156, doi:10.1038/s41598-017-07524-x.
23. Hendrikx, G.; Voo, S.; Bauwens, M.; Post, M.J.; Mottaghy, F.M. SPECT and PET imaging of angiogenesis and arteriogenesis in pre-clinical models of myocardial ischemia and peripheral vascular disease. *Eur. J. Nucl. Med. Mol. Imaging* **2016**, *43*, 2433–2447, doi:10.1007/s00259-016-3480-8.
24. Knetsch, P.A.; Petrik, M.; Griessinger, C.M.; Rangger, C.; Fani, M.; Kesenheimer, C.; von Guggenberg, E.; Pichler, B.J.; Virgolini, I.; Decristoforo, C.; et al. [68Ga]NODAGA-RGD for imaging $\alpha_v\beta_3$ integrin expression. *Eur. J. Nucl. Med. Mol. Imaging* **2011**, *38*, 1303–1312, doi:10.1007/s00259-011-1778-0.
25. Haubner, R.; Wester, H.J.; Weber, W.A.; Mang, C.; Ziegler, S.I.; Goodman, S.L.; Senekowitsch-Schmidtke, R.; Kessler, H.; Schwaiger, M. Noninvasive imaging of $\alpha_v\beta_3$ integrin expression using 18F-labeled RGD-containing glycopeptide and positron emission tomography. *Cancer Res.* **2001**, *61*, 1781–1785.
26. Haubner, R.; Weber, W.A.; Beer, A.J.; Vabuliene, E.; Reim, D.; Sarbia, M.; Becker, K.F.; Goebel, M.; Hein, R.; Wester, H.J.; et al. Noninvasive visualization of the activated $\alpha_v\beta_3$ integrin in cancer patients by positron emission tomography and [18F]Galacto-RGD. *PLoS Med.* **2005**, *2*, e70, doi:10.1371/journal.pmed.0020070.
27. Higuchi, T.; Bengel, F.M.; Seidl, S.; Watzlowik, P.; Kessler, H.; Hegenloh, R.; Reder, S.; Nekolla, S.G.; Wester, H.J.; Schwaiger, M. Assessment of $\alpha_v\beta_3$ integrin expression after myocardial infarction by positron emission tomography. *Cardiovasc. Res.* **2008**, *78*, 395–403, doi:10.1093/cvr/cvn033.
28. Gao, H.; Lang, L.; Guo, N.; Cao, F.; Quan, Q.; Hu, S.; Kiesewetter, D.O.; Niu, G.; Chen, X. PET imaging of angiogenesis after myocardial infarction/reperfusion using a one-step labeled integrin-targeted tracer 18F-AlF-NOTA-PRGD2. *Eur. J. Nucl. Med. Mol. Imaging* **2012**, *39*, 683–692, doi:10.1007/s00259-011-2052-1.
29. Hedhli, J.; Czerwinski, A.; Schuelke, M.; Ploska, A.; Sowinski, P.; Hood, L.; Mamer, S.B.; Cole, J.A.; Czaplewska, P.; Banach, M.; et al. Synthesis, Chemical Characterization and Multiscale Biological Evaluation of a Dimeric-cRGD Peptide for Targeted Imaging of $\alpha_v\beta_3$ Integrin Activity. *Sci. Rep.* **2017**, *7*, 3185, doi:10.1038/s41598-017-03224-8.
30. Hua, J.; Dobrucki, L.W.; Sadeghi, M.M.; Zhang, J.; Bourke, B.N.; Cavaliere, P.; Song, J.; Chow, C.; Jahanshad, N.; van Royen, N.; et al. Noninvasive imaging of angiogenesis with a 99mTc-labeled peptide targeted at $\alpha_v\beta_3$ integrin after murine hindlimb ischemia. *Circulation* **2005**, *111*, 3255–3260, doi:10.1161/CIRCULATIONAHA.104.485029.
31. Hedhli, J.; Slania, S.L.L.; Ploska, A.; Czerwinski, A.; Konopka, C.J.; Wozniak, M.; Banach, M.; Dobrucki, I.T.; Kalinowski, L.; Dobrucki, L.W. Evaluation of a dimeric-cRGD peptide for targeted PET-CT imaging of peripheral angiogenesis in diabetic mice. *Sci. Rep.* **2018**, *8*, 5401, doi:10.1038/s41598-018-23372-9.
32. Pohle, K.; Notni, J.; Bussemer, J.; Kessler, H.; Schwaiger, M.; Beer, A.J. 68Ga-NODAGA-RGD is a suitable substitute for (18)F-Galacto-RGD and can be produced with high specific activity in a cGMP/GRP compliant automated process. *Nucl. Med. Biol.* **2012**, *39*, 777–784, doi:10.1016/j.nucmedbio.2012.02.006.
33. Virag, J.I.; Murry, C.E. Myofibroblast and endothelial cell proliferation during murine myocardial infarct repair. *Am. J. Pathol.* **2003**, *163*, 2433–2440, doi:10.1016/S0002-9440(10)63598-5.
34. Lindsey, M.L.; Escobar, G.P.; Dobrucki, L.W.; Goshorn, D.K.; Bouges, S.; Mingoia, J.T.; McClister, D.M., Jr.; Su, H.; Gannon, J.; MacGillivray, C.; et al. Matrix metalloproteinase-9 gene deletion facilitates angiogenesis after myocardial infarction. *Am. J. Physiol. Heart Circ. Physiol.* **2006**, *290*, H232–H239, doi:10.1152/ajpheart.00457.2005.
35. Chen, B.; Frangogiannis, N.G. Macrophages in the Remodeling Failing Heart. *Circ. Res.* **2016**, *119*, 776–778, doi:10.1161/CIRCRESAHA.116.309624.
36. Lang, C.I.; Wolfien, M.; Langenbach, A.; Muller, P.; Wolkenhauer, O.; Yavari, A.; Ince, H.; Steinhoff, G.; Krause, B.J.; David, R.; et al. Cardiac Cell Therapies for the Treatment of Acute Myocardial Infarction: A Meta-Analysis from Mouse Studies. *Cell. Physiol. Biochem.* **2017**, *42*, 254–268, doi:10.1159/000477324.
37. Oishi, Y.; Manabe, I. Macrophages in inflammation, repair and regeneration. *Int. Immunol.* **2018**, *30*, 511–528, doi:10.1093/intimm/dxy054.

38. Jenkins, W.S.; Vesey, A.T.; Stirrat, C.; Connell, M.; Lucatelli, C.; Neale, A.; Moles, C.; Vickers, A.; Fletcher, A.; Pawade, T.; et al. Cardiac $\alpha_v\beta_3$ integrin expression following acute myocardial infarction in humans. *Heart* **2017**, *103*, 607–615, doi:10.1136/heartjnl-2016-310115.
39. Vandervelde, S.; van Amerongen, M.J.; Tio, R.A.; Petersen, A.H.; van Luyn, M.J.; Harmsen, M.C. Increased inflammatory response and neovascularization in reperfused vs. non-reperfused murine myocardial infarction. *Cardiovasc. Pathol.* **2006**, *15*, 83–90, doi:10.1016/j.carpath.2005.10.006.
40. Minatoguchi, S.; Takemura, G.; Chen, X.H.; Wang, N.; Uno, Y.; Koda, M.; Arai, M.; Misao, Y.; Lu, C.; Suzuki, K.; et al. Acceleration of the healing process and myocardial regeneration may be important as a mechanism of improvement of cardiac function and remodeling by postinfarction granulocyte colony-stimulating factor treatment. *Circulation* **2004**, *109*, 2572–2580, doi:10.1161/01.CIR.0000129770.93985.3E.

www.nature.com/scientificreports

scientific reports

OPEN

Expedient assessment of post-infarct remodeling by native cardiac magnetic resonance imaging in mice

Cajetan Immanuel Lang[1]✉, Praveen Vasudevan[2,3], Piet Döring[2,5], Ralf Gäbel[2,3], Heiko Lemcke[2,3], Tobias Lindner[4], Gustav Steinhoff[2,3], Bernd Joachim Krause[5], Brigitte Vollmar[6], Felix G. Meinel[7], Seyrani Yücel[1], Alper Öner[1], Hüseyin Ince[1] & Robert David[2,3]

Novel therapeutic strategies aiming at improving the healing process after an acute myocardial infarction are currently under intense investigation. The mouse model plays a central role for deciphering the underlying mechanisms on a molecular and cellular level. Therefore, we intended to assess in-vivo post-infarct remodeling as comprehensively as possible using an expedient native magnetic resonance imaging (MRI) in the two most prominent infarct models, permanent ligation (PL) of the left anterior descending artery (LAD) versus ischemia reperfusion (I/R). Mice were subjected to either permanent or transient (45 min) occlusion of the LAD. After 3 weeks, examinations were performed with a 7-Tesla small animal MRI system. Data analysis was performed with the freely available software Segment. PL resulted in a massive dilation of the left ventricle, accompanied by hypertrophy of the non-infarcted myocardium and a decline of contractile function. These effects were less pronounced following I/R compared to healthy animals. Single plane assessments were not sufficient to capture the specific differences of left ventricular (LV) properties between the two infarct models. Bulls-eye plots were found to be an ideal tool for qualitative LV wall assessment, whereas a multi-slice sector-based analysis of wall regions is ideal to determine differences in hypertrophy, lateral wall thinning and wall thickening on a quantitative level. We combine the use of polar map-based analysis of LV wall properties with volumetric measurements using simple CINE CMR imaging. Our strategy represents a versatile and easily available tool for serial assessment of the LV during the remodeling process. Our study contributes to a better understanding of the effects of novel therapies targeting the healing of damaged myocardium.

Abbreviations

LAD	Left anterior descending artery
MRI	Magnetic resonance imaging
PL	Permanent ligation
I/R	Ischemia reperfusion
LV	Left ventricle
STEMI	ST-segment elevation myocardial infarction
MI	Myocardial infarction
CMR	Cardiac magnetic resonance imaging
EDV	End-diastolic volume
ESV	End-systolic volume

[1]Department of Cardiology, Rostock University Medical Center, Rostock, Germany. [2]Department of Cardiac Surgery, Rostock University Medical Center, Rostock, Germany. [3]Department of Life, Light and Matter, University of Rostock, Rostock, Germany. [4]Core Facility Multimodal Small Animal Imaging, Rostock University Medical Center, Rostock, Germany. [5]Department of Nuclear Medicine, Rostock University Medical Center, Rostock, Germany. [6]Rudolf-Zenker-Institute for Experimental Surgery, Rostock University Medical Center, Rostock, Germany. [7]Institute of Diagnostic and Interventional Radiology, Rostock University Medical Center, Rostock, Germany. ✉email: cajetan.lang@med.uni-rostock.de

LVEF	Left ventricular ejection fraction
SV	Stroke volume
LVM	Left ventricular mass
IVSd	Interventricular septal thickness
LVEDD	Left ventricular end diastolic dimension
LW	Lateral wall thickness
SD	Standard deviation
ED	End diastolic
ES	End systolic

Ischemic heart disease is still the main cause of death worldwide according to the World Health Organization and accounted for more than nine million deaths in 2016[1]. Primary prevention, diagnosis and treatment options of ischemic heart disease have rapidly progressed over the last decades. Particularly timely reperfusion—by both thrombolytic and interventional approaches—reduces myocardial damage dramatically and hence forms the cornerstone of modern therapies for acute ST-segment elevation myocardial infarction (STEMI) patients[2]. Yet, replacement of necrotic myocardium by scar tissue inevitably results in left ventricular remodeling and can eventually lead to heart failure. Left ventricular (LV) remodeling refers to alterations in ventricular architecture and function in response to a variety of forms of myocardial injury and increased wall stress[3,4]. In the context of myocardial infarction, ventricular remodeling is associated with characteristic changes in the early and late post myocardial infarction (MI) phases, respectively. Early LV remodeling results from replacement of necrotic myocardium by fibrotic scar tissue and leads to elongation and thinning of the infarcted zone[5]. Beyond this early phase, LV remodeling is dominated by mechanisms compensating for the loss of vital myocardium. Myocytes in the non-infarcted zone undergo hypertrophic elongation, leading to an increased wall mass, chamber enlargement and a shift from an elliptical to a more spherical chamber configuration[5]. Morphological changes, reduced performance of hypertrophied myocytes and interstitial fibrosis within the non-infarcted zone lead to progressive impairment of LV function.

Initial pivotal studies on LV remodeling were based on post-mortem techniques, such as histopathological tissue analyses[6]. The development of dedicated small animal cardiac magnetic resonance imaging (CMR) initiated a new era, providing a tool which enables high-resolution in-vivo assessment of cardiac function and post-MI remodeling in rodents with utmost precision[7–9]. CMR has become the gold standard for assessing LV remodeling in patients[10,11] for both clinical studies and optimizing therapy management. Particularly with regards to the development of novel regenerative therapies in translational research, non-invasive assessment of LV remodeling has become an indispensable tool. Preserving cardiac function and anatomical integrity is the ultimate goal of regenerative therapies for ischemic myocardium. Thereby, the mouse is the most important model organism when it comes to testing hypothesized mechanisms of action on a molecular and cellular level[12]. Despite the availability of highly elaborate protocols for CMR based assessment of left ventricular remodeling, such as MR spectroscopy and T1/T2 mapping[13], CMR-based assessment of left ventricular remodeling in studies aiming at modulating myocardial healing are mostly restricted to volumetric measurements. Yet, novel therapies targeting modulation of the post-MI healing processes and long-term LV remodeling require more comprehensive imaging approaches for gauging LV remodeling. We suppose, that a wider application of T1/T2 mapping and MR spectroscopy is hampered by the difficulty of both acquisition and image analyses and the need for expensive software add-ins. Therefore, we intended to develop a straightforward protocol which is based on native CINE CMR only, but still provides additional information about the specific properties of the remodeled LV wall. Polar maps were applied to describe both morphological and functional wall properties on a qualitative and quantitative level by using the freely available software *Segment*. Thereby, characteristics of the two most commonly used experimental models of myocardial infarction—permanent ligation (PL) of the left anterior descending (LAD) and transient occlusion of the LAD (I/R)—are visualized and assessed. As expected, myocardial damage is significantly more severe in PL compared to I/R resulting in distinct patterns of left ventricular remodeling respectively.

Methods

Animal model. 129S6/SvEvTac mice were bred in the animal facility of the Rostock University Medical Center according to the German legislation on protection of animals and the Guide for the Care and Use of Laboratory Animals[14]. All experiments performed in this study were approved by the "Landesamt für Landwirtschaft, Lebensmittelsicherheit und Fischerei Mecklenburg-Vorpommern; Rostock, Germany" (registration no. LALLF M-V/TSD/7221.3-1.1-054/15) and carried out in compliance with the ARRIVE guidelines. Myocardial infarctions were induced by either permanent occlusion (PL) or transient occlusion the LAD for 45 min (I/R) as described previously (n = 6 per group)[15,16]. Each animal received an intramyocardial injection of 10 µL PBS mixed with 10 µL Growth Factor Reduced MatrigelTM Matrix. Healthy animals served as a control group (n = 7).

Cardiac magnetic resonance imaging and analysis. For MRI imaging the mice were anaesthetised with 1.5–2.5% isoflurane in oxygen. Examinations were performed with a 7-T small animal MRI system (BioSpec 70/30, maximum gradient strength 440 mT/m, Bruker BioSpin GmbH, Ettlingen, Germany) using a water-cooled actively shielded gradient system. The MRI system was equipped with a 1H transmit volume coil (86 mm, volume resonator) and a two-by-two receive-only surface coil array (both Bruker BioSpin GmbH). Images of the left ventricle for functional and morphological measurements were acquired using a IntraGate gradient-echo cine sequences (Intragate Cine-FLASH) in five contiguous short-axis planes covering the whole left ventricle following the planning sequences for the short axis view. The following acquisition parameters were used: echo

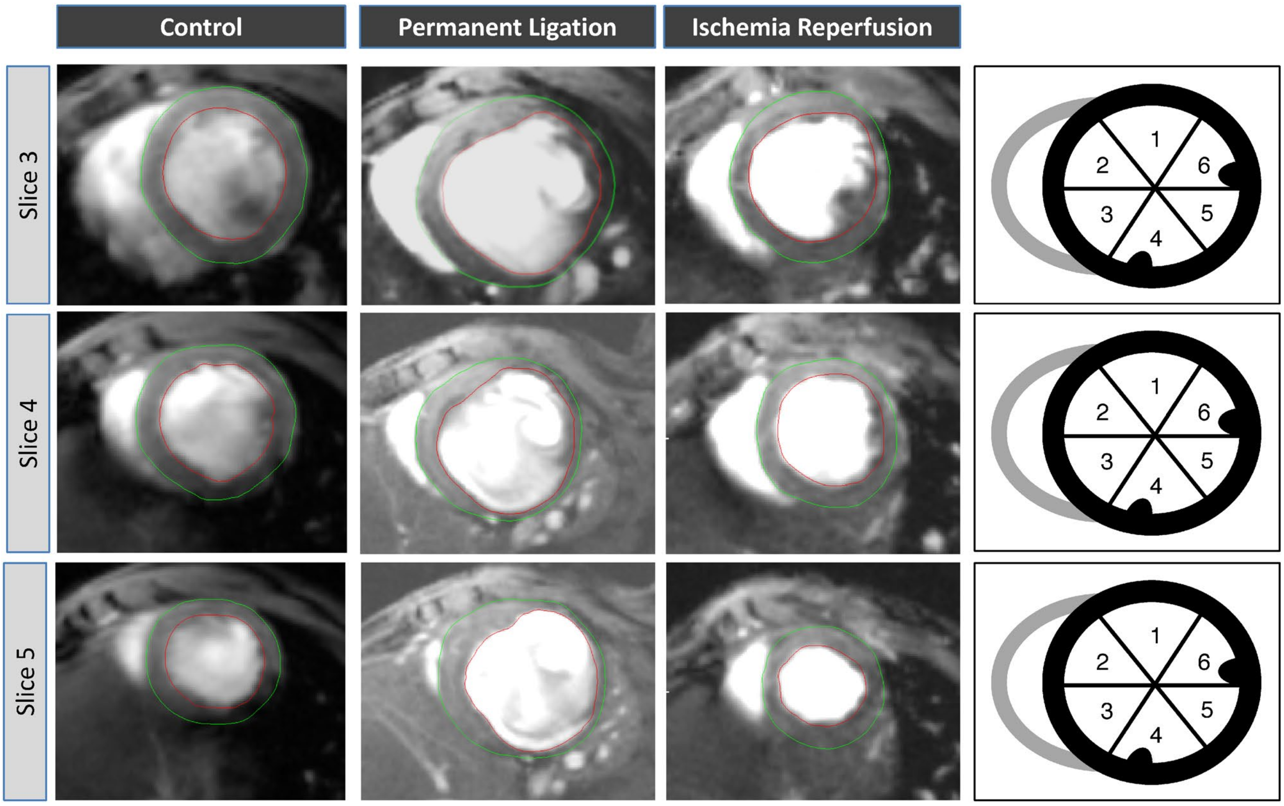

Figure 1. Multi plane assessment of the left ventricular wall. The left ventricle is covered by 5 short-axis slices from basal (1) to apical (5). The scar typically extended from slice 3–5. For regional wall analyses, slices 3–5 were divided into six segments. Septal wall: segment 2, 3. Lateral wall: segment 5, 6.

time (TE): 2.38 ms, repetition time (TR): 5.89 ms, flip angle: 15°, 14 frames per cardiac cycle, oversampling: 140, averages: 1, field of view (FOV): 29.4 × 25.2 mm, matrix size: 211 × 180, resolution in-plane: 0.14 × 0.14 mm, slice thickness: 1 mm, scan time per slice: 2 min. Body temperature of the animals was maintained by a water filled heating mat during the whole scan. Temperature of the water-filled heating mat was monitored and controlled by water bath with immersion circulator (HAAKE SC 100 and HAAKE S5P, Thermo Fisher Scientific, Schwerte Germany). Body temperature was continuously monitored by a small rectal temperature probe and maintained between 36 and 37 °C throughout the examination as previously described[17,18]. Respiration cycles and Cardiac BPM were extracted from the Intragate navigator analysis. Mean heart rates during scanning were 340.8 ± 25.4 bpm in the control group, 327.6 ± 19.6 bpm in the I/R group and 343.1 ± 30.3 in the PL group with no significant difference between the groups ($p = 0.53$).

The freely available software Segment v2.0 R5165 (http://segment.heiberg.sehttp://segment.heiberg.se)[19] was used for the assessment of cardiac function and morphology. Segmentation of the left ventricle was performed manually. Papillary muscles were excluded when defining endo- and epicardial borders. Definition of end-diastole and end-systole were calculated by the software. Following manual LV segmentation, the software calculated end-diastolic volume (EDV), end-systolic volume (ESV), left ventricular ejection fraction (LVEF), stroke volume (SV) and left ventricular mass (LVM) automatically. Interventricular septal thickness (IVSd), left ventricular end diastolic dimension (LVEDD) and lateral wall thickness (LW) were obtained from the respective end-diastolic mid-ventricular slice. Regional wall analyses were performed on a slice-by-slice basis, according to the user manual. In brief, the left ventricle was covered by 5 short-axis slices from basal (1) to apical (5). Each slice was divided into 6 sectors as visualized in Fig. 1. Qualitative analysis by bulls-eye plots showed that scar typically extended from slice 3–5. Hence, these three slices were included into quantitative regional wall analysis. Multiplane quantitative analyses of the respective septal and lateral sectors were performed as visualized in Fig. 1.

Statistics. Normality of data was assessed by the Shapiro–Wilk test. When the normality assumption was met, parametric data of control, PL and I/R group were compared by using one-way analysis of variance (ANOVA). Post-hoc pairwise comparisons were made by the Student–Newmans–Keuls method. When, the normality assumption had been violated, ANOVA on ranks was applied, followed by the Dunn´s Methods for multiple pairwise comparisons. Values of $p < 0.05$ were considered statistically significant. Statistical procedures were performed using *SigmaPlot 11.0*.

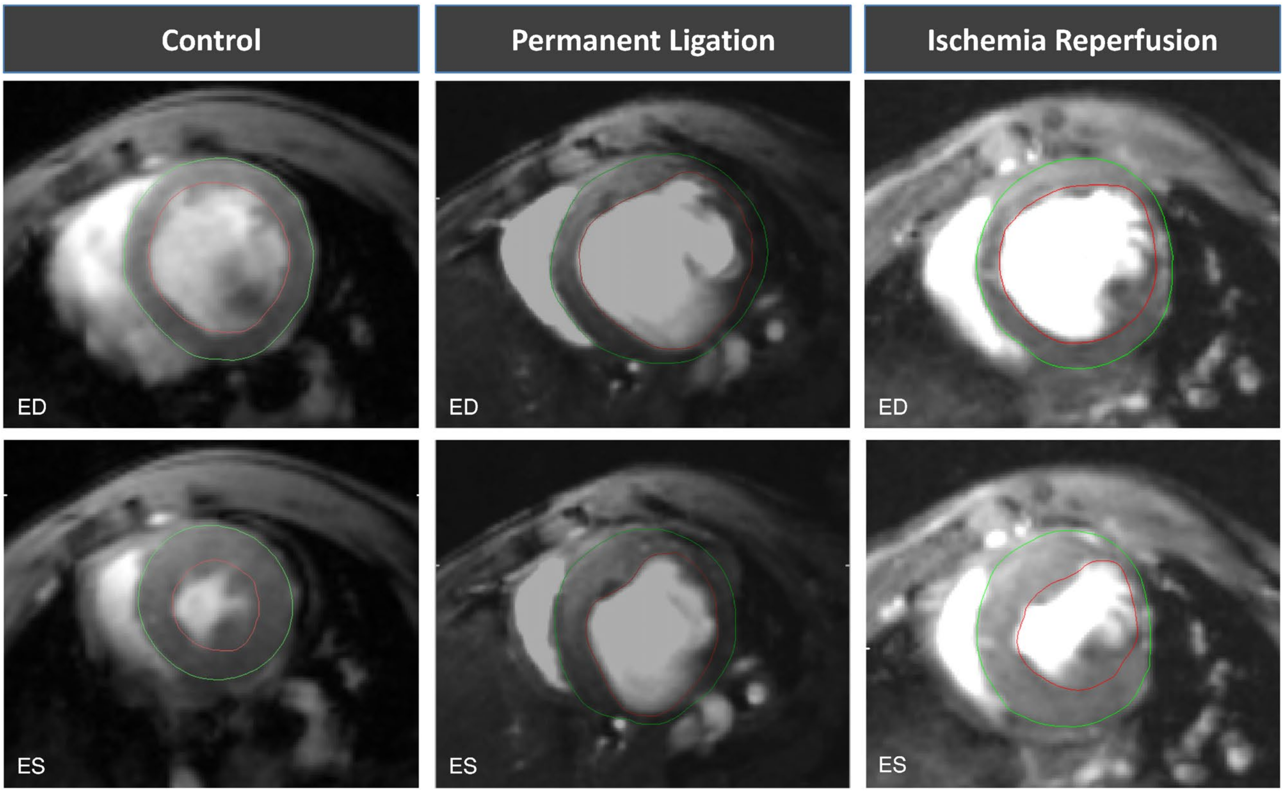

Figure 2. Representative mid-ventricular slices of healthy (control) and infarct animals 3 weeks following MI induction. Upper row: end-diastolic (ED) slices. Lower row: end-systolic (ES) slices. The epicardium is marked with a green line, the endocardium with a red line. Papillary muscles were excluded.

Ethics approval and consent to participate. All experiments performed in this study were approved by the "Landesamt für Landwirtschaft, Lebensmittelsicherheit und Fischerei Mecklenburg-Vorpommern; Rostock, Germany" (registration no. LALLF M-V/TSD/7221.3-1.1-054/15).

Consent for publication. Not applicable.

Results

Volumetric and functional changes. In healthy animals, end-diastolic volume (EDV) was 52.6 ± 4.0 µL whereas the end-systolic volume (ESV) measured 25.7 ± 2.3 µL. Left ventricular ejection fraction (LVEF) was 50.9 ± 1.8% and the stroke volume (SV) 26.9 ± 2.3 µL. Values from healthy animals served as control.

Permanent ligation of the LAD resulted in a massive dilation of the left ventricle with significantly increased diastolic and systolic volumes (EDV: 93.7 ± 14.7 µL, $p < 0.001$ vs. control; ESV: 67.5 ± 12.1 µL, $p < 0.001$ vs. control). These changes in chamber geometry resulted in a dramatic decline of the ejection fraction (LVEF: 28.3 ± 2.6%, $p < 0.05$ vs. control). Yet, the stroke volume remained preserved (SV: 26 ± 4.0 µL, $p = 0.86$) (Figs. 2 and 3).

Transient occlusion (I/R) of the LAD lead to similar, but less severe changes of left ventricular geometry three weeks after MI induction compared to the healthy control group (EDV: 65.3 ± 8.3, $p < 0.001$; ESV: 38.2 ± 10.9 µL, $p < 0.05$) (Figs. 2 and 3). This resulted in a less dramatic reduction of the LVEF (42.3 ± 9.2 µL, $p > 0.05$ vs. control). Similar to the observation in the PL group, the stroke volume remained preserved (SV: 27.0 ± 4.0, $p = 0.86$) (Figs. 2 and 3).

PL resulted in significantly greater volumes of the left ventricle compared to I/R, with a more dramatic decline of the LVEF (Fig. 3).

Scar thinning and LV hypertrophy. Ventricular remodeling in the early phase post MI is a consequence of the replacement of necrotic myocardium by fibrotic scar tissue, which is subsequently subjected to elongation and thinning. Short-axis parameters of the respective end-diastolic mid-ventricular slice were used with the goal to visualize and quantify this process.

Permanent ligation lead to a significant increase of the left ventricular end diastolic dimension compared to the control group (LVEDD: 5.7 ± 0.7 mm vs. 4.1 ± 0.4, $p < 0.001$). The lateral wall thickness (LW) is significantly reduced (LW: 0.43 ± 0.05 mm vs. 0.65 ± 0.08 mm, $p < 0.05$). Yet, LV hypertrophy of the non-infarcted myocardium can only be hypothesized from this single slice assessment of the interventricular septum (IVSd: 0.77 ± 0.14 vs. 0.68 ± 0.08, $p = 0.29$) (Figs. 4 and 5).

Visual and qualitative inspection of the scar area (Fig. 4) reveals a smaller circumferential extent of the scar in the I/R compared the PL group. Whereas LV dilation could be clearly assessed by the determination of EDV

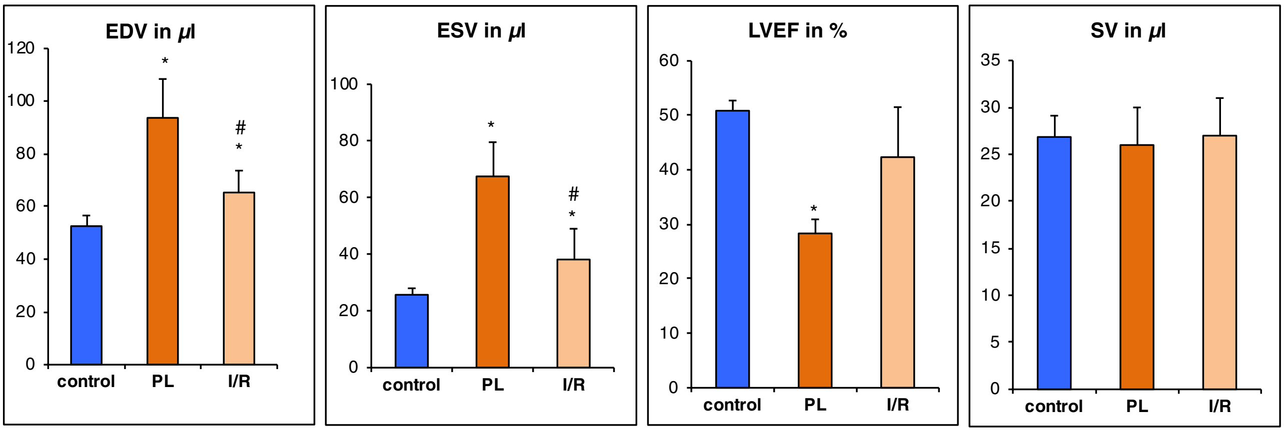

Figure 3. Volumetric and functional changes 3 weeks after MI induction. Values are mean ± SD. $^{*}p < 0.05$ compared to control group. $^{\#}p < 0.05$ compared to PL.

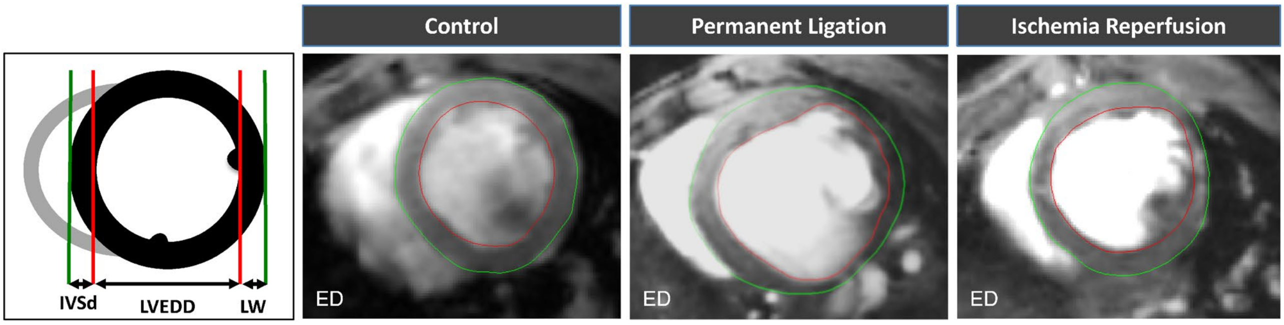

Figure 4. Short-axis End-diastolic mid-ventricular slices—measurement of diastolic interventricular septal thickness (IVSd), LV end diastolic dimension (LVEDD) and lateral wall (LW).

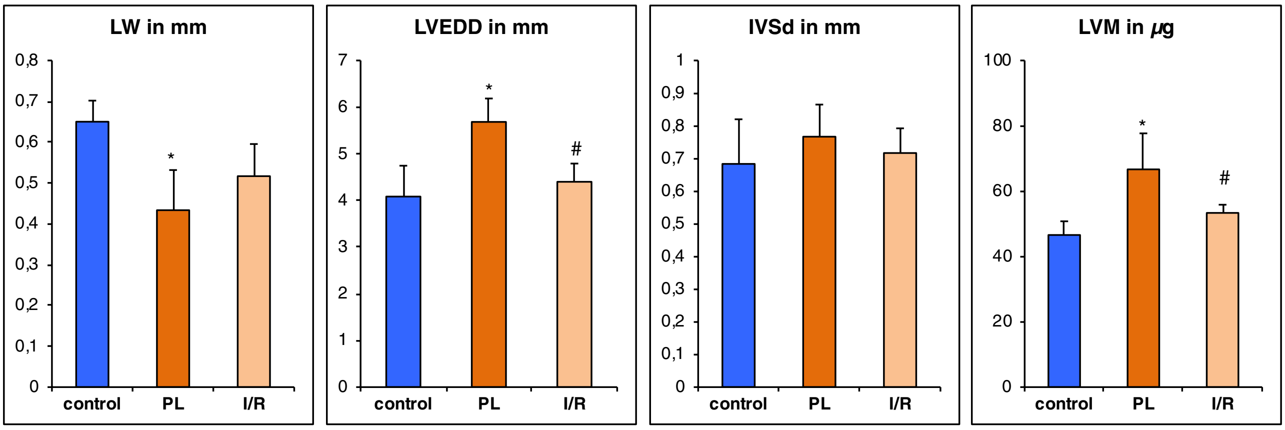

Figure 5. Short-axis end-diastolic dimensions and left ventricular mass. Values are mean ± SD. $^{*}p < 0.05$ compared to control group. $^{\#}p < 0.05$ compared to PL.

and ESV (Fig. 3), single slice assessment of the end-diastolic LV dimension was not significantly increased compared to the control group (LVEDD: 4.4 ± 0.52 mm vs. 4.1 ± 0.40 mm, $p = 0.26$) (Fig. 5). Likewise, scar thinning resulted in a thinner lateral wall—yet not reaching a level of significance—compared to the control group (LW: 0.51 ± 0.10 mm vs. 0.65 ± 0.08 mm, $p > 0.05$). Similar to the PL group, the thickness of the interventricular septum was not significantly increased (IVSd: 0.72 ± 0.01 vs. 0.68 ± 0.08, $p = 0.29$).

Whereas single slice assessment of the IVSd did not sufficiently depict LV hypertrophy, left ventricular mass (LVM) as calculated from all slices covering the left ventricle was significantly increased in the PL group. Yet, the increase of LVM in the I/R group did not reach a level of significance (Fig. 5).

Regional LV wall analyses. For a more comprehensive measurement and visualization of LV hypertrophy of the non-infarcted zone and the wall thinning within the scar area, we performed regional wall analysis of the whole LV (Figs. 1 and 6). Thereby, polar plots showed aneurysm formation within the scar area and a thickened wall in the septal region (Fig. 6). The scar typically extended from the apical to the mid-ventricular slice, corresponding to slice 3–5 (Fig. 6). Each slice was divided into 6 segments as visualized in Fig. 1. The septal wall is represented by the respective segments 2 and 3, the lateral wall by the respective segments 5 and 6.

Quantitative assessments of regional wall thickness show that hypertrophy of the non-infarcted myocardium is present in both infarct models. Compared to the control group, end-diastolic septal wall thickness is significantly increased both in the PL group (0.91 ± 0.10 mm vs. 0.68 ± 0.06 mm, $p < 0.0001$) and the I/R group (0.77 ± 0.04 mm vs. 0.68 ± 0.06 mm, $p < 0.005$) (Fig. 7).

Thinning of the infarct zone was assessed by measuring the end-diastolic lateral wall thickness (segments 5, 6). Permanent ligation of the LAD resulted in a significant thinning of the lateral wall compared to the control group (0.43 ± 0.09 mm vs. 0.60 ± 0.05, $p < 0.001$). Transient occlusion potentially resulted in a slight, yet not significant reduction of the lateral wall thickness (0.57 ± 0.09 vs. 0.60 ± 0.05 mm, $p = 0.32$).

Assessment of the regional wall thickness was used as surrogate measures of LV hypertrophy and scar thinning. Both parameters are determined from end-diastolic images and represent morphological measures. Yet, we assumed quality and composition of the scar area would affect radial wall motion properties. Therefore, wall thickening—the difference between end-diastolic and end-systolic wall thicknesses—was determined for both infarct models compared to the control group. Permanent ligation of the LAD led to a significantly reduced wall thickening in the infarct region (− 0.03 ± 0.06 mm vs. 0.21 ± 0.06 mm, $p < 0.001$) but preserved wall thickening in the septal region (0.25 ± 0.13 mm vs. 0.27 ± 0.07 mm, $p = 0.31$). Similarly, transient occlusion of the LAD resulted in significantly reduced wall thickening in the infarct region (0.07 ± 0.11 mm vs. 0.21 ± 0.06 mm, $p < 0.005$) with preserved septal wall thickening (0.31 ± 0.06 mm vs. 27 ± 0.07 mm, $p = 0.31$) (Figs. 7 and 8).

Discussion

The size of a myocardial infarction has been correlated with the extent of LV remodeling in the late 70s[20] in a rat model and eventually been confirmed in patients in the 90s[21]. LV remodeling is a progressive process, which is closely linked to activation of the renin–angiotensin–aldosterone axis (RAAS) and the adrenergic nervous system. Pharmacological inhibition of these mechanisms has the potential to stop or even reverse pathological remodeling[5]. The imaging-based parameters EDV, ESV and LVEF proved to be reliable surrogate parameters to both estimate cardiovascular events and the effects of pharmacological RAAS inhibition[5]. Hence, monitoring infarct size and left ventricular chamber dimensions are well-established surrogate markers for the effect of therapies for the treatment of myocardial infarctions in patients.

Novel therapies aiming at reducing myocardial damage or restoring contractile function usually target very specific biological mechanisms. Therefore, pilot proof-of-concept studies are most commonly conducted in animal models. Mere global volumetric and functional parameters will not suffice to capture these effects. From a translational perspective, development of novel therapies targeted at modulating myocardial healing requires methods for sequential and comprehensive in-vivo assessment of the remodeling process.

Interestingly, a variety of highly elaborate protocols for CMR based assessment of left ventricular remodeling[13] have been developed. Yet, studies aiming at modulating myocardial healing are mostly restricted to volumetric measurements. The application of elaborate CMR techniques, e.g. MR spectroscopy, requires elaborate and expensive software and profound expertise in CMR radiology, which might hamper a wider application of these attractive tools. This motivated us to develop a protocol, which is based on CINE CMR only, but still provides additional and highly valuable information about the specific properties of the remodeled LV wall.

Therefore, mice were subjected to permanent occlusion (PL) or transient occlusion (I/R) of the LAD, respectively. Post-infarct ventricular remodeling was assessed after 3 weeks by native CMR. PL resulted in a massive dilation of the left ventricle and thinning of the scar, with consecutive formation of an anterolateral aneurysm. Interestingly, despite dramatic increases in EDV and ESV and an according decrease of the LVEF, stroke volume (SV) remained unaffected (Fig. 3). Compared to the PL group, myocardial damage induced by I/R was less pronounced, accordingly LV remodeling was significantly less dramatic. Similar to the PL group, stroke volume was preserved.

Our overall observation, that LV dilation and consecutive impairment of cardiac function parameters caused by PL is more pronounced compared to I/R, is well in line with findings by other groups[17,22–24]. The observation that SV remains preserved despite LV dilation in both infarct models has also been made by Soepriatna et al. in mice[17]. Similar findings in patients, namely the fact that SV is commonly not reduced despite enormous LV dilation in patients, has been extensively reviewed by Maciver et al.[25] and can most probably be explained by a compensated stage of heart failure in both animals and patients at the time of assessment.

Post-infarct LV remodeling comprises characteristic alterations in both infarcted and non-infarcted myocardium. Fibrotic repair of the necrotic area results in scar formation with consecutive elongation and thinning of the infarcted zone[5]. On the other hand, adaptive mechanisms, such as hypertrophic myocyte elongation in the non-infarcted myocardium and a consecutive increase of LV mass have the capacity to compensate for the loss of functional cardiomyocytes to a certain extent[5]. These adaptive mechanisms retain normal cardiac output in the initial post-MI phase but eventually result in progressive fibrosis of the pathologically hypertrophied non-infarcted myocardium, chamber enlargement and a decline in ventricular performance[5].

PL of the LAD induces a large transmural scar with a thin remaining rim of endocardial-located viable cardiomyocytes resulting in progressive thinning of the fibrous scar[26,27]. In contrast, I/R induces a longitudinal scar layer in the middle of the LV myocardium with non-infarcted endocardial and epicardial myocardium left[27].

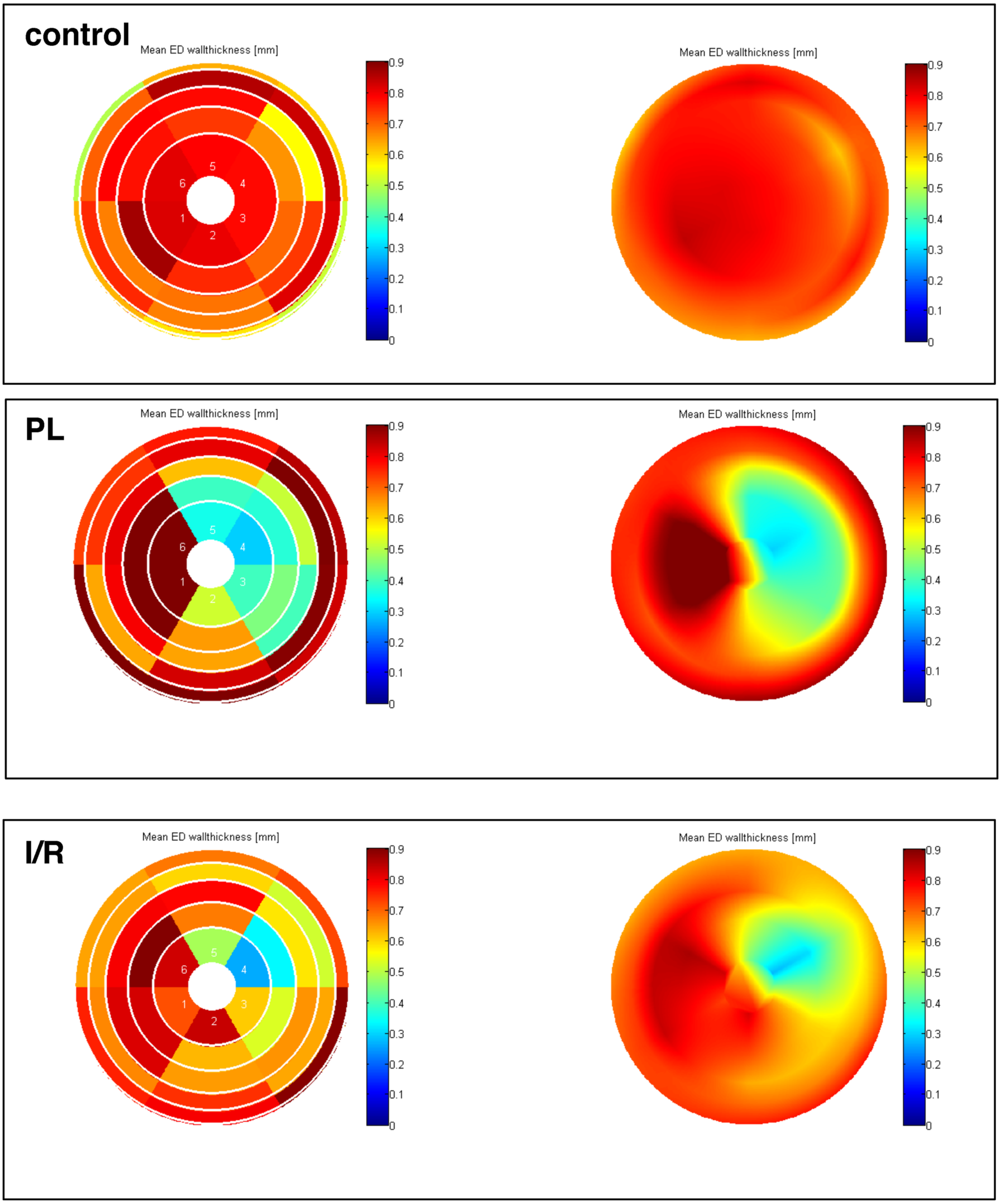

Figure 6. Polar plots of the left ventricle for visual and qualitative assessment of LV wall thickness. Each ring represents one short-axis slice. The apical slice 5 is located in the middle. The basal slice 1 is the outer ring. The "smooth bulls eye view" (right side) visualizes the aneurysm formed in the lateral wall.

As a consequence, LV wall thickness in the infarct region is maintained. Yet, both infarct models show signs of compensatory hypertrophy of the non-infarcted region measured by histological methods[24].

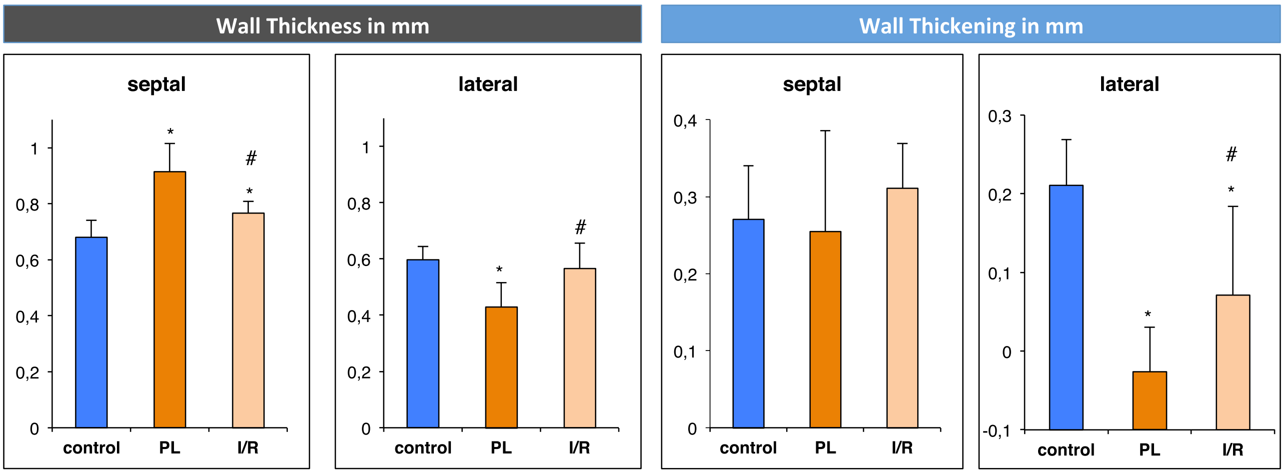

Figure 7. Regional wall analysis of short-axis slices 3–5. Wall thickness was assessed in end-diastolic images. Wall thickening is the difference between end-systolic and end-diastolic wall thickness. Values are mean ± SD. $^{*}p < 0.05$ compared to control group. $^{\#}p < 0.05$ compared to PL group.

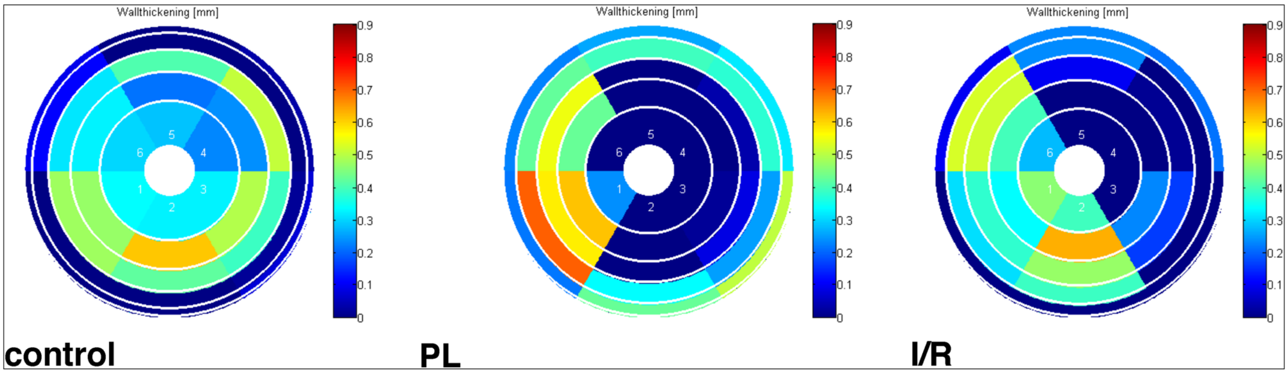

Figure 8. Left ventricular wall thickening. Representative polar maps of visualizing LV wall thickening of healthy (control) and MI animals.

Differences in regional left ventricular wall properties between PL and I/R in mice had been described mostly in post mortem studies until recently[26–29]. The evolution of elaborate techniques for qualitative tissue assessment resulted in studies describing differences in LV wall properties between the two infarct models by both echocardiographic-based regional myocardial strain analysis[17] and CMR-based T1/T2 mapping[23].

Here, we developed a simple and straightforward protocol, based on CINE CMR only, to provide a tool for regional LV wall analysis for scientists in the field of experimental cardiology who are not designated experts in the field of cardiovascular imaging.

In our study, we measured changes of LV wall dimensions by both single plane and multiple plane approaches. Thereby, using a clinically well-established single plane view, the mid-ventricular parasternal short axis, only thinning of the infarct wall reached the level of significance. Hence, we used a multi-slice approach for more comprehensive analysis of the LV wall properties in both infarct models (Fig. 1). We used left ventricular mass (LVM) as a surrogate for overall hypertrophy of the non-infarcted myocardium. LVM was significantly increased by PL and to a less but significant extent by I/R (Fig. 3). Bulls-eye plots were used for qualitative assessment of the specific remodeling patterns of PL and I/R respectively. We used a multi-plane approach to capture differences of septal and lateral wall properties as visualized in Fig. 1.

We found PL to induce dramatic thinning of the lateral wall accompanied by hypertrophy of septal wall regions, a finding, which is in line with previous reports[24,26]. In contrast to single plane approaches[26], we found I/R to result in LV hypertrophy and a consecutive increase in septal wall thickness in our study. Yet, as supposed, lateral wall thickness was preserved after I/R.

For functional assessment of the scarred myocardium, we measured regional wall thickening in both infarcted and non-infarcted regions. As one would expect, the dilated scar in PL mice exhibited a negative thickening value, which might represent the passive systolic expansion of the aneurysmal lateral wall. Interestingly, despite retained thickness of the lateral wall after I/R, wall thickening was dramatically reduced. This finding suggests, that scarring after I/R has significant implications on LV function, despite a lack of changes on lateral wall dimensions. Similarly, Soepriatna et al. who used echocardiography based three-dimensional strain mapping, found significantly higher strain values within the infarcted myocardium of I/R compared PL mice[17]. Haberkorn et al.

also described distinct differences in T1 values within the infarct region between IR and PL in mice, which they ascribe to fibrotic changes[23].

Conclusions

By the use of multi-plane sector analysis, we succeeded in capturing both morphological and functional differences between PL and I/R regarding post-infarction LV remodeling by native CMR. We believe our approach to offer a deeper understanding of the specific functional implications of both PL and I/R. This will provide an excellent and simple tool for unraveling the effects of novel therapies targeting at healing damaged myocardium.

Limitations. We did not apply late gadolinium enhancement CMR, which represents the gold standard for determination of circumferential scar size extent. The scarred area can only be estimated indirectly based on the "thinning" of the infarct region. Furthermore, our approach is based on the repeated assessment of five contiguous 1 mm thick short-axis slices. Hence, the longitudinal increase in LV mass and wall motion properties may have been missed. Also, the heart rates below 400 per minute, as a potential result of anesthesia, may have affected the assessed functional parameters[30]. Lack of intra- and inter-observer analysis may also have produced some inaccuracy. Finally, the injection of Matrigel matrix into the infarct region of all mice may have contributed to our failure to detect significant wall-thinning in the infarct regions of the I/R mice.

Data availability

The datasets used and analyzed during the current study are available from the corresponding author on reasonable request.

Received: 10 January 2021; Accepted: 18 May 2021

References

1. Nowbar, A. N., Gitto, M., Howard, J. P., Francis, D. P. & Al-Lamee, R. Mortality from ischemic heart disease. *Circ. Cardiovasc. Qual. Outcomes* **12**(6), e005375 (2019).
2. Frohlich, G. M., Meier, P., White, S. K., Yellon, D. M. & Hausenloy, D. J. Myocardial reperfusion injury: looking beyond primary PCI. *Eur. Heart J.* **34**(23), 1714–1722 (2013).
3. McKay, R. G. *et al.* Left ventricular remodeling after myocardial infarction: a corollary to infarct expansion. *Circulation* **74**(4), 693–702 (1986).
4. Patten, R. D. & Konstam, M. A. Ventricular remodeling and the renin angiotensin aldosterone system. *Congest. Heart Fail* **6**(4), 187–192 (2000).
5. Konstam, M. A., Kramer, D. G., Patel, A. R., Maron, M. S. & Udelson, J. E. Left ventricular remodeling in heart failure: current concepts in clinical significance and assessment. *JACC Cardiovasc. Imaging* **4**(1), 98–108 (2011).
6. Pfeffer, M. A. & Braunwald, E. Ventricular remodeling after myocardial infarction. Experimental observations and clinical implications. *Circulation* **81**(4), 1161–1172 (1990).
7. Wiesmann, F. *et al.* Cardiovascular phenotype characterization in mice by high resolution magnetic resonance imaging. *MAGMA* **11**(1–2), 10–15 (2000).
8. Vallee, J. P., Ivancevic, M. K., Nguyen, D., Morel, D. R. & Jaconi, M. Current status of cardiac MRI in small animals. *MAGMA* **17**(3–6), 149–156 (2004).
9. Epstein, F. H. MR in mouse models of cardiac disease. *NMR Biomed.* **20**(3), 238–255 (2007).
10. Salerno, M. *et al.* Recent advances in cardiovascular magnetic resonance: techniques and applications. *Circ. Cardiovasc. Imaging* **10**(6), e003951 (2017).
11. Ibanez, B. *et al.* Cardiac MRI endpoints in myocardial infarction experimental and clinical trials: JACC scientific expert panel. *J. Am. Coll. Cardiol.* **74**(2), 238–256 (2019).
12. Patten, R. D. & Hall-Porter, M. R. Small animal models of heart failure: development of novel therapies, past and present. *Circ. Heart Fail* **2**(2), 138–144 (2009).
13. Vanhoutte, L. *et al.* High field magnetic resonance imaging of rodents in cardiovascular research. *Basic Res. Cardiol.* **111**(4), 46 (2016).
14. Animal. *NRCUCftUotGftCaUoL: Guide for the Care and Use of Laboratory Animals* 8th edn. (National Academies Press (US), Washington, 2011).
15. Muller, P. *et al.* Intramyocardial fate and effect of iron nanoparticles co-injected with MACS((R)) purified stem cell products. *Biomaterials* **135**, 74–84 (2017).
16. Vasudevan, P. *et al.* 18F-FDG PET-based imaging of myocardial inflammation predicts a functional outcome following transplantation of mESC-derived cardiac induced cells in a mouse model of myocardial infarction. *Cells* **8**(12), 1613 (2019).
17. Soepriatna, A. H. *et al.* Three-dimensional myocardial strain correlates with murine left ventricular remodelling severity post-infarction. *J. R Soc. Interface* **16**(160), 20190570 (2019).
18. Russo, I. *et al.* A novel echocardiographic method closely agrees with cardiac magnetic resonance in the assessment of left ventricular function in infarcted mice. *Sci. Rep.* **9**(1), 3580 (2019).
19. Heiberg, E. *et al.* Design and validation of segment–freely available software for cardiovascular image analysis. *BMC Med. Imaging* **10**, 1 (2010).
20. Pfeffer, M. A. *et al.* Myocardial infarct size and ventricular function in rats. *Circ. Res.* **44**(4), 503–512 (1979).
21. Chareonthaitawee, P., Christian, T. F., Hirose, K., Gibbons, R. J. & Rumberger, J. A. Relation of initial infarct size to extent of left ventricular remodeling in the year after acute myocardial infarction. *J. Am. Coll. Cardiol.* **25**(3), 567–573 (1995).
22. du Pre, B. *et al.* Variation within variation: comparison of 24-h rhythm in rodent infarct size between ischemia reperfusion and permanent ligation. *Int. J. Mol. Sci.* **18**(8), 1670 (2017).
23. Haberkorn, S. M. *et al.* Cardiovascular magnetic resonance relaxometry predicts regional functional outcome after experimental myocardial infarction. *Circ. Cardiovasc. Imaging* **10**(8), e006025 (2017).
24. Pluijmert, N. J., Bart, C. I., Bax, W. H., Quax, P. H. A. & Atsma, D. E. Effects on cardiac function, remodeling and inflammation following myocardial ischemia-reperfusion injury or unreperfused myocardial infarction in hypercholesterolemic APOE*3-Leiden mice. *Sci. Rep.* **10**(1), 16601 (2020).
25. MacIver, D. H. & Dayer, M. J. An alternative approach to understanding the pathophysiological mechanisms of chronic heart failure. *Int. J. Cardiol.* **154**(2), 102–110 (2012).

26. De Celle, T. *et al.* Long-term structural and functional consequences of cardiac ischaemia-reperfusion injury in vivo in mice. *Exp. Physiol.* **89**(5), 605–615 (2004).
27. Vandervelde, S. *et al.* Increased inflammatory response and neovascularization in reperfused vs. non-reperfused murine myocardial infarction. *Cardiovasc. Pathol.* **15**(2), 83–90 (2006).
28. Hashmi, S. & Al-Salam, S. Acute myocardial infarction and myocardial ischemia-reperfusion injury: a comparison. *Int. J. Clin. Exp. Pathol.* **8**(8), 8786–8796 (2015).
29. Michael, L. H. *et al.* Myocardial infarction and remodeling in mice: effect of reperfusion. *Am. J. Physiol.* **277**(2 Pt 2), H660-668 (1999).
30. Lindsey, M. L., Kassiri, Z., Virag, J. A. I., de Castro Bras, L. E. & Scherrer-Crosbie, M. Guidelines for measuring cardiac physiology in mice. *Am. J. Physiol. Heart Circ. Physiol.* **314**(4), H733–H752 (2018).

Author contributions

Conceptualization, C.I.L. and R.D; methodology, T.L., F.G.M., formal analysis, C.I.L. and P.D.; investigation, C.I.L., P.D., P.V., R.G.; writing—original draft preparation, C.I.L.; writing—review and editing, G.S., B.J.K., B.V., H.L., F.G.M., S.Y., A.Ö., H.I., R.D.; visualization, C.I.L. and P.V.; supervision, R.D.; funding acquisition, C.I.L., R.D., B.V. and B.J.K. All authors have read and approved the final manuscript.

Funding

Open Access funding enabled and organized by Projekt DEAL. This work was supported by the German Heart Research Foundation (F/34/15) and the FORUN Program of Rostock University Medical Center (889066). P.V.; H. L. and R.D. were supported by the BMBF (VIP + 00240) and the EU Social Fund (ESF/14-BM-A55-0024/18, ESF/14-BM-A55-0027/18). In addition, R.D. was supported by the DAMP foundation and the DFG (DA1296/6-1). The small animal MRI system was funded by the European Regional Development Fund (EFRE UHROM 16). C.I.L. was supported by the Clinician Scientist Program of Rostock University Medical Center.

Competing interests

The authors declare no competing interests.

Additional information

Correspondence and requests for materials should be addressed to C.I.L.